PIPELINE INTEGRITY FOR GROUND MOVEMENT HAZARDS

FINAL REPORT
R-07-082-459

Prepared for:
United States Department of Transportation
Pipeline and Hazardous Materials Safety Administration
Office of Pipeline Safety

December 2008

Captain Robert A. Bartlett Building
Morrissey Road
St. John's, NL
Canada A1B 3X5

T: (709) 737-8354
F: (709) 737-4706

Info@c-core.ca
www.c-core.ca

This page is intentionally left blank

PIPELINE INTEGRITY FOR GROUND MOVEMENT HAZARDS

FINAL REPORT

Version 2

Prepared for:
United States Department of Transportation

Prepared by:
C-CORE

C-CORE Report:
R-07-082-459

December 2008

Innovative Engineering Solutions
Captain Robert A. Bartlett Building
Morrissey Road
St. John's, NL
Canada A1B 3X5

T: (709) 737-8354
F: (709) 737-4706

Info@c-core.ca
www.c-core.ca

The correct citation for this report is:

C-CORE (2008) Pipeline Integrity For Ground Movement Hazards. Report prepared for United States Department of Transportation, C-CORE Report R-07-082-459v2, December 2008.

Project Team
Ryan Phillips (Project Manager)
John Barrette
Ahmad Jafari
Tim Park
Gerry Piercey

REVISION HISTORY

VERSION	NAME	COMPANY	DATE OF CHANGES	COMMENTS
v1	Ryan Phillips	C-CORE	Mar 08	Draft report for team and then client review
v2	Ryan Phillips	C-CORE	Dec 08	Final report

DISTRIBUTION LIST

COMPANY	NAME	NUMBER OF COPIES
United States Department of Transportation	James Merritt	PDF
Pipeline Research Council International, Inc.	Ken Lorang	PDF
D. G. Honegger Consulting	Doug Honegger	PDF
SSD, Inc.	Jim Hart	PDF

EXECUTIVE SUMMARY

PRCI is leading a program to develop a comprehensive set of guidelines and recommended practices for evaluating pipelines in areas subjected to large-scale ground movements comprising 5 main tasks. This engineering report presents Task 2: Improved Pipeline/Soil Interaction Modeling and Task 3: Improved Pipeline Response Modeling, which are the responsibility of C-CORE. An assessment of INSAR current practice for remote sensing applications is also included.

Recommendations are made for improvements to current guidelines for pipeline/soil interaction modelling in respect of axial, lateral and combined load effects. The axial resistance results mainly from friction caused by normal effective soil stresses acting around the pipe circumference. These stresses should also include bearing stresses mobilised by pipe movement in the transverse direction, and consideration of pore water pressure effects.

Significant research has shown that combined vertical upward and lateral resistances to pipe motion are limited by this finite resistance. This oblique loading effect should be reintroduced into future guideline revisions.

The study simulations have confirmed the importance of combined axial and lateral soil resistance to pipe motion in both dry sand and saturated clay. The oblique loading conditions produced an interaction envelope under axial and lateral load comprised of 2 different failure criteria. For low load angles, the criterion is sliding along the interface between the pipe and soil. For larger angles, after a transition, the second criterion is shear failure through the soil mass. The shear failure criterion was found to be well approximated in sand and clay using a Von Mises type failure criterion.

Three worked examples showed effects of the interaction between axial and lateral soil resistance in pipe-soil (beam-spring) structural analysis for aseismic ground movement. The current practice soil spring formulation generally predicted higher pipe bending strains when interaction effects were not considered.

Higher order ‘elbow’ elements are viable alternative pipe formulation when distortion of the cross-section by ovalization and warping dominates the pipe behavior. This study has demonstrated that continuum finite element modelling is a viable alternative to structural modelling for detailed consideration of short pipe section subject to ground movement.

TABLE OF CONTENTS

EXECUTIVE SUMMARY
TABLE OF CONTENTS
NOMENCLATURE
1 INTRODUCTION 1-1
1.1 Program Overview 1-1
1.2 C-CORE Project Overview 1-2
1.2.1 Improved Pipeline/Soil Interaction Modeling 1-2
1.2.2 Improved Pipeline Response Modeling 1-3
1.2.3 Options to Mitigate Risks of Large Ground Displacement 1-4
2 LITERATURE REVIEW 2-1
2.1 Scope 2-1
2.2 Current Design Practice 2-1
2.3 Axial Response 2-3
2.4 Transverse Horizontal Interaction 2-5
2.5 Transverse Vertical Interaction 2-11
2.6 Pipe-Soil Interaction Modelling 2-12
2.7 Oblique Pipe Movement 2-14
3 MODELING OBLIQUE PIPE SOIL INTERACTION IN CLAY 3-1
3.1 Introduction 3-1
3.2 Analysis Specifications 3-1
3.3 Soil Constitutive Model 3-2
3.4 Numerical Simulations For Clay 3-6
3.4.1 Loads 3-6
3.4.2 Numerical simulation results 3-6
3.4.3 Burial depth and adhesion sensitivity 3-9
3.4.4 Load path dependency 3-12
4 MODELLING OBLIQUE PIPE SOIL INTERACTION IN SAND 4-1
4.1 Introduction 4-1
4.2 Soil Properties And Applied Loads 4-1
4.3 Numerical Simulation Results 4-2
4.4 Burial Depth And Other Sensitivities 4-7
4.4.1 Loading 4-7
4.4.2 Buried pipe in dense sand, H/D =1.5 4-7

4.4.3 Buried pipe in dense sand, H/D =2.5 4-8
4.5 Effects Of Soil Hardening On Oblique Pipe Soil Interaction 4-13
4.5.1 Soil constitutive model 4-13
4.5.2 Numerical simulations 4-14
4.6 Effects Of Elastic Stiffness On Oblique Pipe Soil Interaction 4-19
5 CENTRIFUGE MODELLING 5-1
5.1 Introduction 5-1
5.2 Summary Program 5-1
5.3 Experimental Apparatus 5-2
5.3.1 Pipe sections and load cells 5-2
5.3.2 Test Package & Actuator 5-3
5.4 Soil Preparation and Testing 5-5
5.4.1 Testbed preparation 5-5
5.4.2 Instrumentation and measurement 5-6
5.4.3 Test Procedure 5-6
5.4.4 Clay shear strength and water content 5-9
5.5 Sand Test Results 5-10
5.6 Clay Test Results 5-15
5.7 Numerical & Physical Model Comparison 5-19
5.7.1 Clay tests 5-19
5.7.2 Sand tests 5-22
6 IMPROVED PIPELINE RESPONSE MODELING 6-1
6.1 Alternative Soil Spring Formulations 6-1
6.1.1 Simple downslope pipeline movement 6-2
6.1.2 Simple lateral slide 6-5
6.1.3 Three dimensional pipeline example 6-11
6.2 Alternative Pipeline Mechanical Formulation 6-17
6.3 Continuum Pipeline/Soil Interaction Analysis 6-19
7 SUMMARY AND CONCLUSIONS 7-1
8 REFERENCES 8-1
9 APPENDIX A : ABAQUS/STANDARD IMPLEMENTATION 9-1
9.1 Hardening/Softening 9-1
9.2 Elastic Stiffness 9-2
10 APPENDIX B : ASSESSMENT OF INSAR CURRENT PRACTICE FOR REMOTE SENSING APPLICATIONS 10-1
10.1 Synthetic Aperture Radar (SAR) Interferometry 10-1

10.2 Principles of Interferometry from Space 10-1
10.3 Factors Affecting InSAR Results 10-4
10.3.1 Temporal Decorrelation 10-5
10.3.2 Baseline Decorrelation 10-6
10.3.3 Atmospheric Effects 10-7
10.4 Slope Movement Monitoring 10-8
10.4.1 SAR Look Direction 10-8
10.4.2 SAR Layover and Shadow 10-9
10.5 Geo-referencing and Control of SAR Images 10-11
10.5.1 Collection of GCPs for Geo-referencing of SAR Images 10-11
10.5.2 Sources of SAR GCPs 10-12
10.5.3 Topographic Maps 10-13
10.5.4 High Resolution Orthophotography 10-13
10.5.5 Photogrammetry 10-13
10.5.6 Summary of GCP Collection 10-14
10.6 Site & InSAR Suitability 10-14
10.7 Variations To Application Of InSAR Monitoring 10-15
10.8 References 10-19
11 APPENDIX C: LATERAL-AXIAL RESPONSE INTERACTION CONSIDERATION 11-1

LIST OF TABLES

Table 2-1 Soil spring relationships, Honneger and Nyman (2004) 2-2
Table 3-1 Soil and interface constitutive parameters 3-2
Table 4-1 Sand constitutive parameters 4-1
Table 4-2 Dense soil and interface constitutive parameters 4-14
Table 5-1 Summary of experimental tests 5-1
Table 5-2 Clay test strength and water content summary 5-9
Table 6-1 Simple lateral slide soil independent reactions 6-5
Table 6-2 Soil reactions for NG and NGL pipelines 6-11

LIST OF FIGURES

Figure 2-1 Idealization of pipe-soil interaction based on structural models. 2-1
Figure 2-2 Adhesion factor for buried pipes in cohesive soils (after Honegger and Nyman 2004). 2-3
Figure 2-3 Lateral bearing capacity factors, Hansen (1961) 2-6
Figure 2-4 Lateral pipe response in clay from Phillips et al (2004b) 2-7
Figure 2-5 Lateral pipe response in sand from Karimian (2006) 2-8
Figure 2-6 Lateral pipe bearing factors in sand from Yimsiri et al (2004) 2-9
Figure 2-7 Lateral pipe bearing factors in dry and moist sand from Turner (2004) 2-10
Figure 2-8 Experimental lateral bearing factors in dry sand, Guo & Stolle (2005) 2-11
Figure 2-9 Lateral bearing factor comparison in dry sand, Guo & Stolle (2005) ... 2-11
Figure 2-10 Coupled soil response, Coccheti et al (2007) 2-13
Figure 2-11 Upward vertical and lateral load interaction, Guo (2005) 2-15
Figure 2-12 Upward vertical and lateral load interaction in sand, Hsu (1996) 2-15
Figure 2-13 Upward vertical and lateral load interaction, Vanden Berghe et al. (2005) 2-16
Figure 2-14 Lateral and axial load interaction in dense sand, Hsu et al. (2006) 2-16
Figure 3-1 Buried pipeline subjected to oblique movement. 3-1
Figure 3-2 (a) Layout and (b) FE model of the buried pipe 3-2
Figure 3-3 Predicted force-displacement curves for shallow oblique angles 3-3
Figure 3-4 Predicted force-displacement curves for intermediate oblique angles 3-4
Figure 3-5 Predicted force-displacement curves for large oblique angles 3-5
Figure 3-6 Conventions for determining the ultimate lateral interaction force. 3-6
Figure 3-7 Dimensionless interaction diagram comparisons using a) convention #1, and (b) convention #2. 3-8
Figure 3-8 Dimensionless interaction diagrams from C-CORE (2003) 3-9
Figure 3-9 Buried pipe geometries 3-9

Figure 3-10 Interaction forces in clay for (a) - (d) H/D1.5 and (e) - (h) H/D2.5..... 3-11
Figure 3-11 Normalised interaction forces in clay for H/D =1.5 and H/D = 2.5 3-12
Figure 3-12 Pipe response with alternative loading paths in clay for H/D =2.5 3-13
Figure 3-13 Interaction diagram considering loading paths in clay for H/D =2.5 3-14
Figure 4-1 Layout of the buried pipe in sand, and FE model. 4-1
Figure 4-2 Pipe response in dense sand subjected to two-step loading..... 4-2
Figure 4-3 Predicted force ratios during loading steps 1 and 2 4-3
Figure 4-4 Pipe response in loose sand subjected to two-step loading..... 4-4
Figure 4-5 Predicted pipe response to axial movement in loose and dense sands. ... 4-5
Figure 4-6 Predicted normalized pipe resistance in dense and loose sands 4-6
Figure 4-7 Layout of the buried pipes in sand..... 4-7
Figure 4-8 Finite element models: a) H/D = 1.5 and b) H/D=2.5 4-7
Figure 4-9 Lateral and axial pipe response in case of H/D =1.5 4-9
Figure 4-10 Interaction diagrams for H/D =1.5 in cohesive sand 4-10
Figure 4-11 Lateral and axial pipe response in case of H/D =2.5 4-11
Figure-4-12 Interaction diagrams for H/D =2.5 in sand 4-12
Figure 4-13 Predicted force-displacement curves for shallow oblique angles..... 4-16
Figure 4-14 Predicted force-displacement curves for intermediate oblique angles .. 4-17
Figure 4-15 Predicted force-displacement curves for large oblique angles 4-18
Figure 4-16 Interaction diagram comparison for dense sand 4-19
Figure 4-17 Predicted force-displacement curve with elastic stiffness variation. 4-20
Figure 5-1 Pipe load cell principle, after Stroud (1971)..... 5-2
Figure 5-2 Pipe load cell dead weight calibration 5-3
Figure 5-3 Pipe loading actuator overview..... 5-4
Figure 5-4 Pipe end connection details..... 5-4
Figure 5-5 Sand grain size distribution..... 5-6
Figure 5-6 Pipe segment prior to lateral loading. 5-7
Figure 5-7 Typical data record for pipe displacement in sand 5-8
Figure 5-8 Water content profiles for clay tests 5-10
Figure 5-9 Pipe segment after lateral loading, sand test 1. 5-11
Figure 5-10 Pipe response during sand tests 5-12
Figure 5-11 Normalized pipe response from sand tests..... 5-12
Figure 5-12 Normalized pipe response with displacement vectors from sand tests.. 5-13
Figure 5-13 Axial resistance ratio for sand tests 5-13
Figure 5-14 Axial resistance ratio development with axial displacement..... 5-14
Figure 5-15 Model Test of Inclined Pipeline Loading in Clay..... 5-15
Figure 5-16 Pipeline Force Response under Inclined Loading 5-16
Figure 5-17 Normalized pipe response from clay tests 5-17

Figure 5-18 Normalized lateral pipe response with displacement vectors 5-17
Figure 5-19 Axial resistance ratio development with axial displacement 5-18
Figure 5-20 Pipe response comparison for lateral clay test conditions 5-20
Figure 5-21 Pipe response comparison for 60 degree clay test conditions..... 5-20
Figure 5-22 Pipe response comparison for 20 degree clay test conditions..... 5-21
Figure 5-23 Pipe response comparison for axial clay test conditions 5-21
Figure 5-24 Interaction diagram for oblique loading in sand, H/D ~ 2 5-22
Figure 5-25 Interaction diagram comparison for oblique loading in sand, H/D ~ 2 . 5-23
Figure 6-1 Simple downslope pipeline geometry 6-2
Figure 6-2 Lateral to axial soil reaction interaction diagram 6-3
Figure 6-3 Simple downslope pipe-soil response 6-4
Figure 6-4 Simple downslope pipeline strain response 6-5
Figure 6-5 Lateral slide soil reaction interaction curve 6-6
Figure 6-6 Simple lateral pipe-soil response with no interaction effect: 6-7
Figure 6-7 Simple lateral pipe-soil response considering the interaction effect 6-8
Figure 6-8 Skewed lateral slide pipe-soil response with no interaction effect 6-9
Figure 6-9 Skewed lateral slide pipe-soil response considering the interaction effect 6-10
Figure 6-10 Pipeline alternatives subject to lateral and vertical displacement..... 6-11
Figure 6-11 NG pipeline soil reaction interaction curve. 6-12
Figure 6-12 NGL pipeline soil reaction interaction curve 6-12
Figure 6-13 NG pipe-soil response in sand with no interaction effect 6-13
Figure 6-14 NG pipe-soil response in sand considering the interaction effect..... 6-14
Figure 6-15 NGL pipe-soil response in sand with no interaction effect..... 6-15
Figure 6-16 NGL pipe-soil response in sand considering the interaction effect 6-16
Figure 6-17 Simple downslope pipeline with beam element formulation..... 6-18
Figure 6-18 Simple downslope pipeline with elbow element formulation..... 6-18
Figure 6-19 Continuum FEA of indenter – soil – buried pipe system..... 6-20
Figure 6-20 Plastic equivalent strain of continuum pipe 6-21
Figure 6-21 Comparison of pipe deflected shape and soil movement..... 6-22
Figure 6-22 Comparison of pipe strains 6-23
Figure 9-1 Implemention of hardening law in ABAQUS/STANDARD..... 9-1
Figure 9-2 Subroutine USDFLD used for hardening/softening 9-2
Figure 9-3 Subroutine USDFLD for elastic stiffness variation 9-3
Figure 9-4 Implementation of state-dependent material properties..... 9-4
Figure 10-1 Geometry of synthetic aperture radar 10-2
Figure 10-2 InSAR measurement of ground movement..... 10-2
Figure 10-3 InSAR interferogram 10-3

Figure 10-4 Reflectors can be used to mitigate the problem of temporal decorrelation 10-6
Figure 10-5 Orbit baseline changes can produce varying phase shifts..... 10-7
Figure 10-6 Polar orbiting satellites perspective (RADARSAT International, 1995). 10-8
Figure 10-7 Example of satellite looking up-slope and down-slope 10-9
Figure 10-8 The concept of layover in SAR image acquisition 10-10
Figure 10-9 The concept of shadow in SAR image acquisition 10-11
Figure 10-10 Radar reflectors using two different mounts (upper left and right), and packaged for shipping (lower centre) 10-16
Figure 10-11 IPTA example (Colour Cycle = 4 mm /year) (GAMMA website).. 10-17
Figure 10-12 The new SAR satellites RADARSAT-2 and TerraSAR-X..... 10-18
Figure 11-1 Interaction diagram 11-1

NOMENCLATURE

C	Cover depth to pipe crown
c	Soil cohesion
c_v	Coefficient of consolidation
c_u	Undrained shear strength
D	Pipe outer diameter
E	Modulus of elasticity,
f	as μ
f_s	Axial pipe-soil interface shear stress
f_x	Function relating x to t
f_y	Function relating y to p
f_z	Function relating z to q
h	Burial depth to the base of pipe
H	Burial depth to the center of pipe
K_a	Active earth pressure coefficient
K_0	Ratio of 'at rest' lateral to vertical effective stresses
L	Pipe length
N_q	Bearing capacity factor for frictional effects
N_{qh}	Lateral bearing capacity factor for frictional effects
N_{qv}	Vertical bearing capacity factor for frictional effects
N_c	Bearing capacity factor for cohesive effects
N_{ch}	Lateral bearing capacity factor for cohesive effects
N_{cv}	Vertical bearing capacity factor for cohesive effects
N^*_{ch}	Clay interaction factor associated with soil strength
N^{max}_{ch}	Upper limit of N_{ch} associated with deep burial mechanism
N_h	Lateral bearing factor for sand (total p / γ' H D)
N_p	as N_h
N_t	Axial factor for sand (total t / γ' H D)
N_v	Vertical bearing factor for sand (total q / γ' H D)
N_{yu}	as N_{ch}
N_x	Lateral bearing factor for clay (total p / c_u D)
N_γ	Bearing capacity factor for soil weight effects
N_z	Axial factor for clay (total t / c_u D)
p	Lateral soil force per unit pipeline length
p_u	Ultimate lateral soil force per unit pipeline length
P_y	as p_u
q	Vertical soil force per unit pipeline length
q_u	Ultimate vertical soil force per unit pipeline length
S_t	Strength sensitivity of the soil
s_u	as c_u
t	Axial soil force per unit pipeline length

W'	Submerged pipe weight per unit length
x	Relative axial soil-pipe movement
y	Relative lateral soil-pipe movement
v	Pipe movement velocity

α	Oblique pipe movement angle in horizontal plane
α	Axial adhesion factor
δ	Soil-pipe interface friction angle
ε^p	Plastic strain magnitude
ϕ	Soil friction angle
ϕ_{cv}	Constant volume friction angle
γ	Soil unit weight
γ'	Effective soil unit weight
γ_d	Dry soil unit weight
μ	Interface friction coefficient, tan δ
ν	Poisson's ratio
θ	Oblique pipe movement angle in vertical plane normal to pipe length
σ'	Effective normal stress
τ	Shear stress limit at the pipe soil interface.
ψ	Soil dilation angle

1 INTRODUCTION

1.1 Program Overview

Land use policies increasingly prevent pipelines from obtaining right-of-way for pipeline corridors that avoid ground movement hazards. Where ground displacement hazards cannot be avoided, the potential risks must be managed by suitable combination of design and operational strategies.

The program objective is to develop a comprehensive set of guidelines and recommended practices, in a format that can be implemented within the industry, for evaluating pipelines in areas subjected to large-scale ground movements.

The Pipeline Research Council International, Inc. (PRCI), in concert with a research team drawn from C CORE, D. G. Honegger Consulting (DGHC), SSD, Inc. (SSD), the USGS, PRCI industry sponsors that include the Southern California Gas Company, TransCanada, El Paso, Marathon Pipelines, Williams Gas Pipeline, and Gaz de France, and the California Energy Commission are assessing and recommending current landslide risk management methods and practices for use within the pipeline industry. In addition, research activities are carried out to address known deficiencies in current techniques for assessing pipeline response to large ground displacements. These guidelines will be made available from the PRCI publications web site at no charge. PRCI intends to support regular updates to the guidance document as necessary to incorporate future technological developments.

The broad technical tasks involved in the study program include: definition of large ground displacement hazards, development of pipeline/soil interaction models, improved pipeline response modeling, utilization of pipeline geometry monitoring to assess pipeline condition and, options to mitigate risks of large ground displacement. The result of this work will be a concise set of unified guidelines that can be readily implemented within the pipeline industry and serve as a basis for demonstrating that reasonable measures have been taken to address potential risks from large ground displacements.

The technical program consists of five major project activities related to (1) geohazard definition, (2) improved methods to model pipeline-soil interaction, (3) analyzing pipeline response to geohazards, (4) methods to mitigate pipeline risk posed by geohazards, and (5) compilation of a succinct and complete guidance document that can readily be implemented within the pipeline industry.

These activities are divided into 7 main tasks, each led by a member of the research team:

- Task 1: Definition of Large Ground Displacement Hazards [DGHC]
- Task 2: Improved Pipeline/Soil Interaction Modeling [C-CORE]
- Task 3: Improved Pipeline Response Modeling [C-CORE]
- Task 4: Use of Pipeline Geometry Monitoring to Assess Pipeline Condition [SSD]
- Task 5: Options to Mitigate Risks of Large Ground Displacement [DGHC]
- Task 6: Comprehensive Guidance Document [PRCI, C-CORE, DGHC, SSD]
- Task 7: Reporting and Administration [PRCI]

1.2 C-CORE Project Overview

C-CORE is responsible for Task 2: Improved Pipeline/Soil Interaction Modeling and Task 3: Improved Pipeline Response Modeling. It has also contributed to subtask 5.3 of Task 5: Options to Mitigate Risks of Large Ground Displacement.

1.2.1 Improved Pipeline/Soil Interaction Modeling

Task 2 has examined the current state-of-practice to analyze pipeline/soil interaction for long-term ground movement hazards associated with subsidence and slope movement. A key issue is the significance of coupled soil deformation mechanisms (e.g. combined axial-lateral soil deformation mechanisms) during oblique pipeline/soil interaction events. This task has integrated a physical modeling program with the development of calibrated numerical models using continuum finite element methods. A numerical sensitivity analysis examined a range of practical design parameters (e.g. diameter, burial depth, soil properties, loading magnitude, etc.). Normative design curves are developed that characterize soil load-displacement relationships for coupled behaviour during oblique loading events. The pipeline/soil interaction modelling procedures advanced in this study will provide an improved basis to evaluate pipeline mechanical response and assess the suitability of potential mitigation strategies. Engineering guidelines on the integration of improved pipeline/soil interaction modeling procedures within current industry practice will be continued under Task 6.

The Task 2 activities described in this report include:

- Task 2.1 An update assessment of engineering practice to analyze pipeline/soil interaction events for long-term subsidence and slope movement hazards

- Task 2.2 Develop numerical procedures to conduct preliminary analysis on the significance of coupled soil deformation mechanisms for oblique loading events during pipeline/soil interaction in advance of the experimental program
- Task 2.3 Conduct centrifuge model experiments on oblique axial-lateral pipeline/soil interaction in clay (cohesive) soil conditions
- Task 2.4 Calibrate numerical procedures based on physical test data and conduct a parametric analysis on oblique axial-lateral pipeline/soil interaction in clay (cohesive) soil conditions
- Task 2.5 Conduct centrifuge model experiments on oblique axial-lateral pipeline/soil interaction in sand (frictional) soil conditions
- Task 2.6 Calibrate numerical procedures based on physical test data and conduct a parametric analysis on oblique axial-lateral pipeline/soil interaction in sand (frictional) soil conditions
- Task 2.7 Preparation of this interim engineering report on physical modeling, numerical analysis and improved pipeline/soil interaction models with guidance on the integration of improved pipeline/soil interaction modeling procedures within current practice.

1.2.2 Improved Pipeline Response Modeling

Under Task 3, the significance of numerical procedures that account for alternative soil spring formulations (e.g. coupled soil deformation mechanisms from Task 2), pipeline mechanical behavior (e.g. stress-strain relationships for defining pipe bend behavior under combined loading) and continuum pipeline/soil interaction behavior (e.g. soil pressure, pipeline sectional response) on pipeline response is examined. The adequacy and effectiveness of current industry practice to address these issues for long-term ground movement hazards, such as subsidence and slope movement is investigated. Recommended guidelines will be developed to identify design conditions where more sophisticated pipeline/soil interaction and pipeline response modeling techniques are warranted under Task 6 in consultation with the research team.

The Task 3 activities described in this report include:

- Task 3.1 Evaluate alternative spring formulations, which define more realistic soil load-displacement behavior, on pipeline response through structural-based and continuum finite element methods

- Task 3.2 Evaluate alternative pipeline formulations, which accounts for specific pipeline mechanical behavior on pipeline response through structural-based finite element methods
- Task 3.3 Evaluate the significance of continuum behavior (e.g. soil pressure, local ground deformations, local pipeline mechanical response) through continuum finite element methods
- Task 3.4 Preparation of this interim engineering report (section 6) on improved pipeline response modeling with guidance on appropriate selection, application, and integration of more sophisticated engineering modeling procedures in current practice

1.2.3 Options to Mitigate Risks of Large Ground Displacement

C-CORE is responsible under this Task 5 to "Assess Current Practice for Remote Sensing Applications" as Task 5.3. This subtask is reported below in Appendix B, and has been integrated into the PRCI geohazard report prepared by DGHC.

2 LITERATURE REVIEW

2.1 Scope

This section presents an assessment of engineering practice to analyze pipeline/soil interaction events for long-term subsidence and slope movement hazards A comprehensive literature review covering the main aspects encountered in modelling pipe-soil interaction was presented in the C-CORE (2003) report to PRCI. This section reviews the recent PRCI guidelines by Honegger and Nyman (2004) and summarises recent advances in the area of pipe-soil interaction modelling since 2003. Due to importance of the oblique pipe movement in the current study, experimental and theoretical studies corresponding to this issue are covered in Section 2.7.

2.2 Current Design Practice

For a buried pipeline, loads are induced in the pipeline when differential motion between the pipeline and the surrounding soil occurs. In current engineering design practice, it is prevalent to consider the soil-pipeline system as a combination of structural beam elements (representing the pipe) and spring elements in three perpendicular directions (representing the soil resistance in three directions, i.e. axial, transverse horizontal and transverse vertical directions) as shown on the pipe section right hand side of Figure 2-1 These springs represent soil resistance against pipe movement in three orthogonal directions. Typically a finite element method is used to assess the pipe response to ground movements imparted to the pipe through the soil springs as indicated.

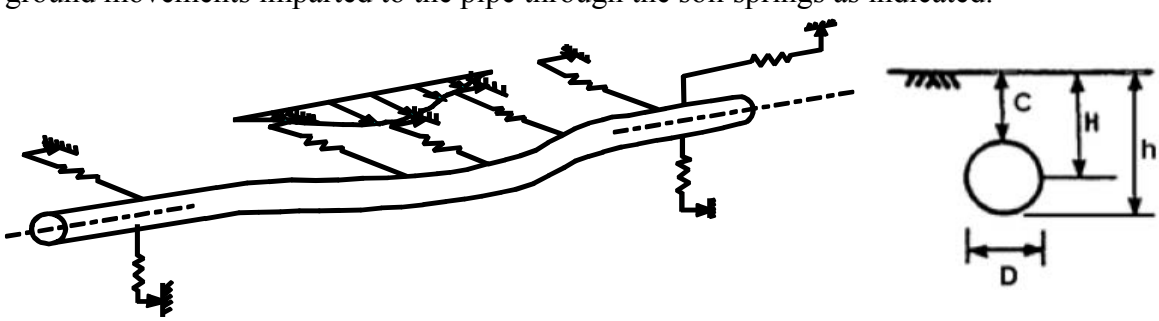

Figure 2-1 Idealization of pipe-soil interaction based on structural models.

The stress-dependent load-deformation characteristics of the springs are denoted by *t-x*, *p-y*, and *q-z* curves, as expressed by the following equations.

$$t = f_x(x)\,,\; p = f_y(y)\,,\; q = f_z(z) \qquad (2\text{-}1)$$

where *t, x* (axial); *p, y* (lateral); *q, z* (vertical) are the soil forces per unit pipeline length and pipeline displacement in the directions indicated.

Table 2-1 Soil spring relationships, Honneger and Nyman (2004)

Relationship	**Soil types and comments**
Axial spring: $t = \pi D \alpha c + \pi D H \bar{\gamma} \left(\frac{1+K_0}{2} \right) \tan \delta$	For granular and cohesive soils, where : $\alpha = 0.608 - 0.123c - \frac{0.274}{c^2+1} + \frac{0.695}{c^3+1}$
Lateral spring: $p_u = N_{qh}\, \gamma' H\, D + N_{ch} c D$ where N_{ch} = horizontal bearing capacity factor for cohesive effects (0 for c = 0), N_{qh} = horizontal bearing capacity factor for frictional effects (*0* for $\phi = 0°$)	For granular and cohesive soils. Polynomial fits to Hansen (1961) expressions for N_{ch} and N_{qh} are recommended. N_{qh} can be interpolated for ϕ between 20° and 45°. $y_u = 0.04(H + D/2)$, but not more than $0.10D$ to $0.15D$.
Downward vertical spring: Based on bearing capacity theory in which the pipeline is assumed to act as a cylindrically-shaped strip footing: $q_u = cN_c D + \gamma' H N_q D + \frac{1}{2} \gamma D^2 N_\gamma$ Bearing factors N_c, N_q and N_γ can be derived from procedures proposed by Meyerhof (1955), depending on the soil strength.	For granular and cohesive soils, the downward *q-z* curve can be represented by a hyperbolic or bilinear relationship. The ultimate soil resistance, q_u, is generally considered to occur at a displacement, z_u, of 10% and 20% of the pipeline diameter for granular and cohesive soil respectively.
Upward vertical spring:: General expression for soils due to cohesion and friction: $q_u = cN_{cv} D + \gamma' H N_{qv} D$	For granular and cohesive soils.

Figure 2-1 inset shows four common dimensions related to the pipe and its location including pipe diameter *D*, pipe cover depth *C*, burial depth *H* and embedment depth *h*. Usually, the soil force-displacement relationships are nonlinear and there exist upper limits for *t*, *p* and *q*. In this simplification, normally all soil springs are independent and the effect of shear transfer between adjacent soil springs is neglected. One of the critical tasks in the beam-spring model for buried pipelines is to determine the expressions for

the soil resistance functions f_x, f_y and f_z. Hyperbolic and bilinear forms are usually adopted to express these functions (e.g., Honegger and Nyman 2004).

The ASCE (1984) guideline was the standard reference for pipe design against seismically induced ground movement, including recommendations for these expressions This guide has been replaced by the ALA (2001) 'Guidelines for the design of buried steel pipe' prepared under contract to the American Lifelines Alliance, a public-private partnership between the Federal Emergency Management Agency (FEMA) and the American Society of Civil Engineers (ASCE).

The expressions presented in this new ALA guide are essentially those developed for PRCI in draft guidelines proposed by Honegger and Nyman (2001). This PRCI draft was finalised as Honegger and Nyman (2004). The soil spring response expressions are summarized in Table 2-1. The nomenclature is defined by Honegger and Nyman (2004).

2.3 Axial Response

The axial spring resistance, *t* in Table 2-1 is comprised of cohesive and frictional components. Care should be taken in combining these components as they are referenced to opposite extremes of pipe loading rate. The cohesive term is referenced to undrained soil response under rapid pipe loading rates. The frictional term is referenced to drained soil response that is associated with slow pipe loading rates.

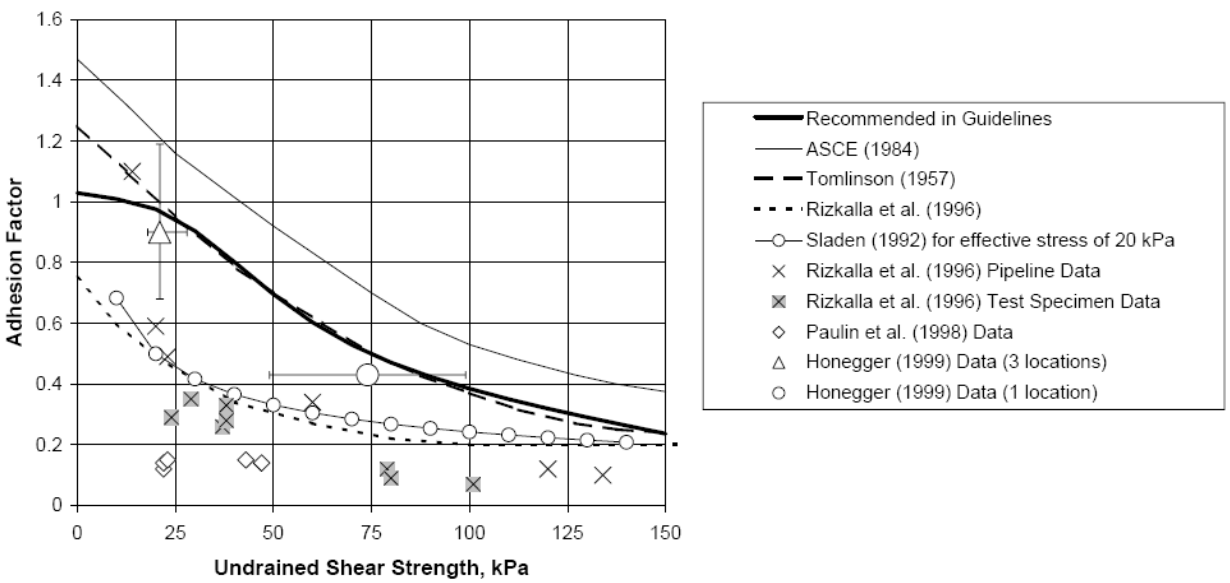

Figure 2-2 Adhesion factor for buried pipes in cohesive soils (after Honegger and Nyman 2004).

Honegger and Nyman (2004) recommend the adhesion factor, α curve developed by Honegger (1999) based on his field observations as shown in Figure 2-2. The pipe tests of Rizkalla et al. (1996), Sladen (1992) and Paulin et al. (1998b) yield much lower values. Phillips et al (2004) suggest that this discrepancy is partly due to slight axial misalignment which can significantly increase the mobilised axial resistance. Further evidence for this suggestion is presented in the following sections of this report. High α values can also result from high pore water suctions and cementation effects adhering the soil to the pipe. These pore suctions can arise either from initial hydrogeological conditions, such as low water table or dessication, or may be induced from rapid shearing of dense or overconsolidated soil.

Finch (1999) suggests that for clays with low shear strength, α values should be 1.0 for peak resistance and about $1/S_t$ where S_t is the sensitivity of the soil for a residual strength. Using axial resistance based on shear strength implies a uniform strength along the length in areas of uniform backfill. This is not the reality. Cathie et al (2005) note for submarine pipelines that seabed features and out-of-straightness have the effect of increasing the apparent frictional resistance due to high pressures on supporting areas.

It is usually assumed for seismic events that no drainage occurs during the process of relative pipe-soil movement and the axial soil restraint on pipe is based on the adhesion between the soil and the pipe. Finch et al. (2000) consider it common practice to assume that operational loads develop relatively slowly (e.g. over a period of hours for temperature increases) and that both sands and clays can be treated as drained for axial loading.

Field tests analysed by Cappelletto et al. (1998) and Scarpelli et al.(1999) show that the guideline (i.e., assuming undrained soil condition) significantly overestimates the longitudinal interaction force for buried pipes in cohesive soils and that using an effective stress approach (i.e., β method) is more reliable in this respect. The ultimate resistance is defined as $t_u = \pi D f_s$ after Cappelletto et al. (1998). The coefficient f_s is obtained from α or β method. The α-method considers a total stress analysis: $f_s = \alpha c_u$ Whereas in their effective stress analysis (β-method): $f_s = 0.5\gamma' H(1+K_o)\tan\delta = \beta\sigma_v'$

The frictional resistance component both in the new guidelines and Cappelletto et al. (1998) is assessed from an estimate of the initial effective stresses acting around the pipe. The expression used for obtaining axial pipe-soil interaction requires careful and reasonable estimation of coefficient K_0 (ratio of lateral to vertical effective stresses) and of the pore water pressure conditions. It is usually assumed that this K_0 coefficient is equal to the coefficient of lateral earth pressure at rest. Karimian (2006) measured axial soil loads on pipes in loose sand which were comparable with those calculated using the new PRCI guidelines. He found this guideline may result in underestimation of the ultimate transient soil resistance on buried bare steel pipelines in dense sand. He associated the increased resistance with dilation of the sand adjacent to the pipe. Paulin et al (1998b) found a good comparison between peak axial resistance and the guideline in a more dilatant sand against polyethylene coated pipe. The observed difference may be related to the pipe coating.

The weight of buried pipelines should also be considered for determining friction forces acting on the pipelines (e.g., Dutch code NEN 3650 1991). Finch et al. (2000) consider the frictional resistance arises from the pipe weight and the normal stresses on the top, bottom and sides of an equivalent square:

$$\sigma' = 0.25\left[\gamma' H + 2K_a\gamma'\left(H + \frac{D}{2}\right) + \gamma' H + \left(\frac{W'}{D}\right)\right]$$

so that the axial resistance of a buried pipe is: $P_x = \mu \cdot \pi \cdot D \cdot \sigma'$

The active earth pressure coefficient K_a is used which is lower than K_0. Phillips et al (2004b) and this report consider that the normal stress should include the mobilised vertical and lateral bearing pressures, p & q acting on the pipe surface.

The axial resistance between the pipe and soil may need to be reduced in some situations. A study of the geosynthetic-wrapped pipelined by Karimian (2006) indicated that geosynthetic layers are effective in reducing the axial soil loads. In fact, these layers reduce the pipe soil interface friction. Karimian (2006) also stated that these layers prevent the opportunity for dilation at the geosyntheic-interface during shear deformations as mentioned earlier. Assessment of the use of geosynthetic layers for reducing pipe soil interaction forces are reported by Honegger et al. (2006) based on the experiments conducted by Karimian (2006).

2.4 Transverse Horizontal Interaction

The lateral spring resistance, p in Table 2-1 considers the contribution of the soils cohesive and frictional strength. The associated bearing factors N_{ch} and N_{qh} are taken as

polynomial fits to the factors assessed by Hansen (1961), Figure 2-3 depending only on relative burial depth and soil strength, The contribution from soil weight, such as included in the downward vertical resistance is not included in the lateral resistance. Phillips et al (2004a) in summary of C-CORE (2003) demonstrate that the N_{ch} term should include consideration of the soil weight and be capped above a certain relative pipe burial depth, as follows: $N_{ch} = \min\left(N^{*}_{ch} + 0.85\frac{\gamma H}{c_u}, N^{\max}_{ch}\right)$

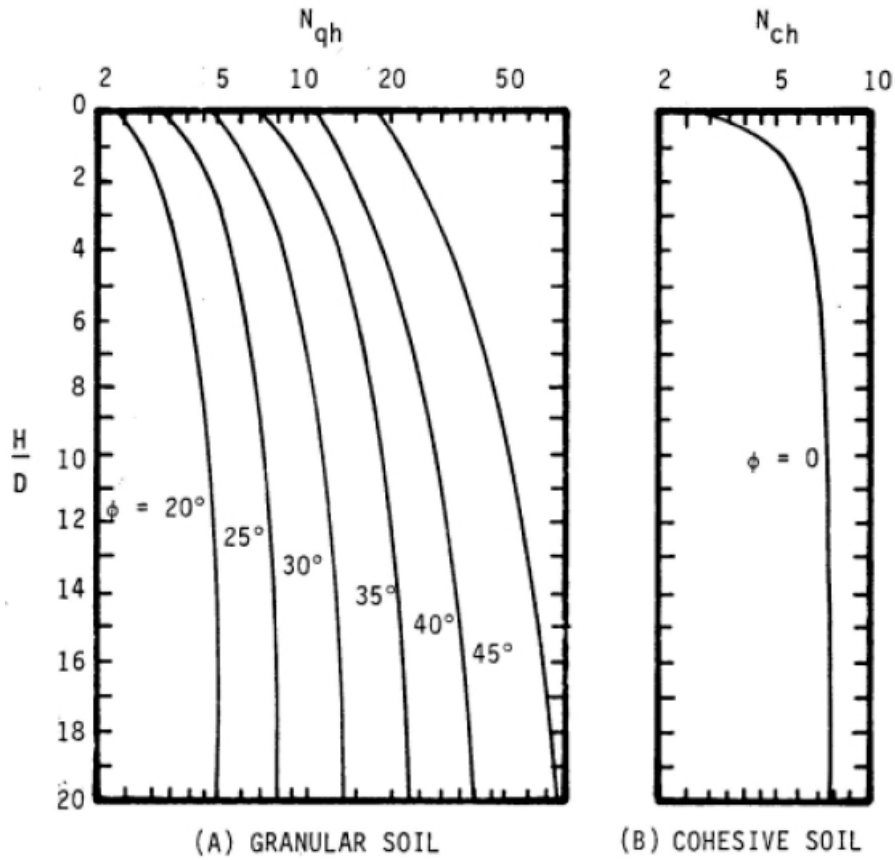

Figure 2-3 Lateral bearing capacity factors, Hansen (1961)

Cathie et al (2005) make a similar demonstration for homogeneous cohesive soils. The ultimate lateral resistance of buried pipelines can be based on the work of Merifield et al. (2001) for plate anchors: $P_y = N_{yu} D\, s_u + \gamma' D(H+D)$ where the dimensionless factor N_{yu} depends on the embedment of the pipeline and to a lesser extent on its surface roughness. There is also an upper limit imposed on P_y to reflect the transition from shallow to deep behaviour.

Centrifuge experiments conducted on buried pipelines in clay (Paulin 1998) revealed that the ultimate lateral pipe-soil interaction force increases by decreasing the loading rate. In contrast, centrifuge experiments performed by Krstelg (1996) on saturated dilative sand showed an opposite trend. These tests confirm that pipe-soil interaction forces increase with increase in loading rate for dilative soils, while the opposite is true for contractive soils. The tendency of soil materials to compact or dilate under shear can significantly influence the observed behaviour. Phillips et al (2004b) proposed a normalization of the pipe loading rate based on the soils consolidation properties to assess the transition from undrained (rapid) to drained (slow) loading conditions, Figure 2-4. The physical measurements of Paulin et al (1996) are compared with the range of finite element results bounded by the solid and dashed lines.

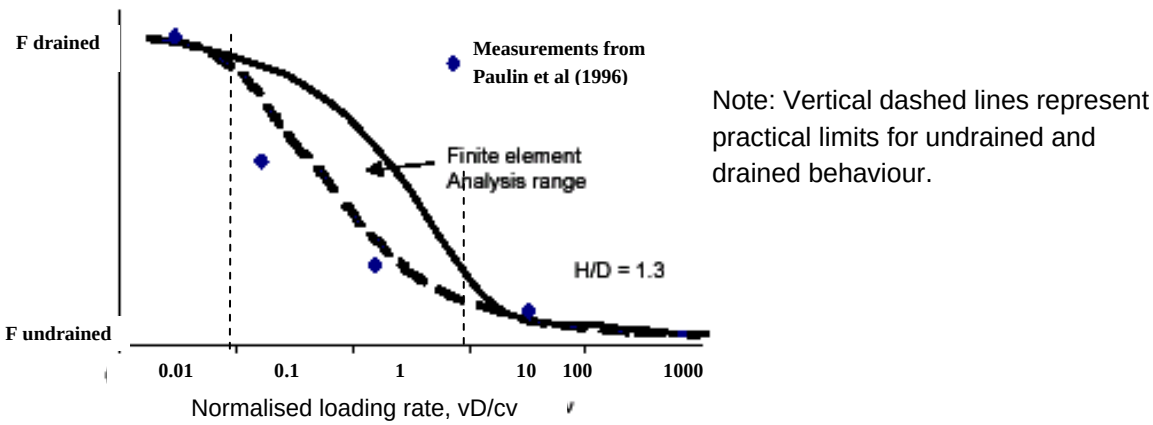

Figure 2-4 Lateral pipe response in clay from Phillips et al (2004b)

In sand, the relative density significantly influences the lateral and longitudinal interaction force based on large scale laboratory tests conducted on buried pipelines, Paulin et al., (1998b). These laboratory tests indicate that the guidelines based on Hansen (1961) may overestimate the maximum soil loads, Honegger and Nyman (2004), who mention that there might be a number of technical issues in these tests related to modeling similitude and loading rate that require resolution and further investigation.

More recent full scale laboratory tests conducted on buried pipelines in dense sand by Karimian (2006) have confirmed Paulin et al. (1998b) observation, Figure 2-5. His test results are also better predicted using N_{qh} bearing factors proposed by Trautman & O'Rourke (1985).

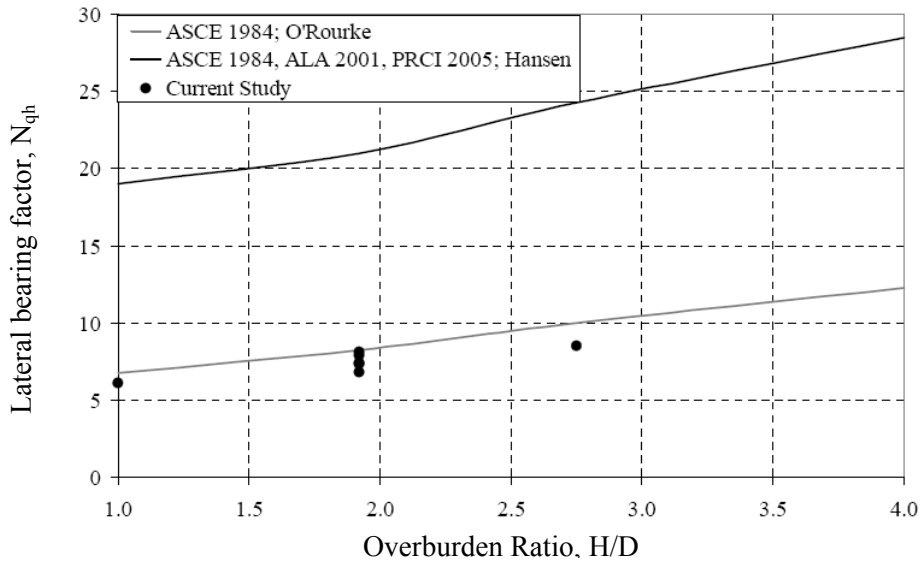

Figure 2-5 Lateral pipe response in sand from Karimian (2006)

Trautman & O'Rourke (1985) show for loose and medium dense sands, N_{qh} increases approximately linearly with the embedment for H/D < 8, whereupon N_{qh} becomes constant, indicative of the transition from shallow to deep soil failure mechanism. For dense to very dense sands, the transition was not reached at H/D of 11. This transition should be considered in the guideline.

Yimsiri et al (2004) developed well calibrated finite element analyses of the pipe response due to lateral and upward movements in sand, using the FE code ABAQUS with two different constitutive models: Nor-Sand (Jefferies, 1993) and Mohr-Coulomb model. They first simulated the experimental tank tests conducted by Trautmann and O'Rourke (1983) to validate the numerical model and then extended their study for deep embedment ratios (up to 100).

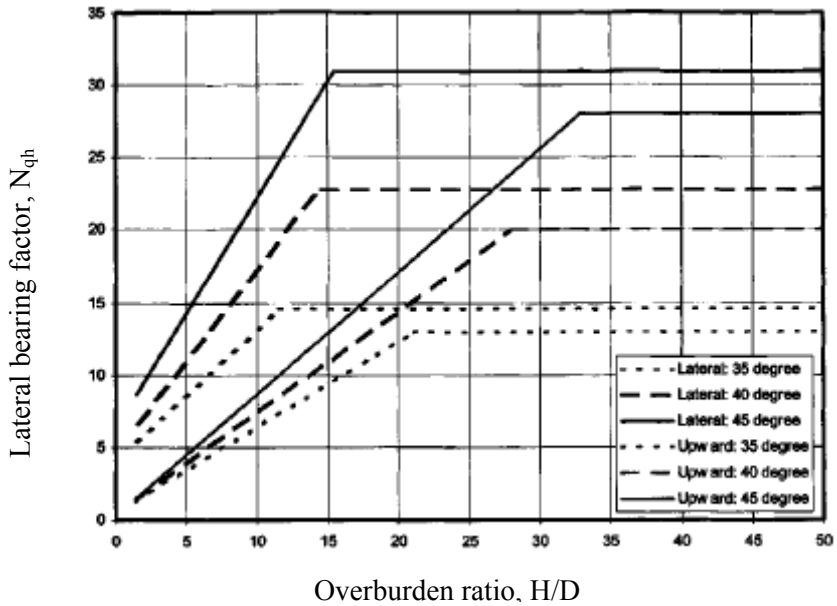

Figure 2-6 Lateral pipe bearing factors in sand from Yimsiri et al (2004)

At their transition for lateral pipe movement in Figure 2-6, the critical peak dimensionless forces N_{qh} are 14, 22, and 30 at H/D of 12, 15, and 16 for peak friction angles of 35°, 40°, and 45°, respectively. For upward pipe movement, the critical peak dimensionless forces N_{qu} are 13, 20, and 28 at H/D of 21, 28, and 33 respectively. The results can be used to estimate the peak dimensionless forces of pipeline at deep embedment conditions, which is not given in the guideline.

Turner (2004) report the results of a further thirty full-scale lateral loading tests at Cornell on a model pipe buried in sand with different water contents (0, 4 and 8%). Burial depths of 6 and 8.5 pipe diameters represented shallow embedment and burial depths of 15.4 and 19.7 pipe diameters represented deep embedment. The experiments conducted in partially saturated sand resulted in considerably higher values for the maximum lateral force than those obtained in case of dry sand with similar dry unit weight and friction angles, Figure 2-7.

.

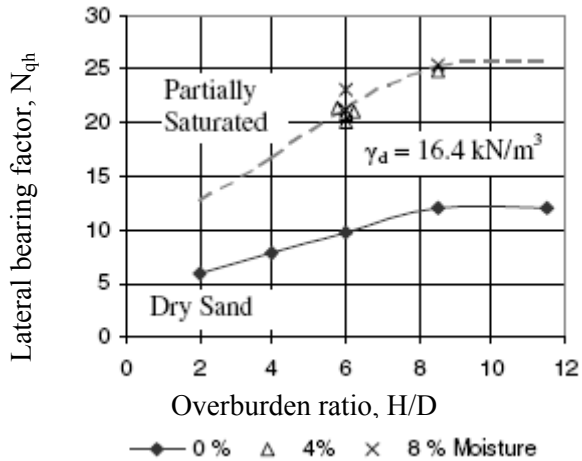

Figure 2-7 Lateral pipe bearing factors in dry and moist sand from Turner (2004)

O'Rourke (private communication) has since noted that side wall friction in the test tank skewed these observations, and that there was no difference between moist and dry sand behaviour under comparable conditions in more recent, unpublished tests. Karimian (2006) has also seen no significant difference when comparing moist and dry sand lateral pipe test results.

The lateral bearing factors for sand proposed by Audibert and Nyman (1977) and Trautmann and O'Rourke (1985) as compared in Figure 2-5, were both developed from experimental observations. Guo and Stolle (2005) present a comprehensive review on the lateral pipe-soil interaction for buried pipelines in sand to understand the underlying difference between these proposals. They compared the experimental bearing factors, N_{qh} (N_h) obtained from Akinmusuru (1978), Audibert and Nyman (1977), Neely et al (1973), Smith (1962), Trautmann & O'Rourke (1985) and others, Figure 2-8. A size effect, that is a reduction in N_{qh} with increasing pipe diameter, was observed similar to that observed by De Beer (1970) for footings on sand.

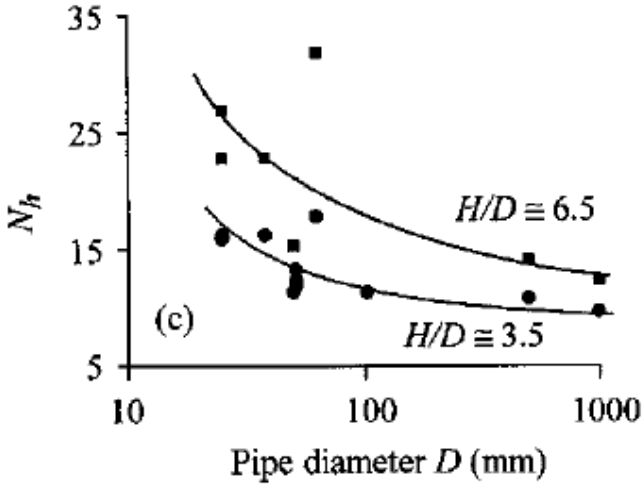

Figure 2-8 Experimental lateral bearing factors in dry sand, Guo & Stolle (2005)

Guo and Stolle (2005) developed a finite element analysis to account for scale effects, i.e., the effects of pipe size and burial depth. They proposed a unique equation to account for this and for soil property variations including friction and dilation. This equation compared very favourably with the experimental observations of Figure 2-8, Figure 2-9. Parameters *k*, *m*, and *n* depend upon soil properties and D_{ref} is a reference pipe diameter equal to 1m. This size effect should be considered in future guidelines.

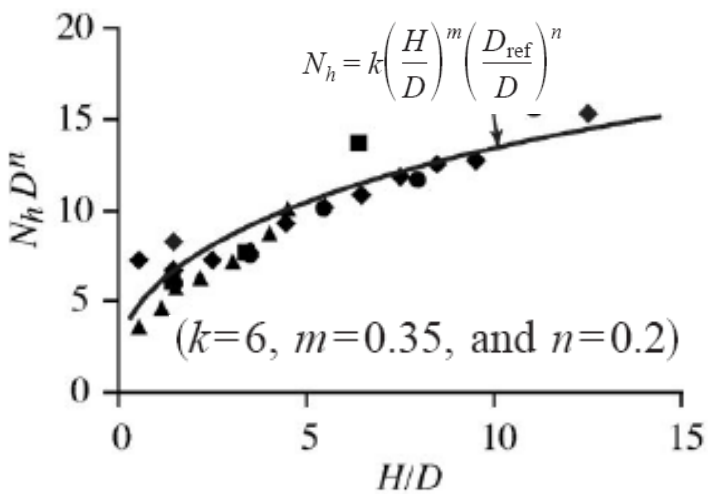

Figure 2-9 Lateral bearing factor comparison in dry sand, Guo & Stolle (2005)

2.5 Transverse Vertical Interaction

The vertical soil resistance, *q* against vertical movement of pipelines is asymmetric, Table 2-1 , unlike the pipe-soil interaction forces in axial and lateral directions. The upward vertical resistance is less than the downward resistance, due to the presence of the

less constrained soil surface. Cathie et al. (2005) present a state-of-the-art review on geotechnical issues related to soil-pipeline interaction. Their review has a comprehensive section on vertical soil resistance. They also consider partially embedded pipelines, backfilling techniques, thermal issues and stability of pipelines during trenching and backfilling as pertinent to offshore pipelines.

2.6 Pipe-Soil Interaction Modelling

The most important issues related to modelling the pipe-soil interaction phenomenon are discussed in C-CORE (2003). These include (1) ability to simulate large relative displacement of pipeline, (2) correct modelling of the pipe-soil interface behaviour, (3) selection of an appropriate constitutive model, (4) accurate estimation of the soil constitutive parameters, (5) considerations related to loading rate effects, (6) coupling effects due to oblique pipe movement, and (7) recognizing the range of applicability of the recommended guidelines in practice over a wide range of real soils.

Analytical solutions are limited to problems with simple geometries, simple boundary conditions and simple constitutive behaviour. For complicated problems numerical methods (e.g., the finite element method and finite difference method) provide a rational basis for conducting pipe-soil interaction studies.

Both structural-based (beam-spring model) and continuum-based finite element (FE) approaches have been used for analyzing pipe-soil interaction events as described in detail by C-CORE (2003). The structural-based FE models (e.g., Kim et al., 1998; and Bruschi et al., 1996) are significantly more efficient and require substantially less computational resources than their equivalent continuum analyses; however, the main issue in these models is to introduce a reliable force-displacement curve representing the resistance of the soil medium. The structural-based models used in the current design practice do not generally consider the coupling effects due to oblique (combined transverse and axial) pipe movements.

Coccheti et al (2007) have recently developed a structural FE model which includes coupling of the soil response in the vertical (V) and lateral (H) directions, Figure 2-10, through the use of ‘macroelements’. Their soil failure envelope is asymmetric in the vertical direction to account for the difference between upward and downward loading. The axial (N) response is not coupled to the assumed transverse behaviour. They present two and three dimensional analyses of a pipeline response in loose sand with a friction

angle of 30 degree and 20 degree of dilation. A comparison between coupled and uncoupled soil response is not presented.

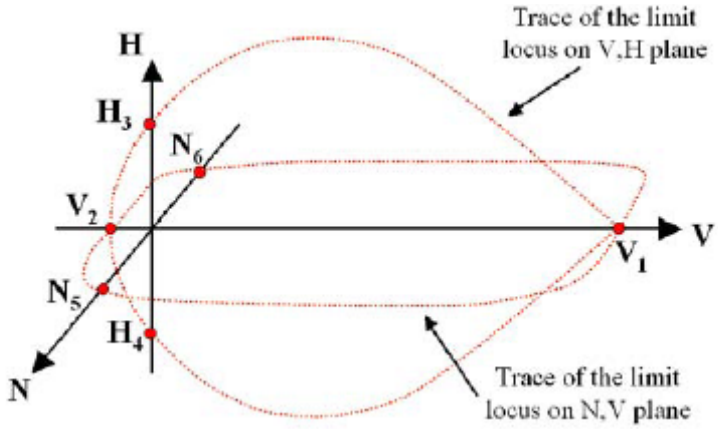

Figure 2-10 Coupled soil response, Coccheti et al (2007)

Continuum finite element models (e.g., Popescu and Konuk, 2001; Altaee et al., 1996 and Bruschi et al., 1995) are robust and comprehensive numerical tools that can address a number of limitations in the structural-based models including soil constitutive behaviour, soil deformation mechanisms (e.g. shear load transfer), soil-pipe interaction (e.g. variable circumferential or longitudinal pressure distribution), and complex pipeline response mechanisms (e.g., ovalization, or wrinkling). The most important disadvantages of the continuum finite element modelling are the demands on computational resources, limited availability of realistic soil constitutive models, and the requisite experience and knowledge of the analyst. In addition, lack of data and uncertainty in determining input parameters (soil properties) always limit the application of a more complex numerical analysis.

A continuum finite element model capable of simulating large relative displacements was developed and validated at C-CORE for pipe-soil interaction problems using the FE code *ABAQUS/STANDARD* (e.g. C-CORE, 1998; Paulin et al., 1997 & 1998b, Popescu, 1999, Popescu et al., 1999 and 2001). The model can account for material nonlinearity (both pipe and soil), relative slip/rotation and separation at the pipe-soil interface, as well as ovalization and buckling of the pipe.

Several aspects of pipe-soil interaction that are not addressed by the current guidelines have been studied to improve the existing soil spring based structural models, C-CORE (2003). These include (1) soil failure mechanism (including embedment ratio, soil type and strength, pipe loading mechanism); (2) pipeline trenching (including trench geometry and backfill vs. native soil strength ratio); (3) pipeline ovalization and collapse (including pipe

thickness-to-diameter ratio, boundary conditions, soil type, internal pressure); and (4) complex loading (including pipe translation + rotation, axial + lateral translation, axial + moment loading).

2.7 Oblique Pipe Movement

Few experimental and numerical studies have been conducted to investigate the effects of oblique pipe movement on the soil resistance, either in the transverse plane (combined vertical and lateral loading) or in combination with axial loading.

Kennedy et al (1977) recognized the effect of lateral soil pressure on increasing the axial soil resistance around curved pipe lengths. Their analyses considered this increase over that caused by 'at rest' soil pressures acting on straight pipe sections.

Guo (2005) presents a summary of previous work related to modeling the pipe-soil interaction phenomenon due to oblique pipe movement in a vertical plane (combined lateral and upward vertical). Nyman (1982) used the experimental data of Meyerhof (1973) for anchor plates and proposed the following equation, as shown in Figure 2-11, for the soil restraint force on pipe due to a combined lateral and vertical pipe movement:

$$p_{u-\theta} = (1-k)q_{u0} + kp_{u0} \quad \text{where } k = \frac{0.25\theta}{90 - 0.75\theta}$$

The oblique pipe angle, θ is measured from vertical direction and *p* and *q* are transverse horizontal and transverse vertical (upward) ultimate soil resistance per unit length of pipe, respectively. The experimental data provided by Das (1985) based on small scale tests on anchor plates buried in clay indicate $k = (\theta/90)^2$.

Guo (2005) extended the model proposed by Martin and Houlsby (2001) for foundations on clay and developed an associative hardening elastoplastic constitutive model in the *p-q* load space for pipes buried in clay. He found good agreement between the results predicted by his extended model and his continuum finite element analyses (FEM) Figure 2-11.

Guo (2005) also found the results provided by Hsu (1996) for pipelines buried in loose sand exhibit reasonable agreement with his model.

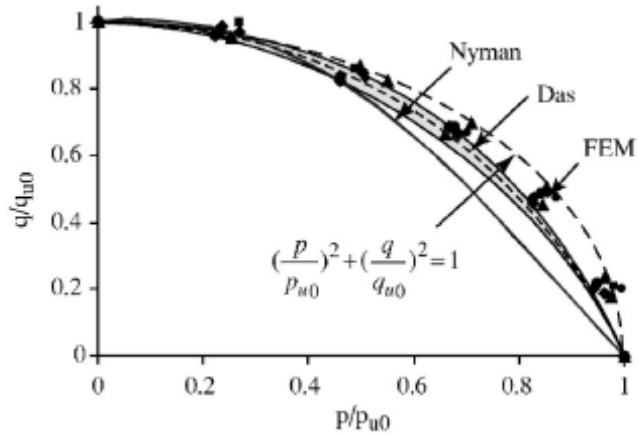

Figure 2-11 Upward vertical and lateral load interaction, Guo (2005)

Hsu (1996) studied the soil resistance due to oblique pipe movement (lateral-vertical) for a series of 1.22m long pipes of different diameters, Figure 2-12 in loose sand. His study indicated that the dimensionless ultimate force and its corresponding displacement increase with increase in oblique angle (measured from vertical direction) and embedment depth, particularly for oblique angles between 45° and 90°, and that a constant hyperbolic relationship can be used to represent the normalized force-displacement relationship.

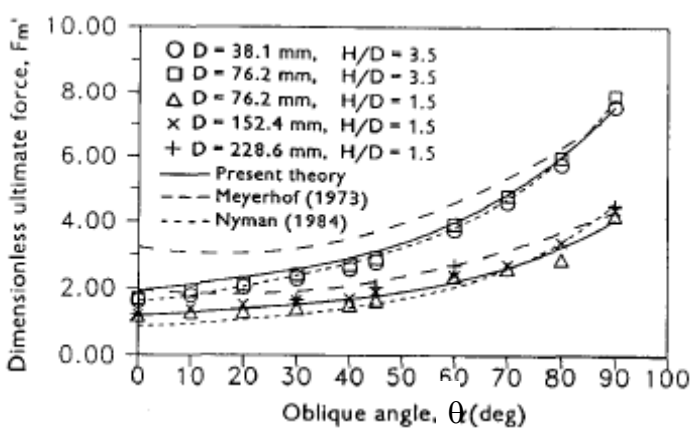

Figure 2-12 Upward vertical and lateral load interaction in sand, Hsu (1996)

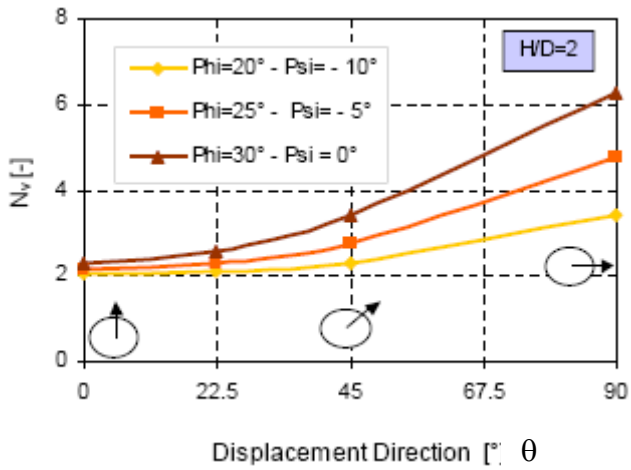

Figure 2-13 Upward vertical and lateral load interaction, Vanden Berghe et al. (2005)

Hsu (1996) test results in loose dry medium sand with a friction angle of 33 degree are consistent with recent numerical analyses by Vanden Berghe et al. (2005), Figure 2-13. They also show that there is very little difference in uplift resistance when the load direction is within about 30° of the vertical.

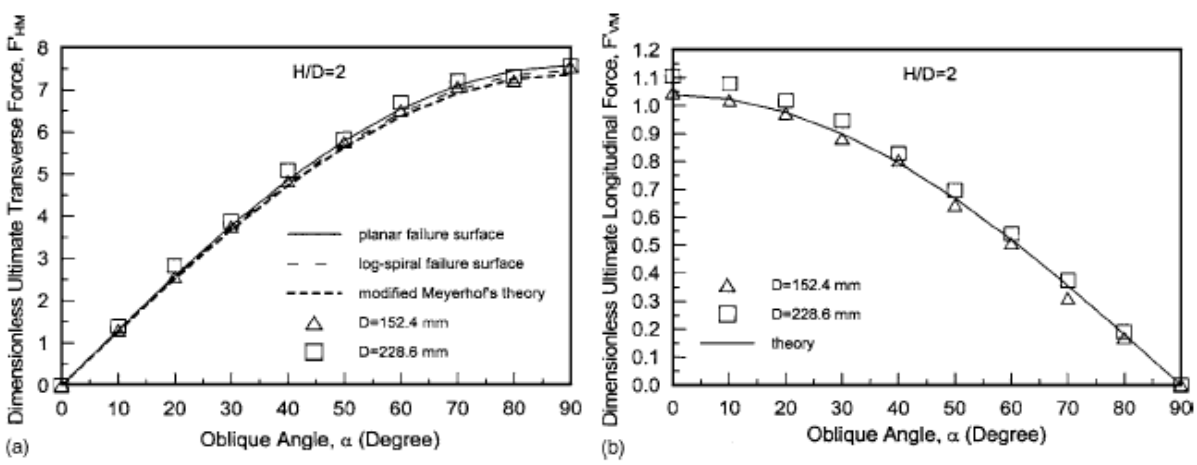

Figure 2-14 Lateral and axial load interaction in dense sand, Hsu et al. (2006)

The effects of oblique pipe movement in a horizontal plane (lateral-axial) on the soil restraints on pipes have been studied using large scale laboratory tests by Hsu et al. (2001) for pipes buried in loose sand and by Hsu et al. (2006) for pipes buried in dense sand, Figure 2-14. A pipe oblique angle, α of zero represents axial loading and an angle

of 90 degrees is for pure lateral pipe movement. They developed a closed form prediction to fit their data based on Meyerhof bearing capacity theory.

C-CORE (2003) developed a FEA model for a parametric study of pipelines buried in clay subjected to combined lateral and axial loading in cohesive soil. The study included a range of soil strengths, oblique angles, pipe displacements and pipe-soil friction angles. The normalized interaction diagrams (relationship between the normalized lateral and the normalized axial interaction forces) were found to be linear for oblique angles lower than 15°, for example Figure 3-8. For oblique angles higher than 30°, N_x tends to increase quickly while N_z decreases.

This current project has extended these analyses to verify the major aspects of pipe-soil interaction behaviour for pipes buried in sand and clay subjected to oblique movement (lateral-axial) by means of centrifuge experiments and numerical modeling, as described in sections 3 to 5.

3 MODELING OBLIQUE PIPE SOIL INTERACTION IN CLAY

3.1 Introduction

Oblique pipe soil interaction is considered in this report as a combination of axial and lateral displacement of a pipeline segment with respect to the surrounding soil, as shown in Figure 3-1. The angle α defines the direction of movement with respect to the pipeline axis.

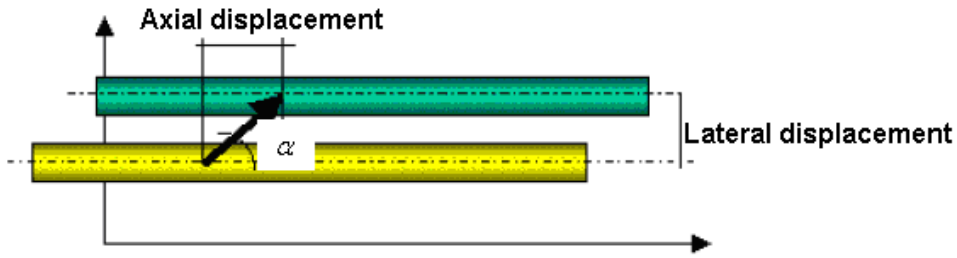

Figure 3-1 Buried pipeline subjected to oblique movement.

A finite element study of this oblique interaction in clay was initiated in C-CORE (2003) report to PRCI. The analyses presented in that report are extended to consider the effects of the interface and of path dependency that is changes in the loading direction.

Section 2.3 revealed two extremes in considering the interface behaviour in clay to be either adhesive or frictional. These extremes are also reflected in the different design guidelines. In the previous study, the pipe –soil interface was considered to be frictional. In this study, the interface is considered adhesive. The effect of this interface assumption is compared between analyses and with the physical model test results presented in section 5.6.

The path dependency analyses will confirm what, if any, additional soil resistance is available, after the soil has failed under oblique loading.

3.2 Analysis Specifications

The layout and the finite element model of the buried pipeline studied here are shown in Figure 3-2. The finite element model and methodology are described in C-CORE (2003). The pipe diameter (D) and the burial depth (H) are 0.508m and H = 2D, respectively. The pipe length in contact with soil is eight pipe diameters.

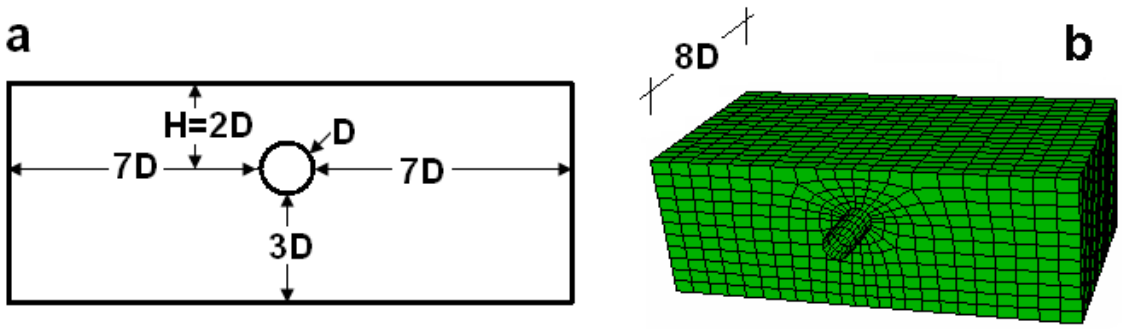

Figure 3-2 (a) Layout and (b) FE model of the buried pipe

3.3 Soil Constitutive Model

The elasto-plastic soil constitutive model is the Von-Mises model implemented in ABAQUS/STANDARD. The soil and interface parameters are listed in Table 3-1 where E = modulus of elasticity, ν = Poisson's ratio, c_u = undrained shear strength, f = coefficient of the pipe-soil interface friction, γ = specific weight, and τ = shear stress limit at the pipe soil interface. The Poisson's ratio was selected as ν = 0.49 to simulate the undrained (constant volume) soil behavior. Higher values may cause numerical difficulties.

The interface behavior is assumed to be purely adhesive. In order to mobilize this assumed shear stress limit at the interface (adhesion limit) an unrealistically large value for the coefficient of the pipe-soil interface friction was adopted in the finite element simulations. An artificial friction coefficient equal to 5 was required for the case studied here. Considering Cappelletto et al (1981) effective stress equation in section 2.3, the large friction coefficient is very much higher than measured interface friction values (tan δ). The effective stress acting on the pipeline must then be about 5 times the total stress levels, which implies pore water suction about 4 times the mean total stress level. These effective stress and pore suction levels will not occur frequently in real situations.

Table 3-1 Soil and interface constitutive parameters

Constitutive Model	Soil type	c_u (kPa)	E (MPa)	ν	f	γ (kN/m^3)	τ (kPa)
Von- Mises	Clay	40	16	0.49	5.0	17.5	25

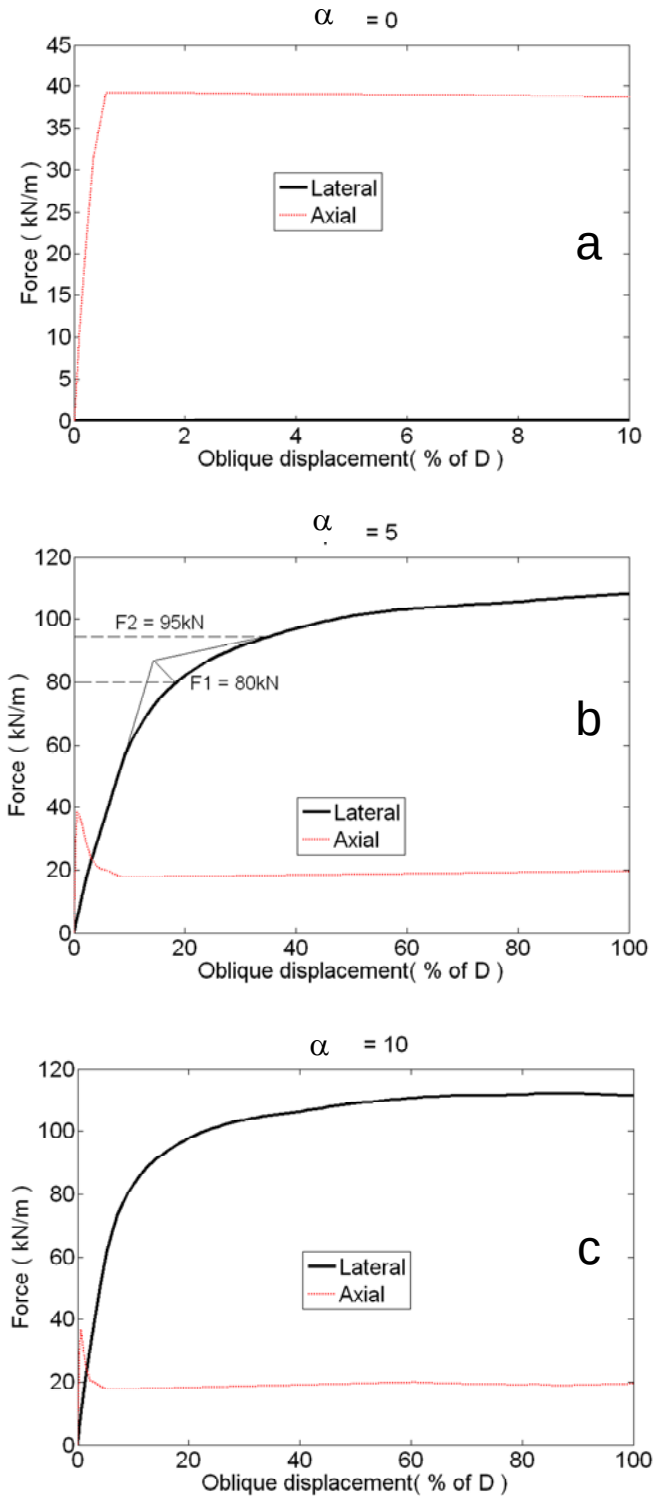

Figure 3-3 Predicted force-displacement curves for shallow oblique angles

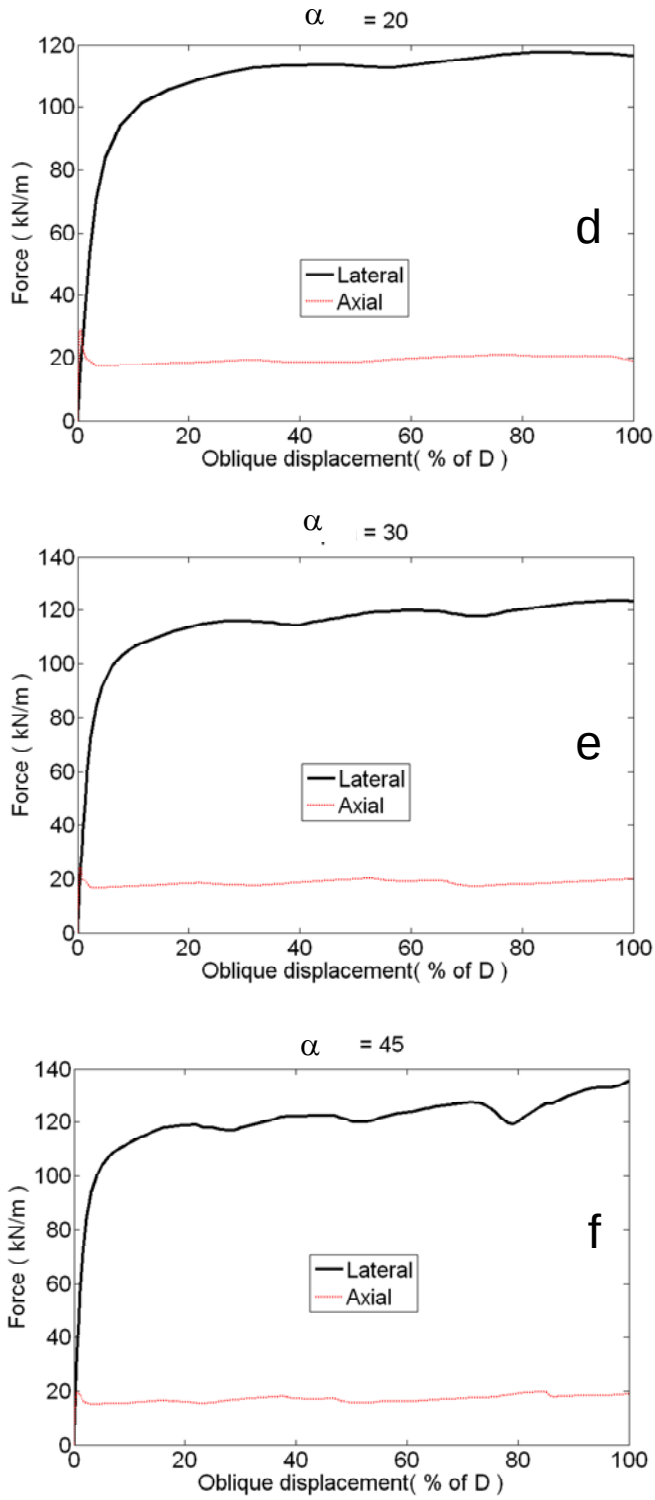

Figure 3-4 Predicted force-displacement curves for intermediate oblique angles

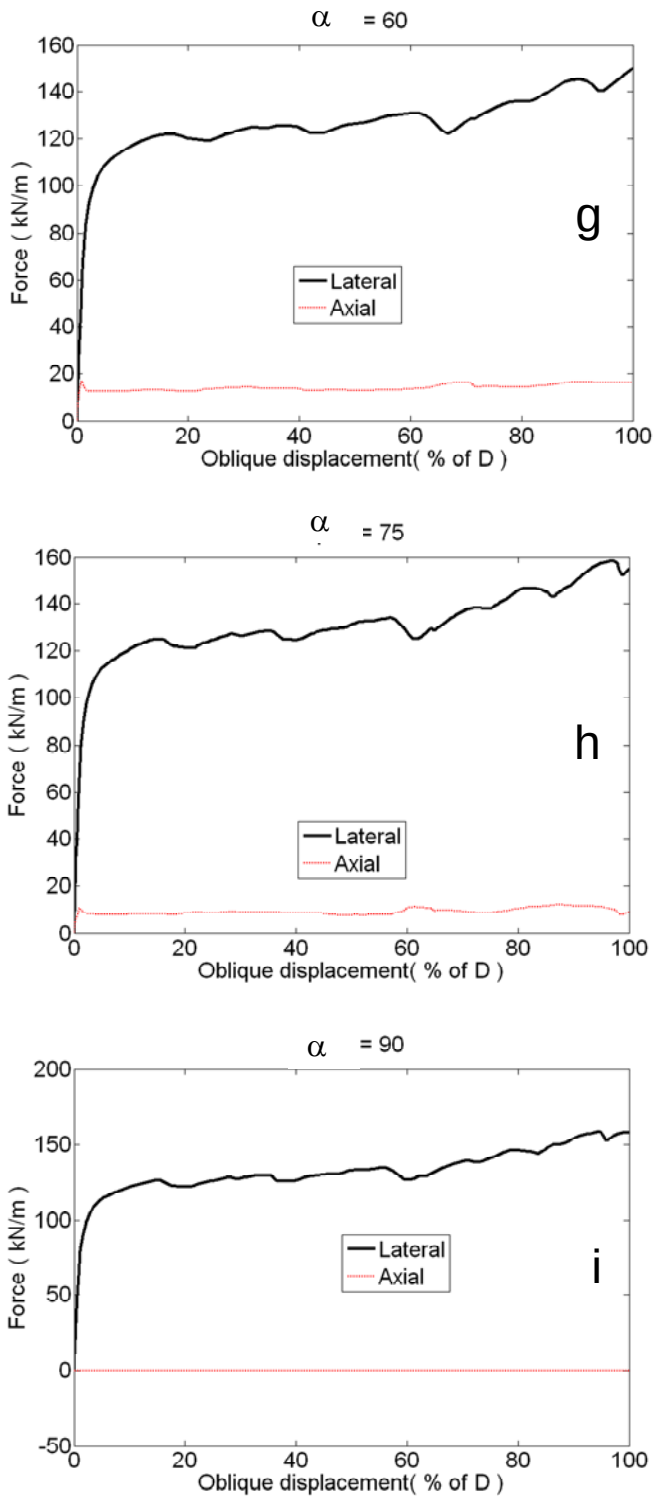

Figure 3-5 Predicted force-displacement curves for large oblique angles

3.4 Numerical Simulations For Clay

3.4.1 Loads

The loading comprises two steps: (1) a geostatic step to obtain the initial stress field within the soil medium and on the buried pipes followed by (2) an oblique pipe movement up to 100% of its diameter. The oblique α angles considered here are 0 (purely axial), 5°, 10°, 20°, 30°, 45°, 60°, 75°, and 90° (purely lateral). The numerical results are presented below for the second load step, i.e. the oblique pipe movement.

3.4.2 Numerical simulation results

The force-displacement curves obtained from numerical simulations with different oblique angles are shown in Figure 3-3 to Figure 3-5. For $\alpha = 0$ the axial interaction force obtained from numerical simulations (i.e., 39.2kN/m shown in Figure 3-3a) is in good agreement with the expected theoretical value at the interface, $\pi D \tau$ =39.9kPa. The large value for the interface friction coefficient was sufficient to simulate the required interface behavior.

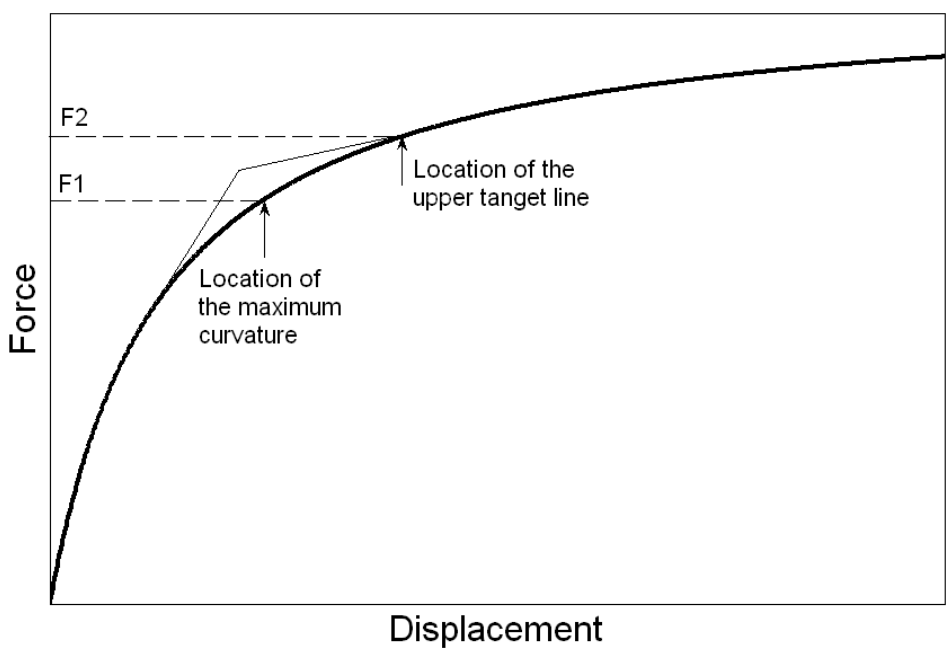

Figure 3-6 Conventions for determining the ultimate lateral interaction force.

In order to plot the interaction diagram, the ultimate axial and lateral interaction forces should be estimated from the force-displacement curves plotted in Figure 3-3 to Figure

3-5. The slight increase in lateral forces (the curves do not reach a horizontal asymptote after yielding) is related to the fact that a soil mass is pushed upward due to continued lateral pipe movement. When a force-displacement curve does not have a horizontal asymptote, a convention is required for determining the ultimate lateral interaction force. Figure 3-6 shows a typical force-displacement curve along with two conventions for determining the ultimate force from the curve. In convention #1 (represented by force F1 in Figure 3-6 and Figure 3-3b) it is assumed that the ultimate lateral interaction force corresponds to the point at which the highest curvature takes place. In convention #2 (represented by force F2 in Figure 3-6 and Figure 3-3b), two tangent lines are drawn and it is assumed that the ultimate lateral interaction force corresponds to the point at which the upper tangent line reaches the force-displacement curve. These two tangent lines can show overall inclinations of a force-displacement curve (e.g. if the curve is approximated by a bilinear function). Typical results are shown in Figure 3-3b for α of 5°.

Figure 3-5g shows cyclic variations in the force after failure. These variations are partly indicative of a sequence of failure mechanisms developing as the pipe is displaced. The upper tangent line is taken as the best fit through the backbone curve post failure, ignoring these periodic load reductions.

Using these conventions, the dimensionless interaction diagrams obtained from numerical simulations are shown in Figure 3-7. The design equation 3-1 proposed by C-CORE (2003) and presented in Phillips et al (2004b) is compared with the numerical values.

$$N_p^2 + 3N_t^2 = N_{p0}^2 \qquad (3\text{-}1)$$

Where N_p and N_t are the ultimate lateral and axial interaction forces respectively, and N_{p0} represents the ultimate lateral interaction force for α of 90° (purely lateral). The N_{p0} value of 6 is consistent with that expected from Phillips et al (2004a) for this geometry and soil conditions. The axial force design limiting value imposed by relations such as Figure 2-2 is not shown in the figure.

The interaction diagram is similar to that developed by C-CORE (2003), Figure 3-8 for oblique loading angles above 20 degree. The effect of the assumed interface behaviour is seen for lower loading angles. The adhesive limit provides a vertical cut off to the interaction diagram around a normalized axial force of 1.9. The frictional assumption of C-CORE (2003) develops very much lower axial resistances which are a linear function of the mobilised lateral resistance. The pure lateral interaction factor from C-CORE (2003) of 4.8, shown on the y-axis in Figure 3-8, is lower than the value of 6 in Figure

3-7 mainly due to size effect from smaller pipe diameter of 0.203 m. There is also a lesser influence from shallower burial and stronger soil. Phillips et al (2004a) gives N_{p0} of 5.2 for this new geometry and soil conditions, which is still slightly lower than the value of 6 obtained from these analyses.

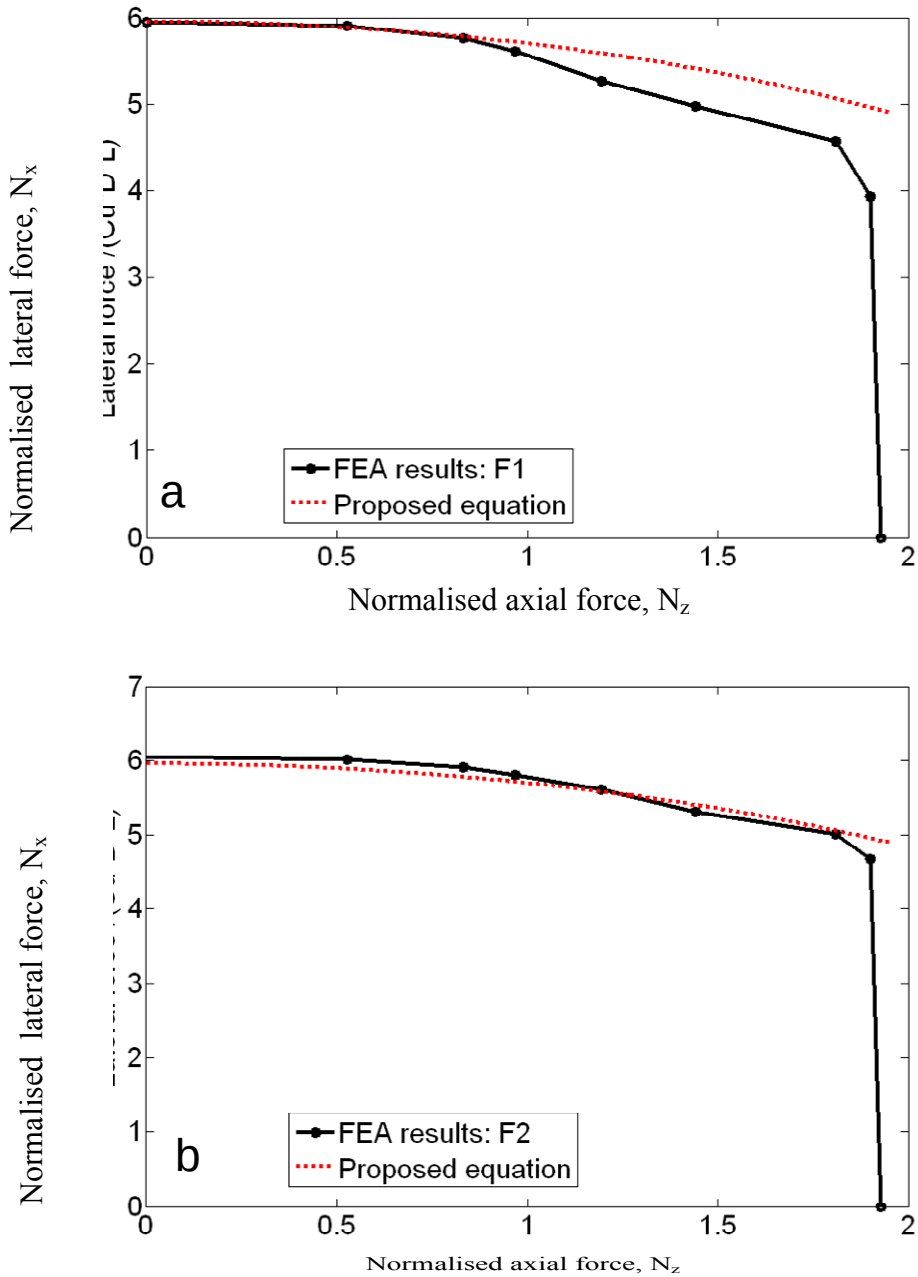

Figure 3-7 Dimensionless interaction diagram comparisons using a) convention #1, and (b) convention #2.

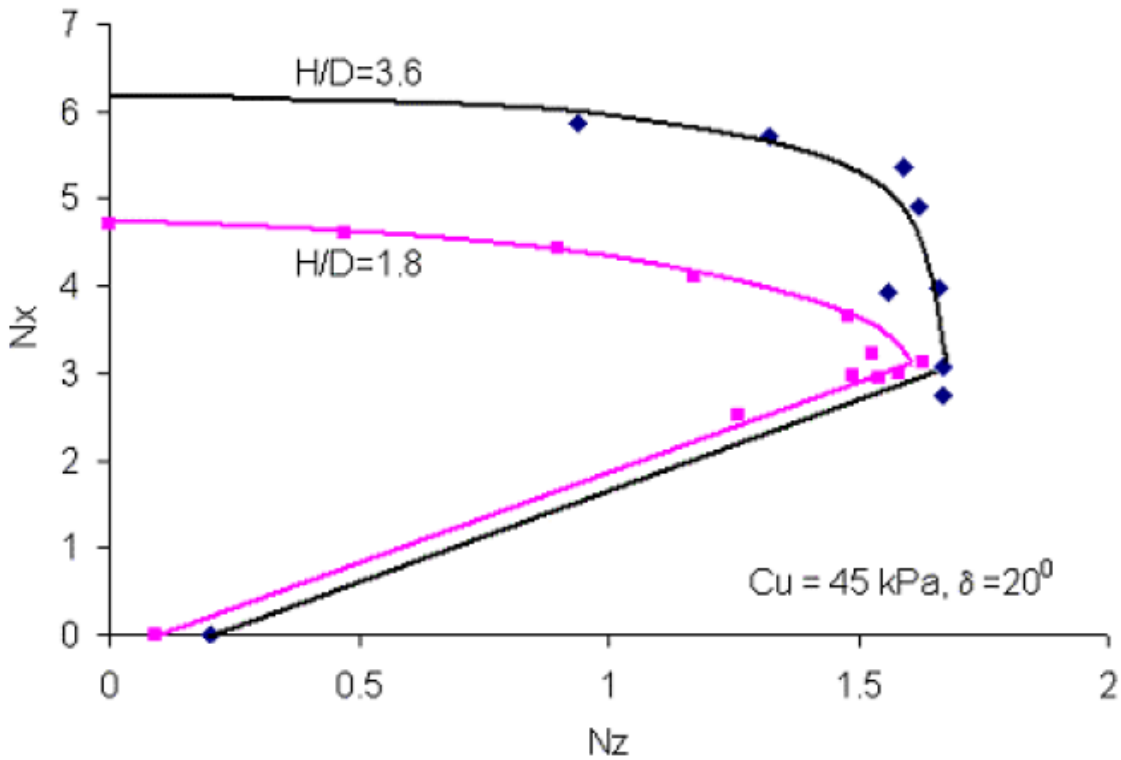

Figure 3-8 Dimensionless interaction diagrams from C-CORE (2003)

Equation 3-1 is in good agreement with the finite element analysis results when convention #2 is employed for plotting the interaction diagram. For convention #1 there are discrepancies between the predicted results and the proposed equation at low oblique angles. The convention #2 is used for assessing ultimate loads from any subsequent numerical analyses.

3.4.3 Burial depth and adhesion sensitivity

The analyses were continued to examine variations in burial depth and the interface friction coefficient. Two configurations for H/D = 1.5 and H/D = 2 were analyzed, Figure 3-9, with a lower interface friction coefficient of 1 for loading angles of 0, 10, 60 and 90 degrees. All other parameters were taken as Table 3-1.

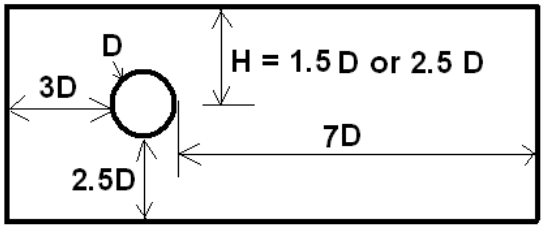

Figure 3-9 Buried pipe geometries

The numerical results corresponding to these cases are shown in Figure 3-10 and Figure 3-11. The normalized lateral interaction factors, Figure 3-11f, of 4.9 and 6.7 for the two burial depths again correlate well with those proposed by C-CORE (2003) considering both geometric and soil parameter contributions. Equation 3-1 also represents the upper failure envelope for shear failure through the soil.

The second failure envelope is seen as a cap on the normalized axial force, representing shear along the pipe soil interface. These axial limits of about 1.0 and 1.5 for the 2 burial depths, are lower than the 1.9 value obtained for H/D = 2.5, Figure 3-7. The maximum 25 kPa adhesion was therefore not mobilized in these analyses. The interface resistance was instead controlled by the assumed friction. This is confirmed by the increase in the axial limit with burial depth due to the increased self weight stresses acting around the pipe.

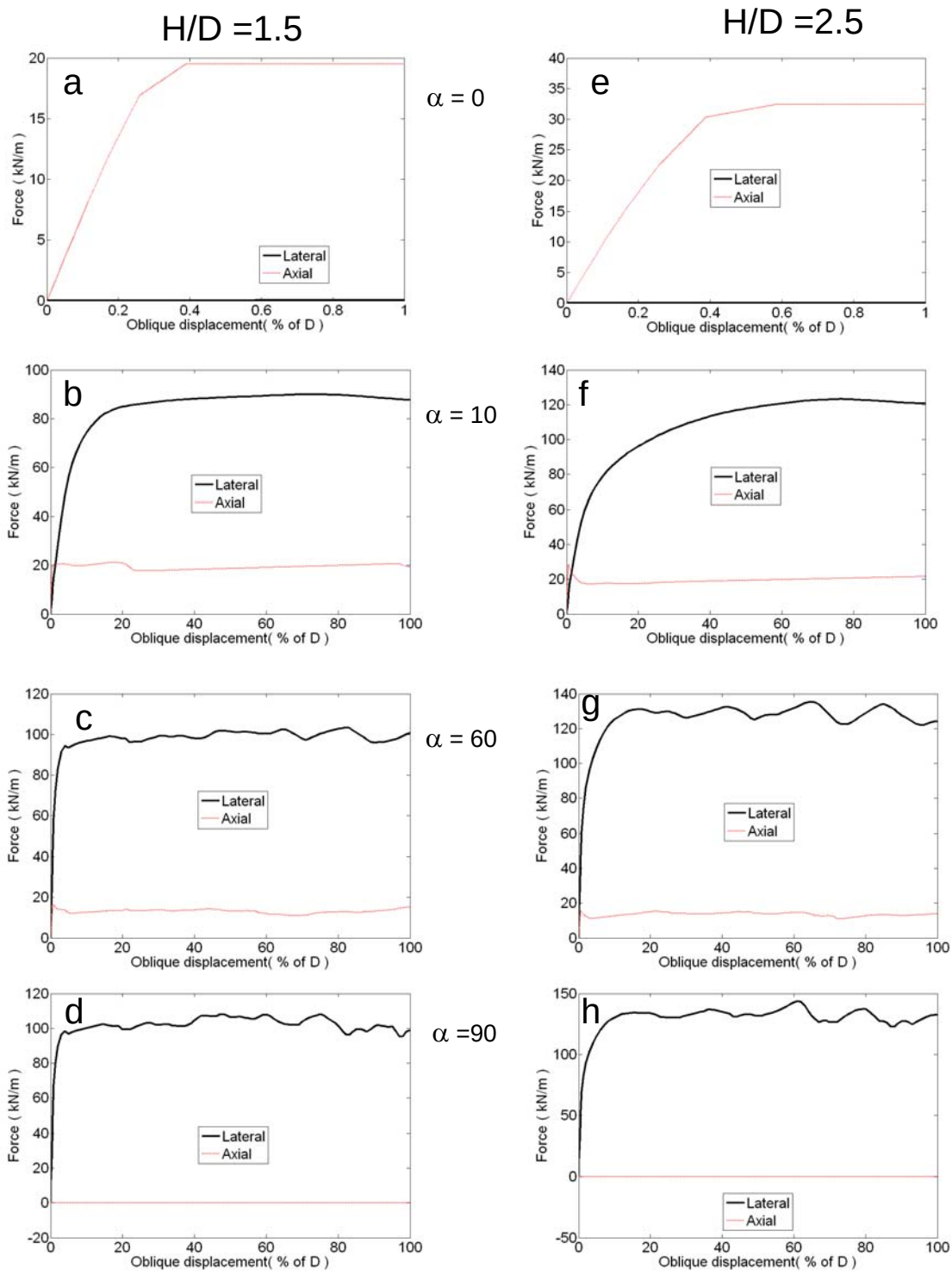

Figure 3-10 Interaction forces in clay for (a) - (d) H/D1.5 and (e) - (h) H/D2.5.

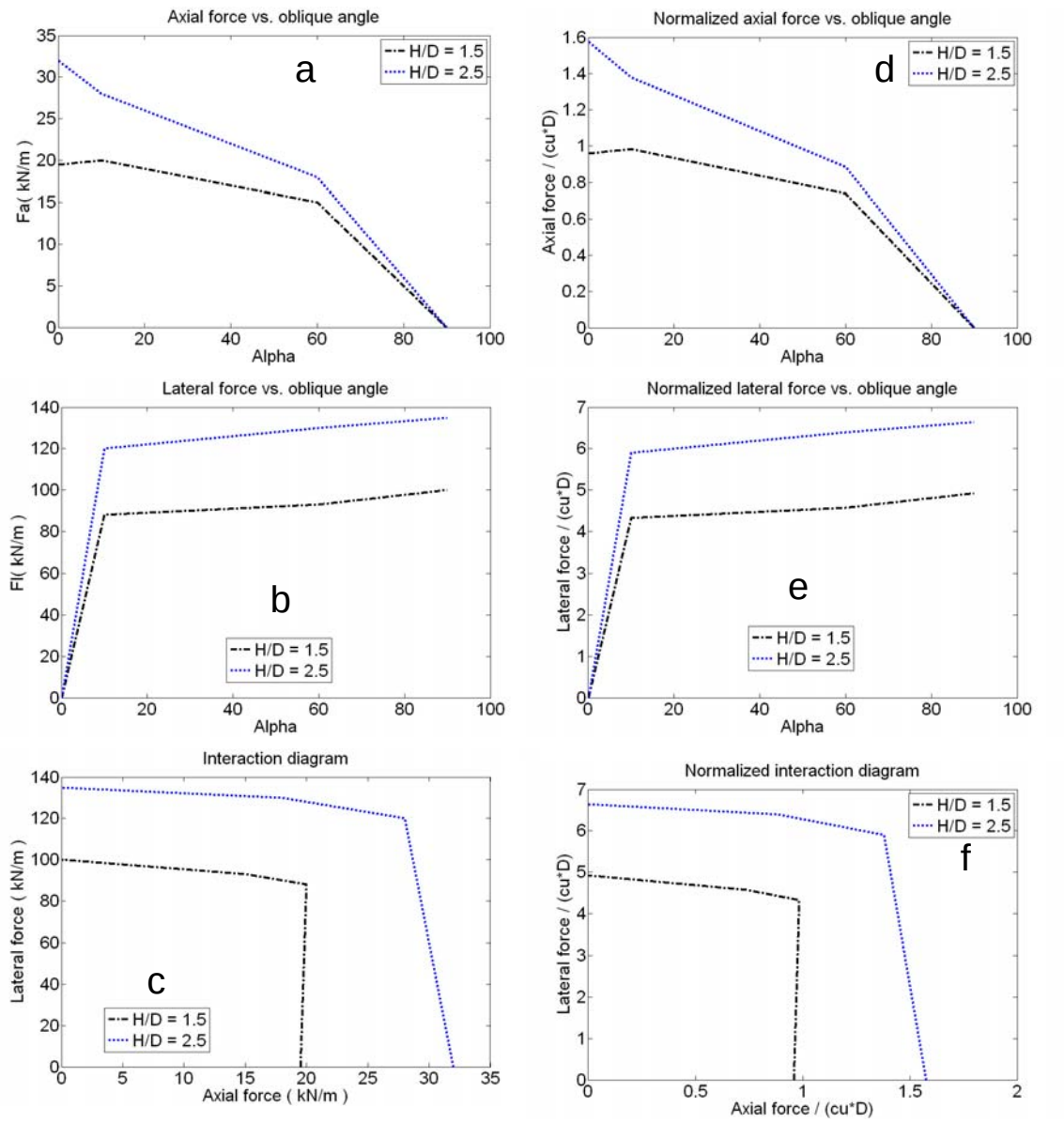

Figure 3-11 Normalised interaction forces in clay for H/D =1.5 and H/D = 2.5

3.4.4 Load path dependency

The analyses of section 3.4.2 for a burial depth H/D = 2.5 was extended to examine the dependency of the interaction diagram in the load path. An interface friction coefficient of 1, rather than 5 was used. Figure 3-7 was developed for monotonic loading at a constant displacement angle. In these analyses, after displacing the pipe one pipe diameter at angles of either 45, 60, 75 or 90 degrees, the pipe was displaced a further pipe diameter in the axial loading direction. The pipe response is shown in Figure 3-12. The x-axis shows the first 100% in the prescribed load direction and the second 100% is under a

purely axial displacement. There is a reduction in the lateral capacity but an increase in the axial resistance during the second phase under purely axial loading.

The resulting failure points under axial loading are shown in
Figure 3-13. The original envelope comes from Figure 3-7 and was developed for a higher interface friction coefficient of 5. The points on the interaction diagram after stage 1 move under axial displacement as indicated by the arrows. These final positions lie close to the axial load limit imposed by the friction coefficient of unity that is around a normalized load of 1.25. The new points probably do not lie exactly on the limit line due to the complexity of the stress conditions around the pipe caused by the first stage of displacement. The original interaction envelope developed from monotonic loading is considered appropriate to capture the changes in failure loads caused by changes in load direction. No additional lateral resistance mobilized by the first displacement stage is retained during the second displacement stage.

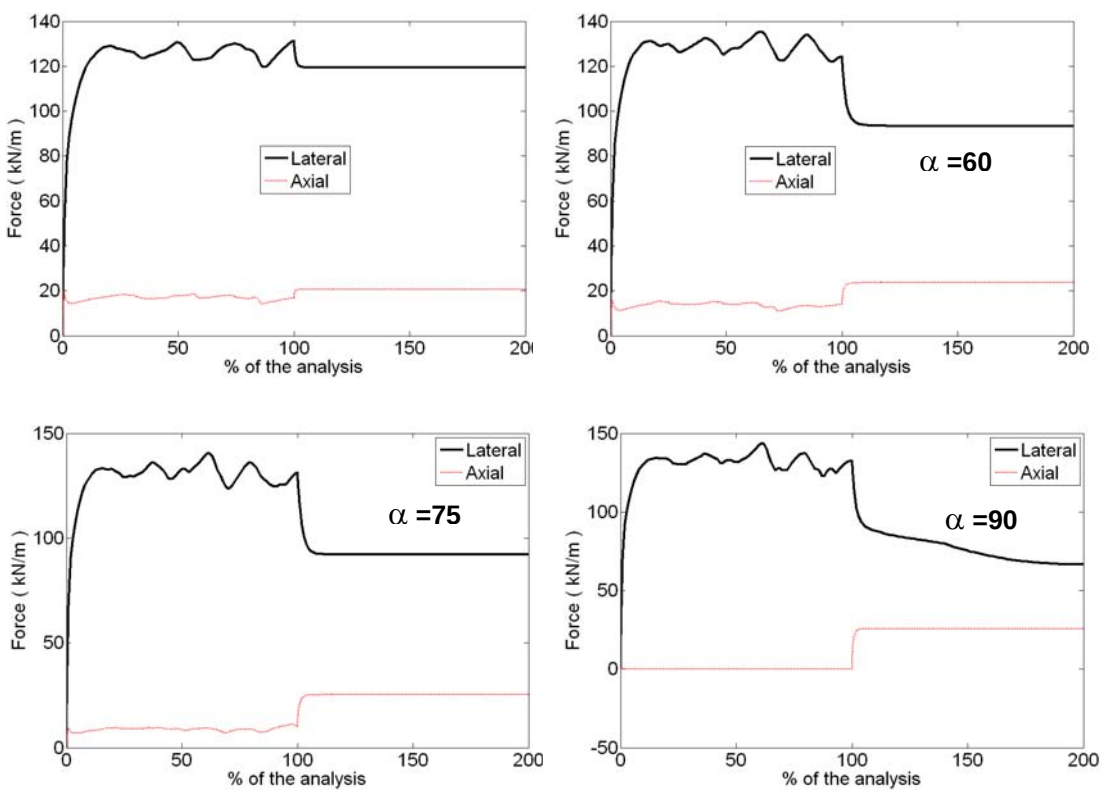

Figure 3-12 Pipe response with alternative loading paths in clay for H/D =2.5

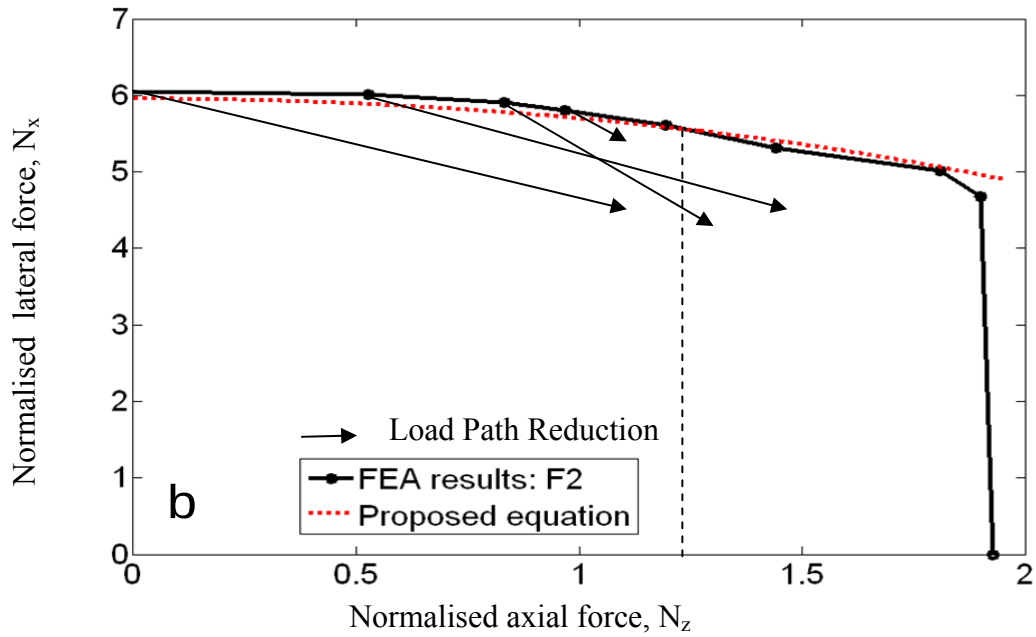

Figure 3-13 Interaction diagram considering loading paths in clay for H/D =2.5

4 MODELLING OBLIQUE PIPE SOIL INTERACTION IN SAND

4.1 Introduction

The finite element methodology presented in section 1 was also used to consider oblique pipe soil interaction in sand. Two sand densities were considered to consider both 'loose' and 'dense' sand behaviour. These analyses were first performed for a single pipe buried in sand with a diameter of 0.328m and a burial depth of 0.936m as illustrated in Figure 4-1.

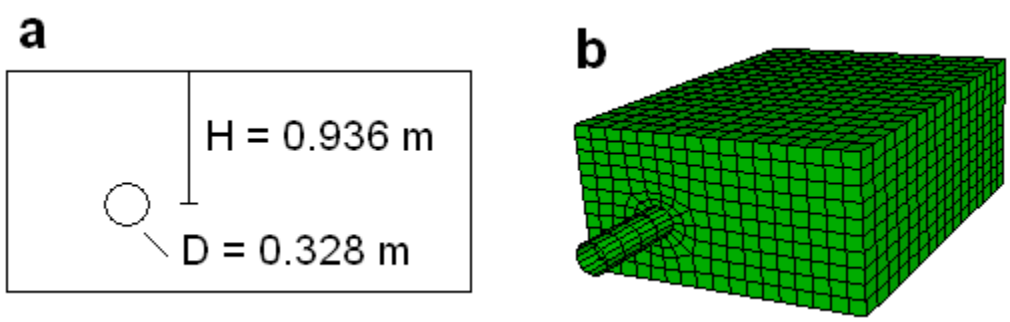

Figure 4-1 Layout of the buried pipe in sand, and FE model.

4.2 Soil Properties And Applied Loads

The constitutive model is the Mohr-Coulomb model implemented in ABAQUS/STANDARD. The assumed constitutive parameters are listed in Table 4-1, where E = sand modulus of elasticity, ν = Poisson's ratio, ϕ = soil friction angle, c = soil cohesion, ψ = dilation angle, f = coefficient of the pipe-soil interface friction, and γ = specific weight. Non-zero soil cohesion, c is required to prevent numerical instability. The sand modulus of elasticity depends upon the level of confining pressure (i.e., effective mean normal stress); a constant E value was used in this phase of the study.

Table 4-1 Sand constitutive parameters

Sand	E (MPa)	ν	ϕ	c (kPa)	ψ	f	γ (kN/m^3)
Dense	8	0.4	46°	2	10°	0.5	17.2
Loose	3	0.3	33°	2	0	0.38	15.2

The loading comprises two steps: (1) an oblique pipe movement equal to 25% of the pipe diameter (0 to 100% of analysis) followed by (2) an axial pipe movement up to 100% of its diameter (100% to 200% of analysis).

4.3 Numerical Simulation Results

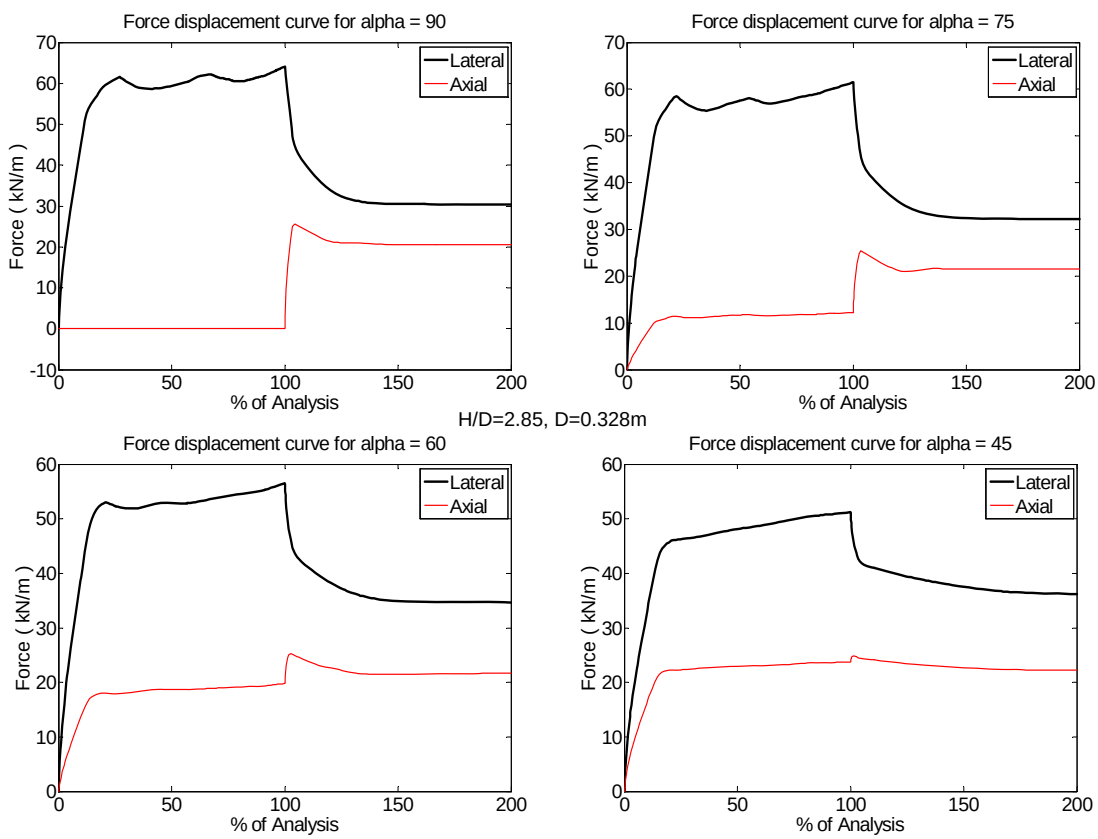

Figure 4-2 Pipe response in dense sand subjected to two-step loading

Figure 4-2 shows the force-displacement curves obtained for the pipe buried in dense sand subjected to the load case described in the previous section for different oblique angles of 45, 60, 75 and 90°. For these high α values, the full axial soil resistance is not mobilized during the first step of primarily lateral loading. The ratio of axial force to lateral force under oblique loading is less than 0.5, Figure 4-3a. This is less than the interface friction coefficient of 0.5, Table 4-1. Shear failure is therefore occurring through the soil mass, rather than along the pipe soil interface.

During the early stages of step 2, the axial force increases (accompanied by a decrease in the lateral force) until the full interface friction is mobilized. The ratio of the axial force

to lateral force is about 0.52 in dense sand, Figure 4-3b. This is slightly greater than the assumed interface friction coefficient, as the vertical forces acting on the pipe are not included in assessing the force ratio.

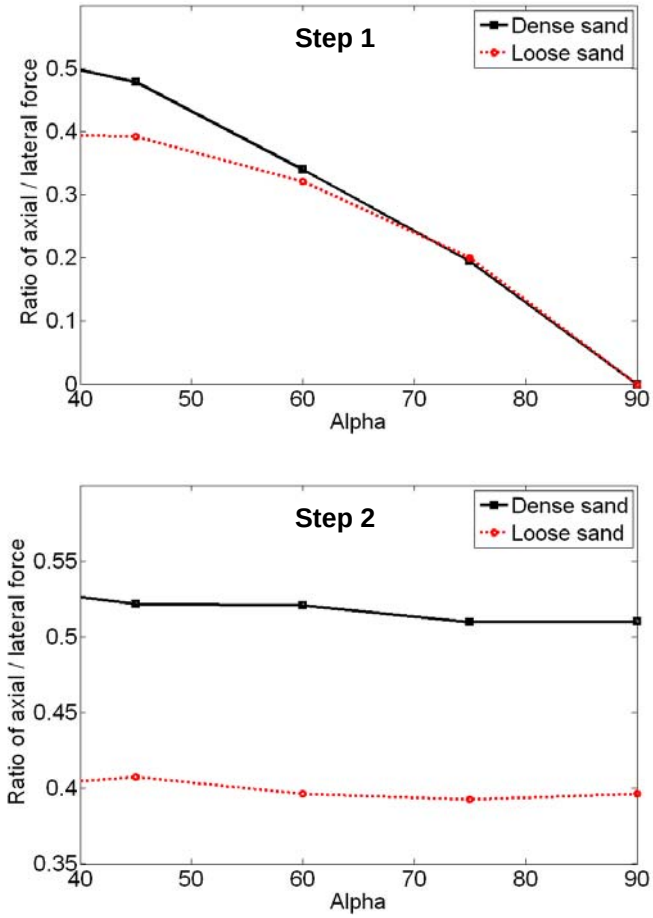

Figure 4-3 Predicted force ratios during loading steps 1 and 2

Numerical simulations of the pipe soil interaction in loose sand (Figure 4-4) resulted in similar observations: The ratio of the axial to lateral force is less than 0.4 during the first step of analysis, Figure 4-3a. The ratio decreases with increases in the oblique angle and is zero at $\alpha = 90$. During the second analysis step, the computed force ratio is reasonably constant around 0.40. Again this is greater than the friction coefficient as the vertical normal forces acting on the pipe are not considered.

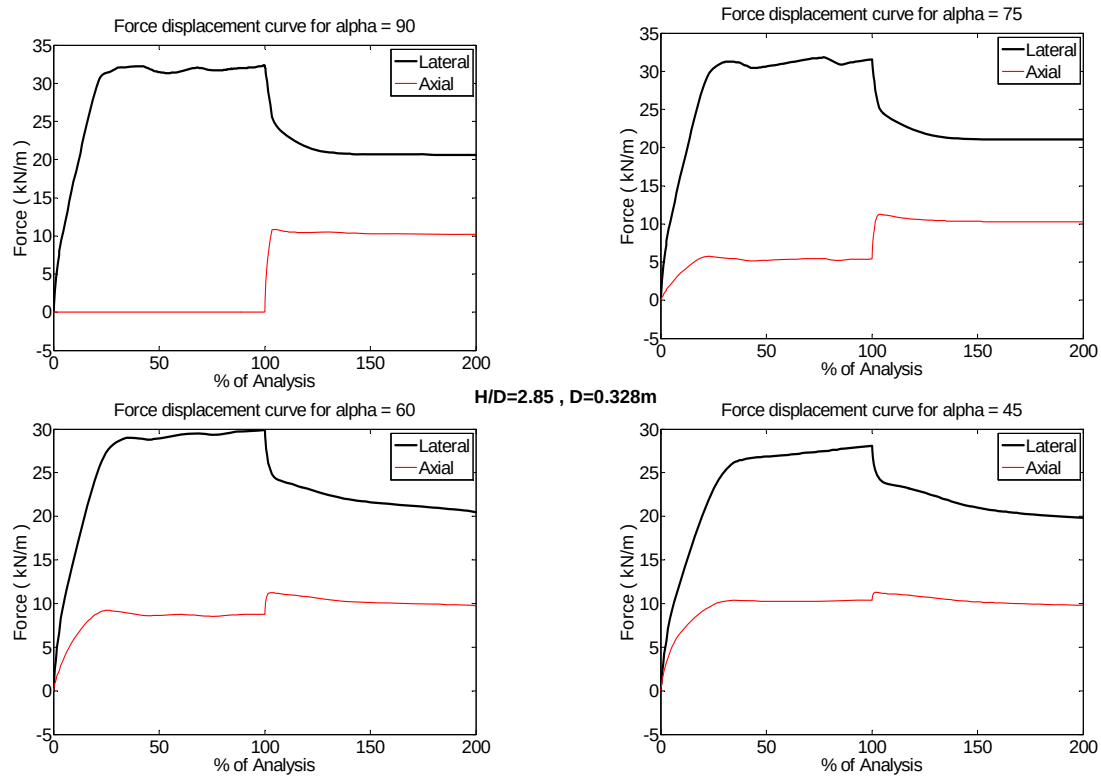

Figure 4-4 Pipe response in loose sand subjected to two-step loading.

Analyses were also conducted for displacement angles of 0, 5, 15 and 30 degrees. Figure 4-5 shows the predicted axial soil resistance for purely axial pipe movement in both loose and dense sands. In the case of dense sand, the predicted axial soil resistance occurs at 3% of the analysis step 1 (i.e., 0.75% of the pipe diameter) with a magnitude equal to 7.9 kN/m. For loose sand, the maximum soil resistance due to purely axial pipe movement of 1% of the pipe diameter with a magnitude of 5 kN/m. These magnitudes are consistent with the axial resistance values for sand calculated from the initial stress conditions using Table 2-1.

Figure 4-6 shows the predicted dimensionless axial and lateral soil resistances for different oblique angles both in dense and loose sands as interaction diagrams. The resistances are normalized by the product of bulk density, burial depth and pipe diameter. The predicted dimensionless axial soil resistances for dense and loose sands indicate a rapid increase from zero to $\alpha = 5^{o}$. For the range of α between 5° and 45° the computed axial soil resistances do not change significantly; however, for higher values of α the predicted forces tend to decrease significantly with increase in the oblique angle.

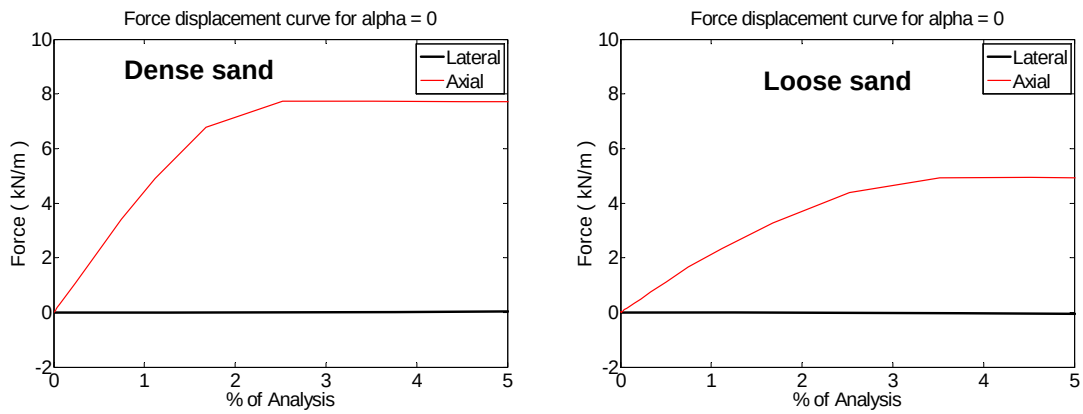

Figure 4-5 Predicted pipe response to axial movement in loose and dense sands.

The predicted dimensionless lateral forces for both dense and loose sands increase due to increase in the oblique angle. This is significantly pronounced for a range of $\alpha \leq 5^o$.

Figure 4-6c shows the predicted interaction diagrams for loose and dense sands. The predicted interaction curves are linear for small oblique angle (up to about 5°) due to frictional failure along the pipe interface. A nonlinear response is seen for higher values α as the failure mechanism changes to shear failure through the soil mass.

For pure lateral loading, Guo and Stoller (2005) propose the lateral interaction factor N_h of the form:

$N_h = k_1 (p_{ref}/\gamma H) + k_2$, where $k_1=11.1\ (H/D)^{0.55}$ and $k_2=6.5(H/D)^{0.35}$ (4-1)

The form of the equation accounts for geometric and soil parameter effects, and p_{ref} is a reference pressure of 1 Pa. The k_1 and k_2 expressions are relevant for a soil with 2kPa cohesion, 33 degree critical state friction with a further 10 degree of dilation. This sand condition lies between the loose and dense sand conditions assumed in these analyses. For H/D =2, N_h is calculated as 9.2 which lies between the 7.0 and 11.8 values for loose and dense sands respectively,
Figure 4-6c.

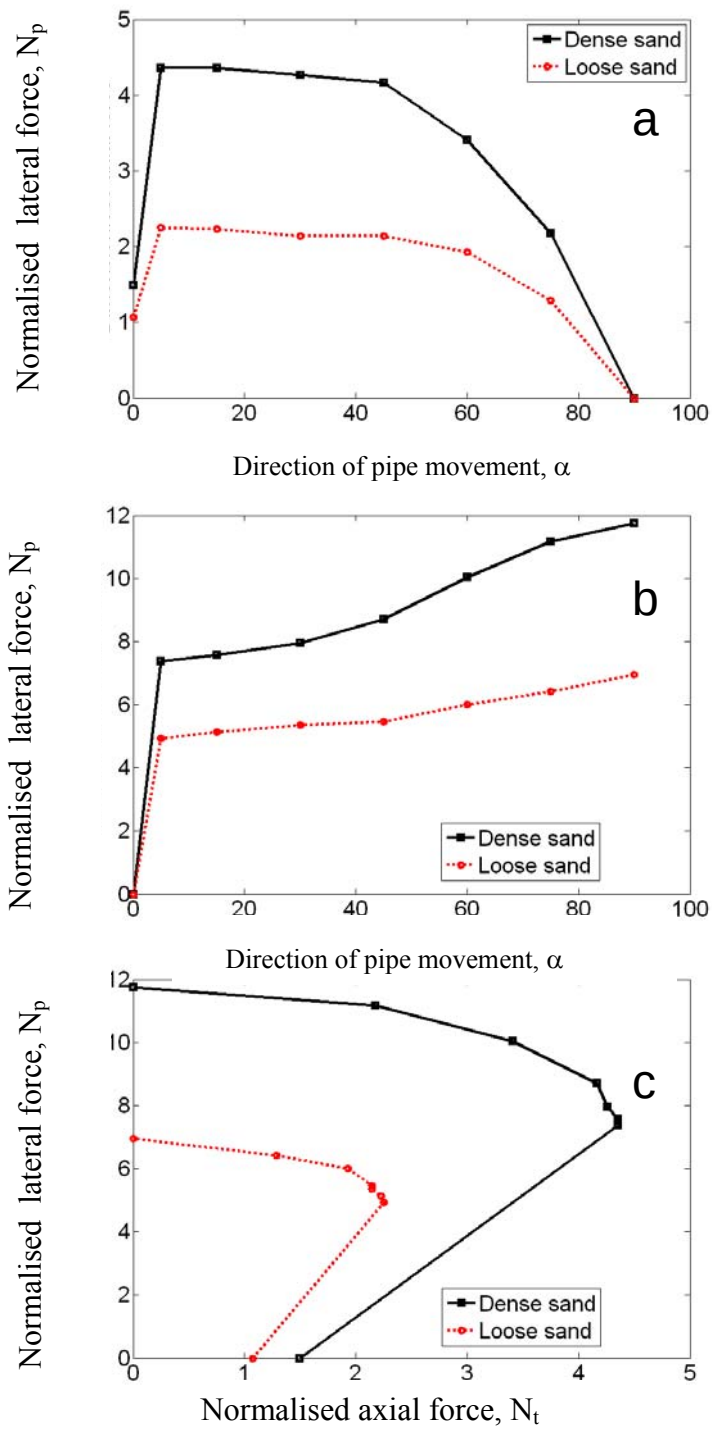

Figure 4-6 Predicted normalized pipe resistance in dense and loose sands

4.4 Burial Depth And Other Sensitivities

The analyses were extended to include burial depths H/D = 1.5 and H/D = 2.5, Figure 4-7 and Figure 4-8. The pipe diameter was increased to D = 0.508m, and a second cohesive intercept, c' of 16 kPa was considered. This geometry and the oblique angles of α = 0, 10°, 60°, and 90° were the same as used in the centrifuge tests on buried pipes in dense sand, section 5.5.

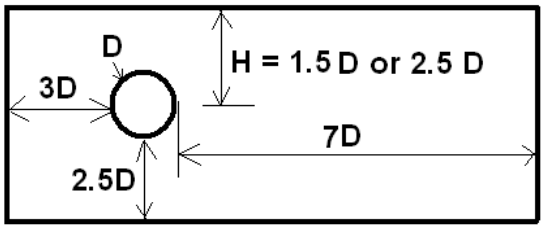

Figure 4-7 Layout of the buried pipes in sand

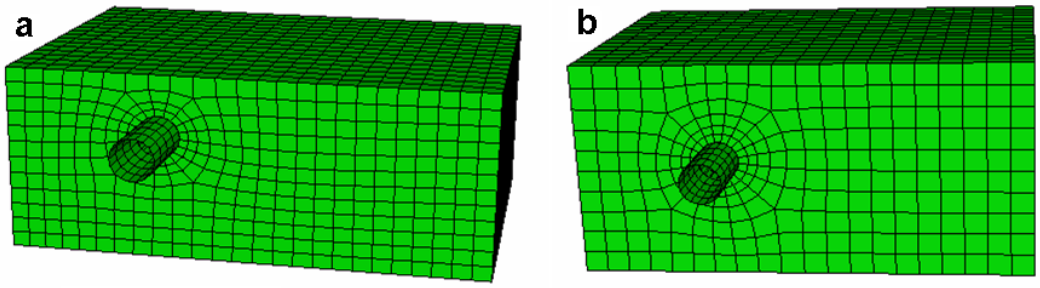

Figure 4-8 Finite element models: a) H/D = 1.5 and b) H/D=2.5

4.4.1 Loading

This loading only included two steps: (1) a geostatic step to obtain the initial stress field within the soil medium and on the buried pipes followed by (2) an oblique pipe movement up to 100% of its diameter. Subsequent axial displacement was not considered. The numerical results are presented only for the second load step, i.e., the oblique pipe movement.

4.4.2 Buried pipe in dense sand, H/D =1.5

The numerical results are significantly affected by the value of soil cohesion, Figure 4-9 and Figure 4-10. For instance, for α=90° the lateral force is almost doubled when cohesion changes from 2kPa to 16kPa. This trend is seen for all cases except for α=0 (purely axial case), where the frictional interface behavior prevails.

4.4.3 Buried pipe in dense sand, H/D =2.5

The numerical results for deeper burial are again significantly affected by the value of soil cohesion, Figure 4-11 and Figure-4-12; however, the influence of this parameter in this case is not as significant as that in case of H/D = 1.5. For instance, for $\alpha = 90^{o}$ the lateral force increases about 50% by changing the cohesion value. The reduced effect of cohesion is due to the increased contribution of the frictional strength component under the increased self weight stresses.

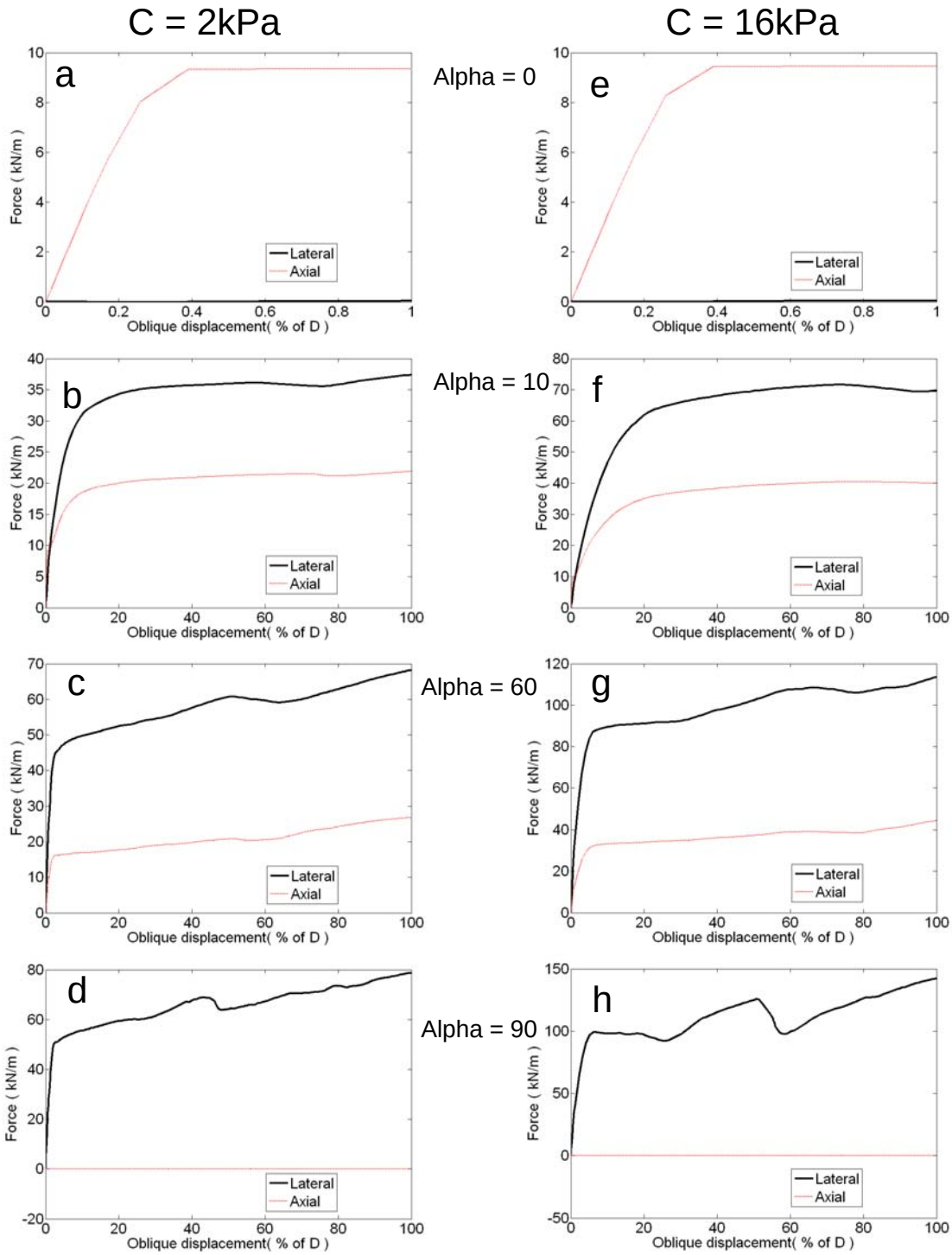

Figure 4-9 Lateral and axial pipe response in case of H/D =1.5

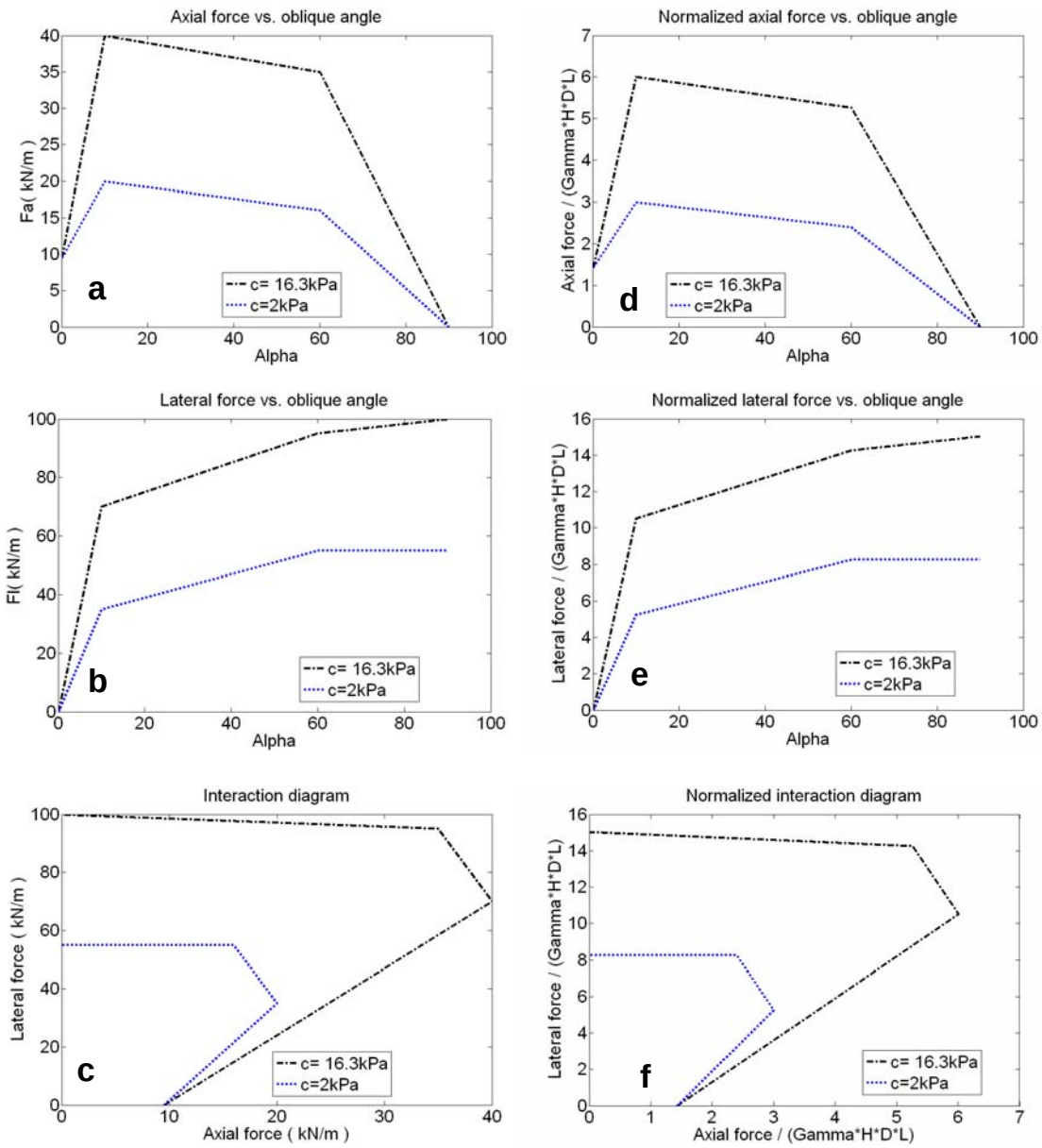

Figure 4-10 Interaction diagrams for H/D =1.5 in cohesive sand

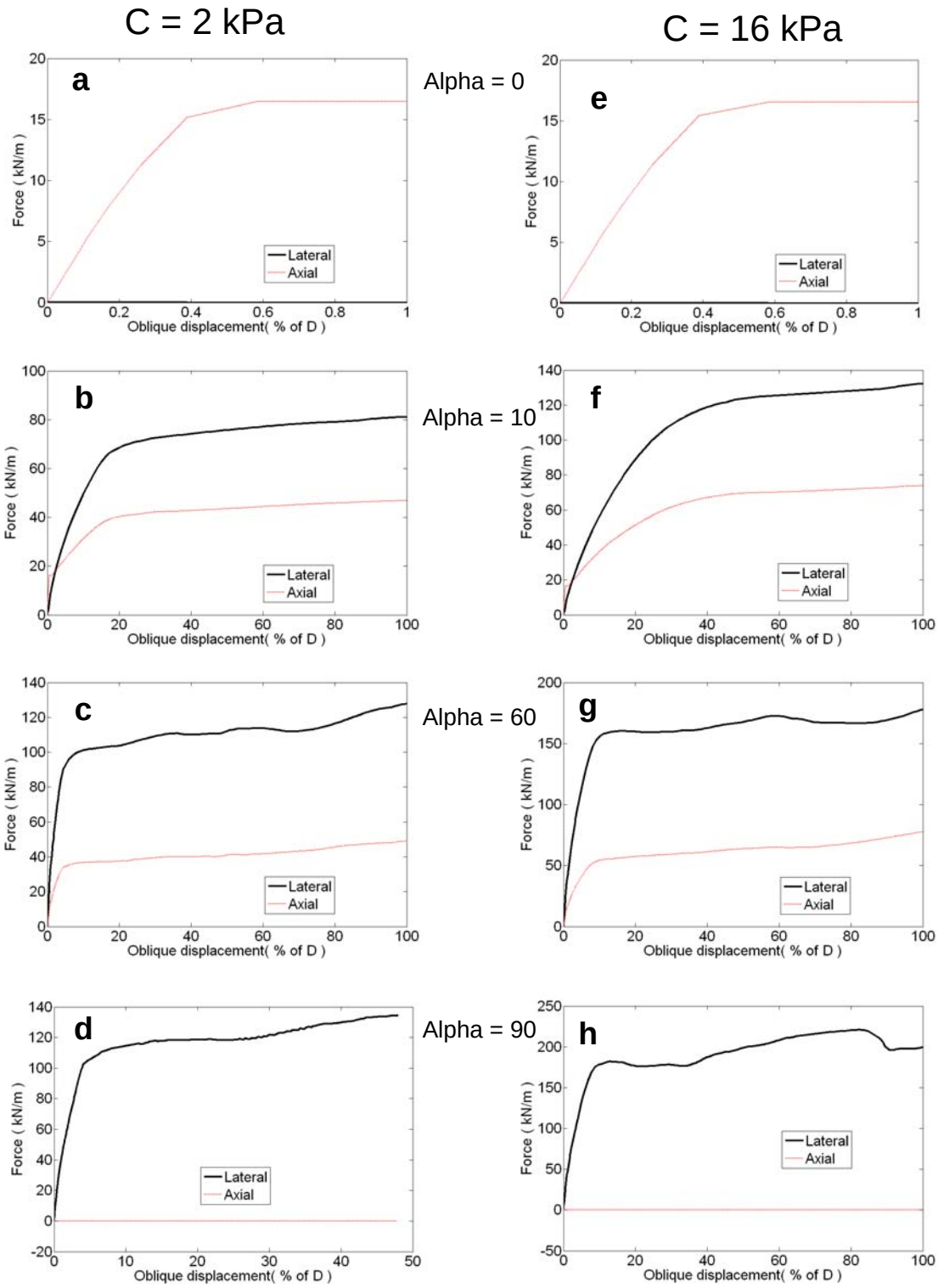

Figure 4-11 Lateral and axial pipe response in case of H/D =2.5

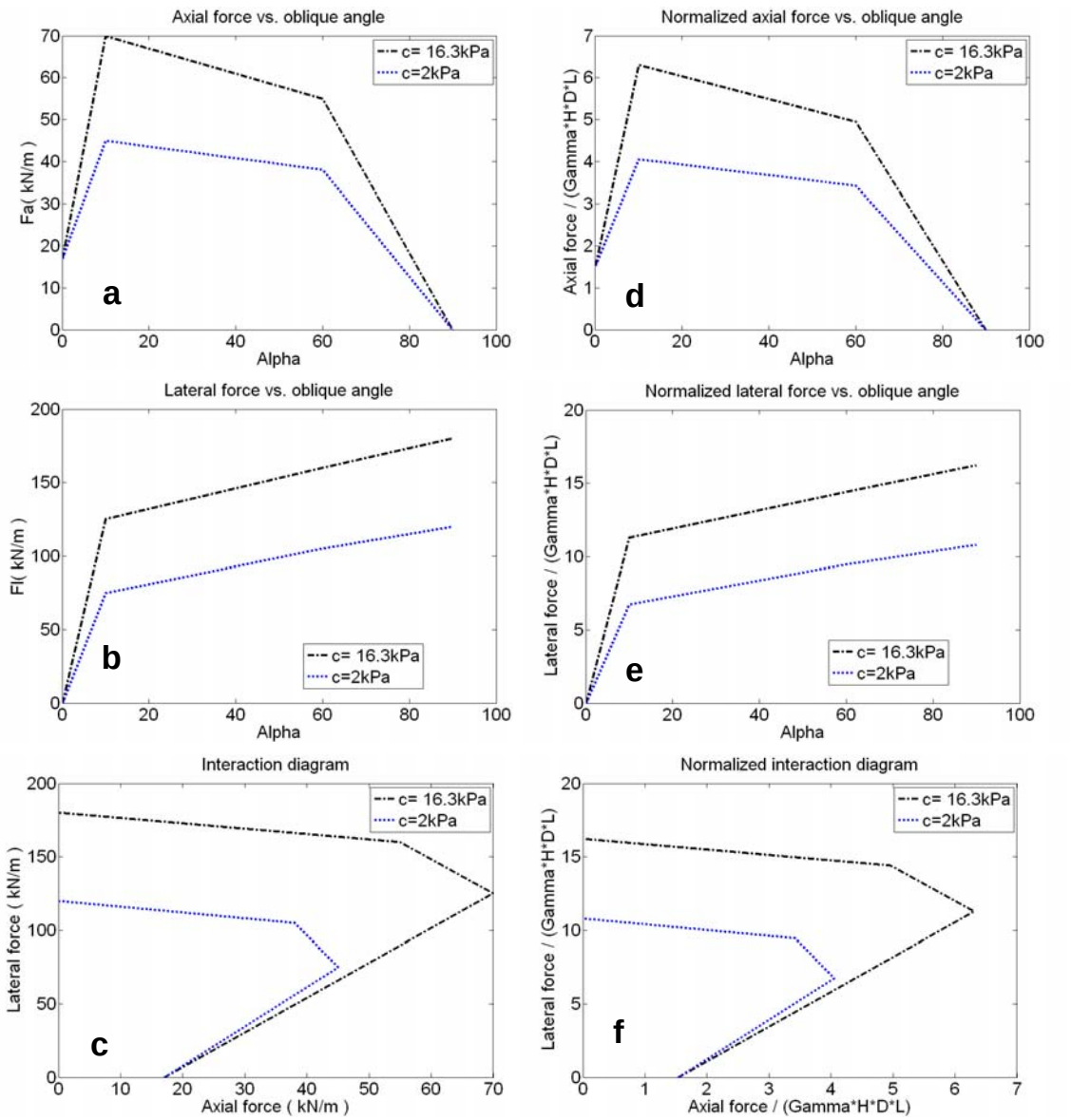

Figure-4-12 Interaction diagrams for H/D =2.5 in sand

4.5 Effects Of Soil Hardening On Oblique Pipe Soil Interaction

The previous analyses in this section have focused on the prediction of failure loads, using linear elastic, perfectly plastic material models. Such models can predict these loads well, but the deformational response of real physical systems, such as the centrifuge model tests in the next section, may not be so well predicted,. The deformational response prediction can be improved by variation of the material strength and stiffness parameters as the system is strained. In these next 2 sections the effects of soil hardening/softening and variation of stiffness parameters on the ultimate interaction forces due to oblique movement of pipes buried in sand are studied.

The numerical results are compared with the current guidelines and the interaction equation proposed by C-CORE (2003). A subroutine and guidelines to implement the presented method in the latest version of ABAQUS/STANDARD are presented.

The layout and the finite element model of the buried pipeline studied here are shown in Figure 4-7. The pipe diameter (D) and the burial depth (H) are D = 0.508m and H = 1.5D.

4.5.1 Soil constitutive model

The constitutive model is the Mohr-Coulomb model as presented in section 4.2. The ABAQUS software allows changes in friction angle, dilation angle and cohesion as functions of field variables. The plastic strain level is considered as a field variable to account for changes in the material yield conditions during plastic straining (hardening law). The sand shear strength and dilation parameters are updated at the end of each time step based on the equivalent plastic strain magnitude computed at the same instant. A similar methodology was used in C-CORE (2003).

The use of this methodology requires interpretation of laboratory test data to infer variations of shear strength parameters as functions of plastic strain magnitude from the experimental results. The experimental data used (i.e. dependence of friction angle on the plastic strain level) have been obtained from previous studies for others at C-CORE.

The constitutive parameters (soil and interface properties) are developed from those defined in Table 4-1. In addition, ϕ_{cv} = constant volume friction angle, and ε^p = plastic strain magnitude. The mobilized friction angle at any time is a function of plastic strain magnitude (Function f_1), Table 4-2,. The initial estimation for the values of dilation

angle, ψ , can be obtained from the Rowe's stress dilatancy theory as a function of ϕ and ϕ_{cv} (Function f_2) expressed by:

$$\sin\psi = \frac{\sin\phi - \sin\phi_{cv}}{1 - \sin\phi \sin\phi_{cv}} \tag{4.1}$$

Table 4-2 Dense soil and interface constitutive parameters

Soil Model	Soil type	E (MPa)	ν	ϕ	c (kPa)	ψ	f	γ (kN/m^3)
Mohr-Coulomb	Dense sand	8	0.4	$f_1(\varepsilon^p)$	5	$f_2(\phi, \phi_{cv})$	0.5	17.2

The functions f_1 and f_2 are defined by piece wise linear fits to the data tables presented in Figure 9-1 as detailed in Appendix A, section 9.1. The constant volume friction angle ϕ_{cv} is 35.3 degrees, with a maximum angle of 43.7 degrees associated with a dilation angle, ψ of 10.6 degrees.

4.5.2 Numerical simulations

The oblique angles considered here are 0 (purely axial), 5°, 10°, 20°, 30°, 45°, 60°, 75°, and 90° (purely lateral). The force-displacement curves for the different oblique load angles are shown in Figure 4-13 to Figure 4-15. Post peak reductions in load are observed in all cases except for axial loading, followed by a load regain as material is displaced upwards in front of the displaced pipe. For each case the peak lateral and axial interaction forces (e.g. Figure 4-13c for $\alpha = 10^o$) occur at the same displacement level. This level decreases from 0.3D to about 0.05D as the load angles increases from 5 to 90 degrees.

The peak loads are quite close to those predicted in section 4.4.2 for similar geometric and material conditions (cohesion of 2kPa), Figure 4-9 under the same load angle. The dimensionless interaction diagrams of Figure 4-10f for 2kPa and Figure 4-16 are very similar.

Figure 4-16 also compares the interaction diagram with C-CORE (2003) recommendations for purely axial and lateral load cases and equation 3-1 (solid curve in Figure 4-16). This equation, section 3.4.2 was originally developed by C-CORE (2003) for clay interaction.

The straight inclined line and equation 3-1, define reasonable bounds for the interaction diagram. These lines are constructed according to the coordinates shown in Figure 4-16 (where f is the coefficient of the pipe-soil interface friction).

The axial and lateral interaction force guidelines presented in CORE (2003) with and without considering cohesion are plotted in Figure 4-16. The lateral force guides use Honegger and Nyman (2001) to account for the contributions of both cohesion and friction angle as presented in Table 2-1 and section 2.2 However, the lateral frictional component is assessed using Trautmann and O'Rourke (1983) factors. The finite element simulation lateral forces are reasonably close to the guideline. For axial loading, the simulation is closest to the guideline values for no cohesion, as the simulation limited the shear stress ratio at the pipe interface.

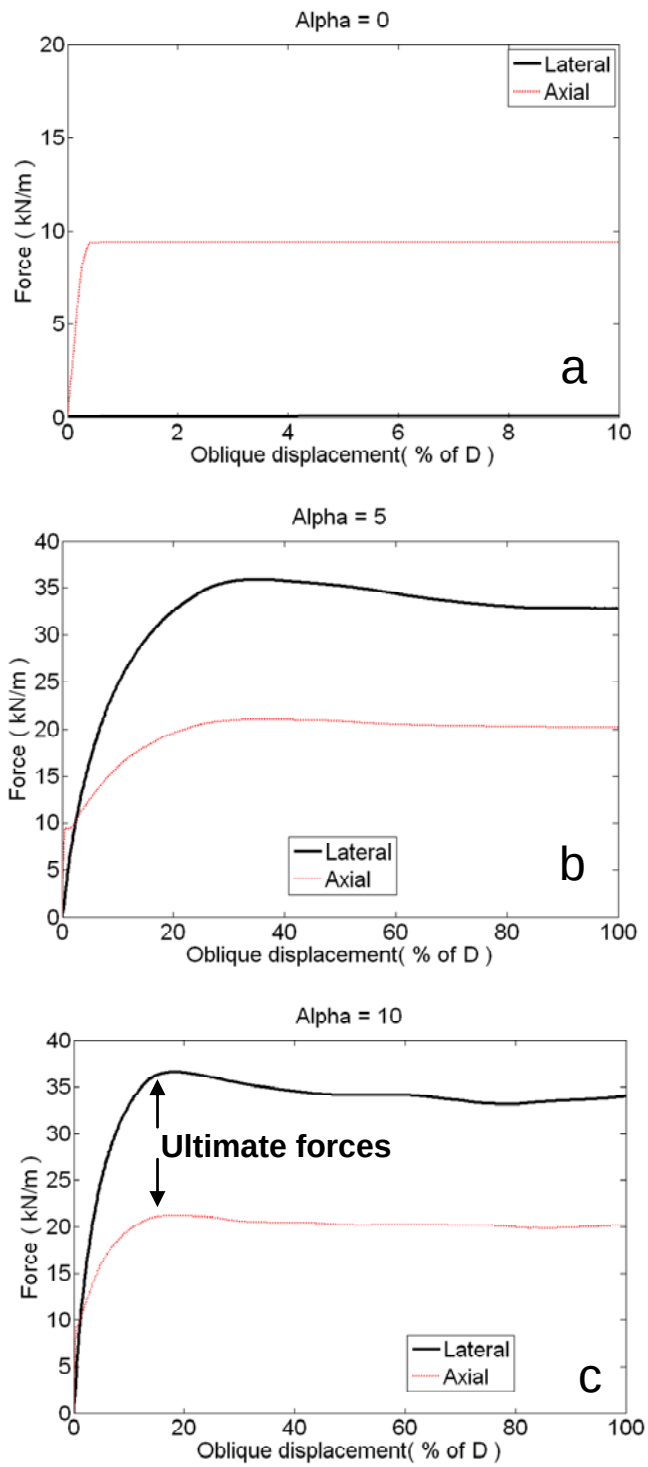

Figure 4-13 Predicted force-displacement curves for shallow oblique angles

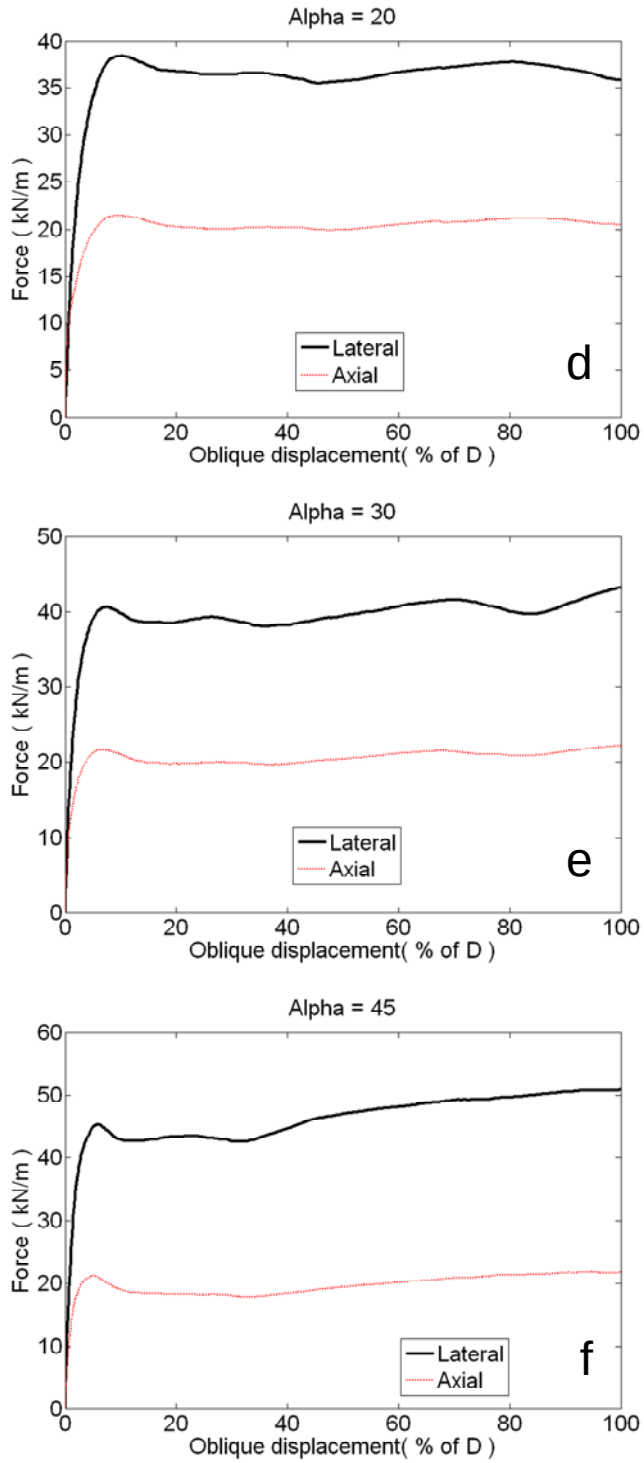

Figure 4-14 Predicted force-displacement curves for intermediate oblique angles

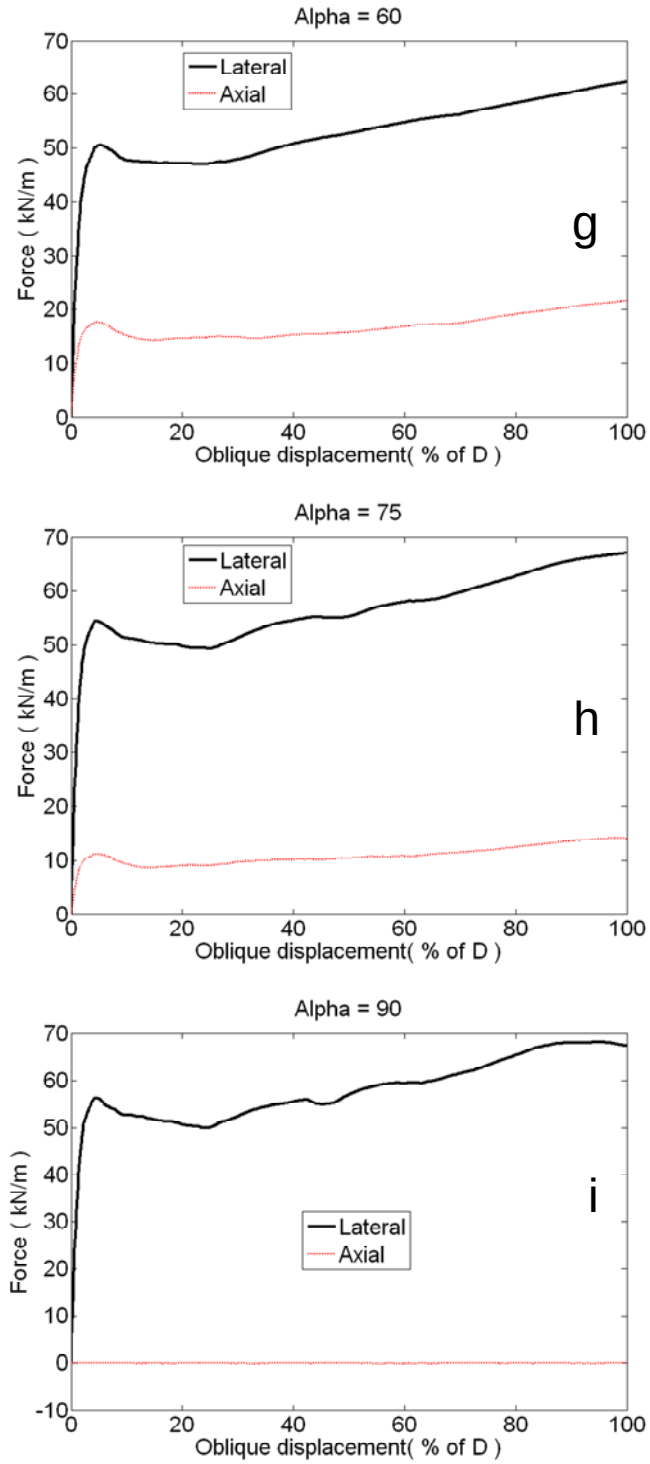

Figure 4-15 Predicted force-displacement curves for large oblique angles

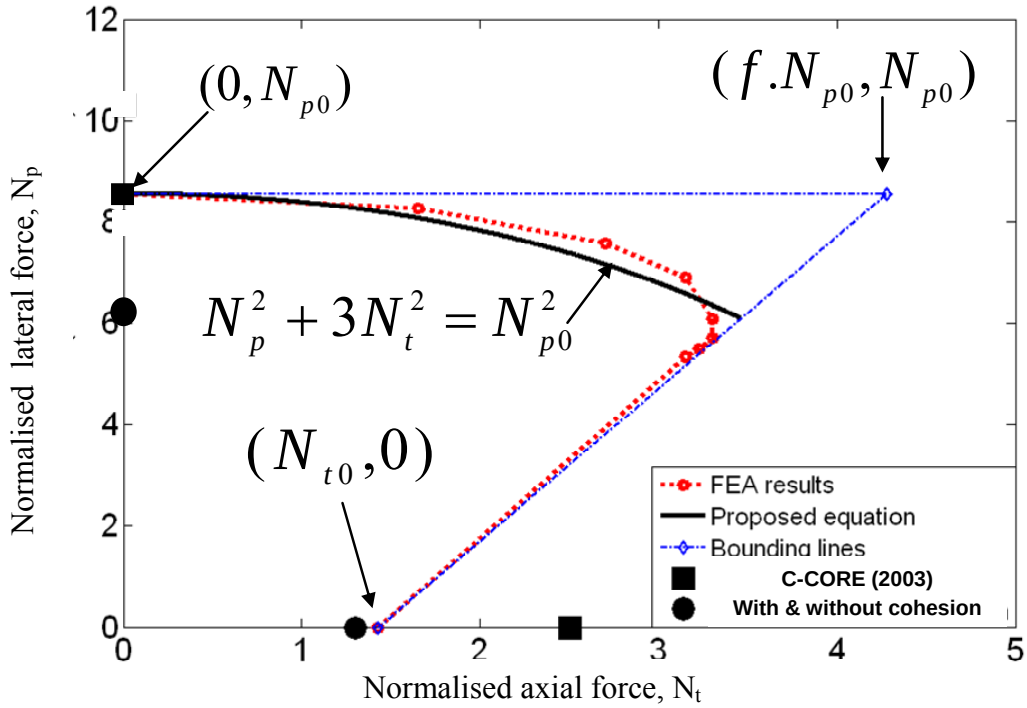

Figure 4-16 Interaction diagram comparison for dense sand

4.6 Effects Of Elastic Stiffness On Oblique Pipe Soil Interaction

The elastic modulus of sand is dependent upon the level of confining stress. This section demonstrates how it can be updated accordingly in the analyses.

The geometry is shown in Figure 4-7 with D = 0.508m and H/D = 2.5. The pipe is moved laterally. The Mohr-Coulomb constitutive model, section 4.5.1 uses updated shear strength parameters (cohesion and friction angle), dilation angle and soil modulus of elasticity. Shear strength parameters and dilation angle are updated based on the equivalent plastic strain magnitude calculated at the end of each time step, section 4.5.1. The sand elastic modulus, *E*, is updated to simulate its dependence on the confining stress level, *p*, as expressed by:

$$E = E_0 \left(\frac{p}{p_0}\right)^n \qquad (4\text{-}2)$$

In Eq. (4-2), E_0 is the sand shear modulus at a reference confining pressure of p_0, and *n* is a power exponent. For most sands a reasonable value of *n* is 0.5. The reference confining

pressure is usually considered equal to the atmospheric pressure (i.e. p_0 = 100kPa) and E_0 is estimated from the laboratory soil tests or available correlations and charts found in the literature at a certain strain level. In this study E_0 is 24.5MPa. The value considered here is a typical value for pipe soil interaction and was selected for demonstration purposes. This modulus is also dependant on the strain magnitude, for example much higher values are required to simulate very low strain phenomena such as acoustic wave propagation.

The subroutine USDFLD and the material formulations used for this analysis are presented in Appendix A, section 9.2.

The sand material exhibits significant softening behavior as expected, Figure 4-17. The computed peak load (160kN/m at a lateral pipe movement of about 20% of its diameter) reaches a steady state value of about 100kN/m at a lateral pipe movement of about 80% of its diameter. This curve can be compared with Figure 4-11h for similar geometric and peak strength conditions. The peak load predictions are similar. This load for constant parameters is mobilized at a smaller displacement of about 0.1D.

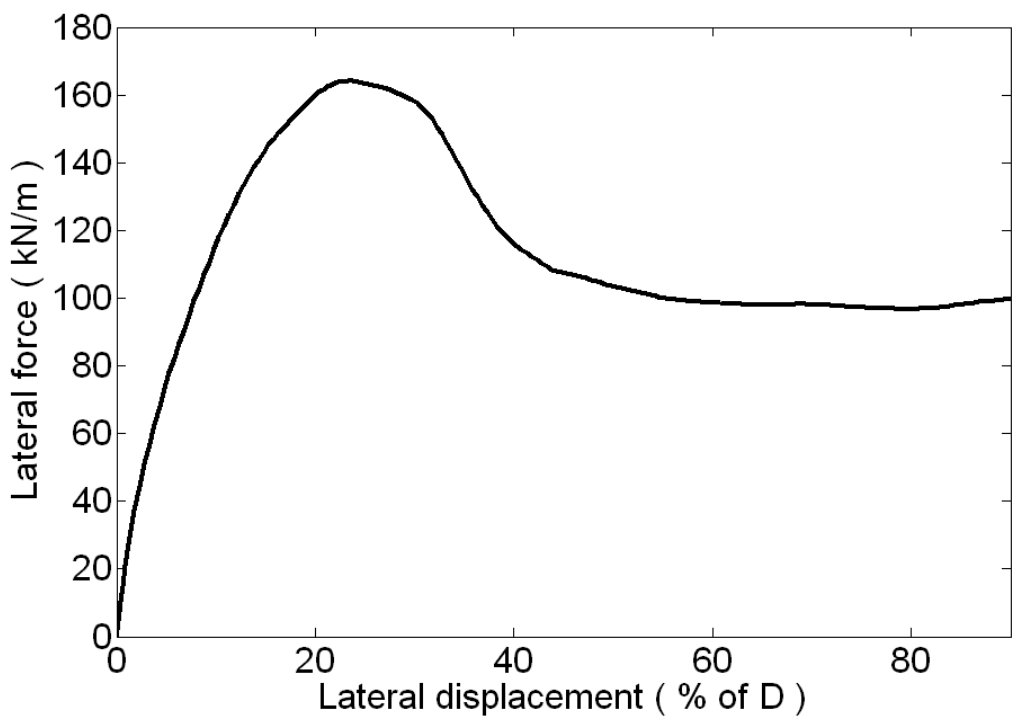

Figure 4-17 Predicted force-displacement curve with elastic stiffness variation.

5 CENTRIFUGE MODELLING

5.1 Introduction

The physical modelling program comprised centrifuge tests of obliquely loading of pipeline sections in a horizontal plane in cohesive and granular soil. The axial and lateral load components acting on each section were assessed for four different load angles. These model tests complemented the numerical analyses presented in sections 3 and 4.

Centrifuge modelling has been shown to be a useful tool when modelling gravity dependent phenomena (e.g. Schofield, 1980; Murff, 1996). Centrifugal acceleration is used to simulate increased gravity and allows for correspondence of stress fields between model and full-scale, permitting accurate modelling of geotechnical and other gravity dependent phenomena. Such modelling increases general understanding, and permits calibration and verification of numerical and theoretical models of full-scale situations.

5.2 Summary Program

A total of 8 tests were performed in two test beds: one of saturated silty clay and one of dry fine sand. Table 5-1 summarizes all test conditions. The physical model tests were conducted in the C-CORE centrifuge. All tests were done under an acceleration of 12.3g. The pipes were pulled at a displacement rate of 0.4 mm/s. This rate was sufficiently fast for undrained lateral loading in the cohesive soil, Phillips et (2004).

Table 5-1 Summary of experimental tests

Test	Soil	Load Direction	Date	Cover Depth (mm)	Relative density / Shear Strength (kPa)	Cover Depth (D)
1	Sand	Axial	10 July 07	58.5	0.4	1.43
2		Lateral	13 July 07	55.5	0.4	1.35
3		60 degree	18 July 07	53.5	0.4	1.30
4		20 degree	24 July 07	56.5	0.4	1.38
5	Clay	Lateral	25 Sep 07	61.8	25	1.50
6		60 degree	26 Sep 07	61.9	30	1.50
7		20 degree	27 Sep 07	61.7	30	1.50
8		Axial	28 Sep 07	61.8	30	1.50

5.3 Experimental Apparatus

5.3.1 Pipe sections and load cells

A 20” diameter steel pipe was modeled at 1/12.32 scale using a 1 5/8” C-1026 cold drawn seamless tube. The pipe model was 41mm in diameter (D) by 328mm long, with a wall thickness of 6.35mm. The pipe was translated horizontally by an actuator connected, through a load cell, to each end cap.

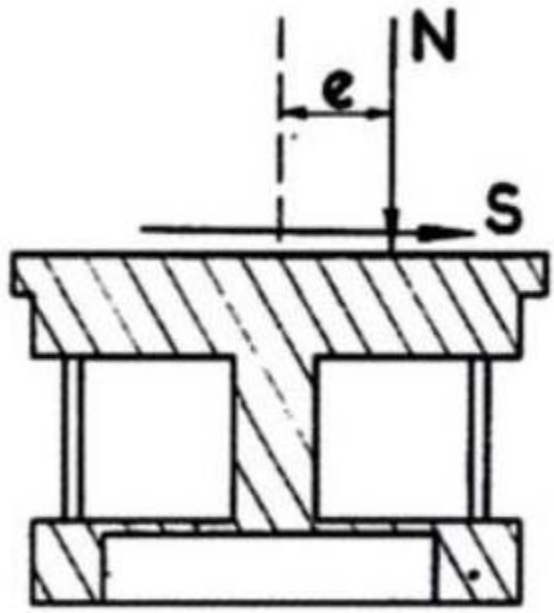

Figure 5-1 Pipe load cell principle, after Stroud (1971)

The pipe load cells measured one horizontal load component, the applied axial load and the point of load application. The first load cells were built and tested after the design of Hsu et al (2001), but this design was not appropriate for the applied load levels and the smaller pipe diameter. The load cells were rebuilt according to the design of Stroud (1971), Figure 5-1. Two sets of strain gauged thin webs measure these loads principally in compression. The axial load, N is measured in the 2 vertical webs shown, and the lateral load, S in the horizontal webs. There is cross sensitivity between the 2 sets of webs. The load cells were therefore calibrated under 3 different combinations of dead weight lateral and axial load applied at varying load eccentricities to assess the calibration matrix, Figure 5-2. The lateral load is applied through the steel wire. The axial load is applied vertically through a loading yoke (off the load cell in the back of photo) through the ball bearing sat on the load cell top cap. The load cell was covered by a sleeve for pipe testing.

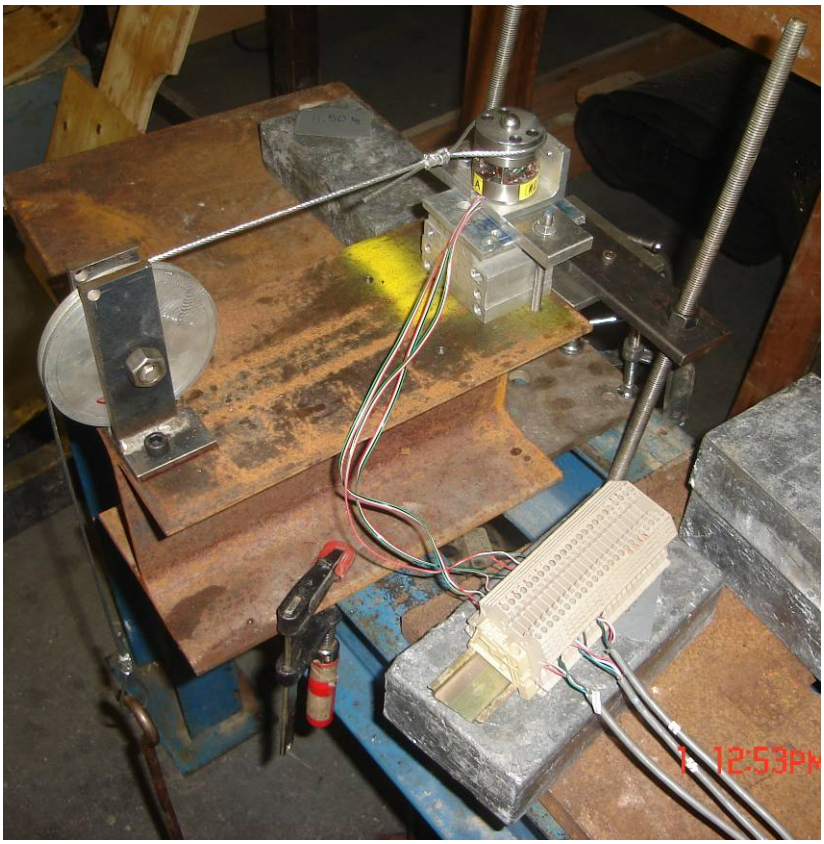

Figure 5-2 Pipe load cell dead weight calibration

5.3.2 Test Package & Actuator

A new servo controlled load actuator was built to translate each buried pipe section through the soil bed. The interfaces between the actuator and the buried pipe and the strongbox are depicted in Figure 5-3, with the pipe connection details in Figure 5-4.

The pipe was located in the soil bed by an actuator consisting of: a guided ball screw, a carriage with two ball races, two stanchions and two load cells. The load cells are bolted to the two stanchion bases, the pipe is pinned between the load cells by the two ball bearings. An aluminum dog bone was used to prevent the stanchions from rotating; keyways were later grooved into the stanchions to prevent rotation. The stanchions were located and guided by two linear ball races, which were connected to the actuator carriage through a pivot assembly. The pivot was locked in the required orientation to the actuator for each test. The races allowed for vertical movement of the pipe, although little movement was measured during the tests. The horizontal actuator was held in place by

two aluminum support I-beams bolted to the rectangular strong box containing the soil and the pipe. Each testbed contained 4 buried pipe sections.

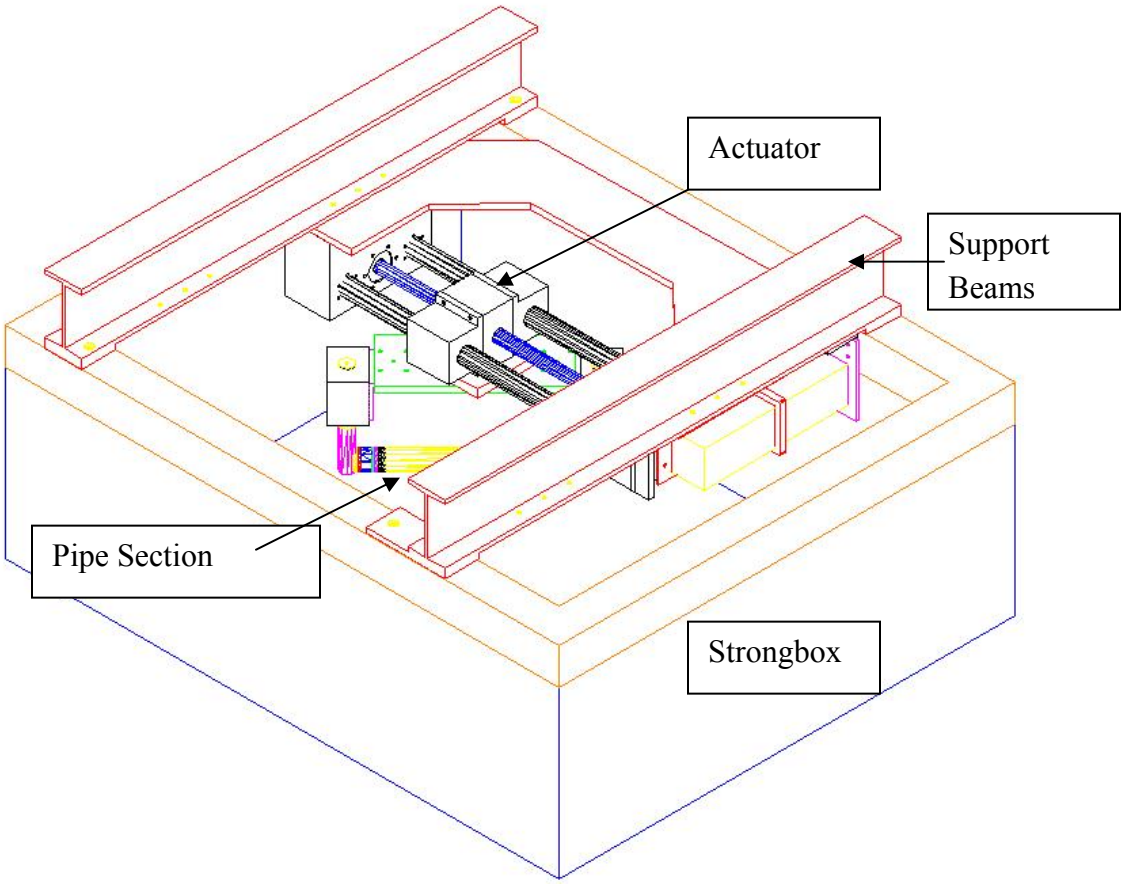

Figure 5-3 Pipe loading actuator overview

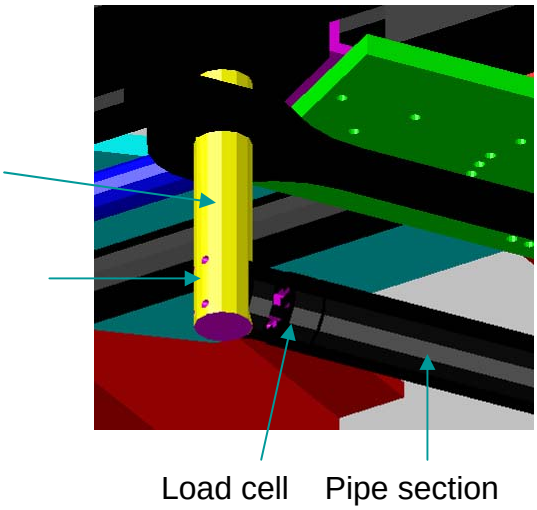

Figure 5-4 Pipe end connection details

5.4 Soil Preparation and Testing

5.4.1 Testbed preparation

The testbeds were comprised of either saturated silty clay or dry fine sand. Paulin (1998) discussed reasons for the selection of this silty clay mix. The sand was commercially available dry graded fine sand.

The silty clay testbed was a mixture of 50% Speswhite Kaolin clay and 50% Sil-Co-Sil silt. The soil was mixed from powder in a Bowers ribbon blade mixer at twice its liquid limit (70% water content) under vacuum. The soil was consolidated to a maximum vertical pressure of 450 kPa. The compression index and swell index was determined to be 0.161 and 0.027 respectively from observation of consolidation data. The resulting conditions gave a clay soil with approximate water content of 30%. The bulk unit weight of this soil was 18.9 kN/m^3.

Before each pipe clay test, the pipe was placed in a 1.5D wide vertical trench excavated in the testbed. A 25mm thick crushable foam pad was placed on the leading end cap of the stanchion to minimize end bearing stress influence on the measured pipe section response. The trench was backfilled with the excavated material which was tamped into position. For each test 1.5D (61.5mm) was the target cover depth; this measurement was followed to within half a millimetre. The clay surface was coated in Vaseline to prevent surface drying during centrifuge flight.

A set of vane shear test were conducted prior to excavating a trench in the clay, and an additional series of vane shear test were completed after each centrifuge test; the results of each test can be found below.

The sand was Alwhite medium-fine sand with a specific gravity of 2.66, a maximum void ratio of 0.89, and a minimum void ratio of 0.57. The grain size distribution curve of the sand is shown in Figure 5-5. The unit weight of the sand as placed was 14.8 kN/ m^3. Direct shear box tests around this density gave a critical state friction angle of 35 degree and a peak friction angle of 42 degrees.

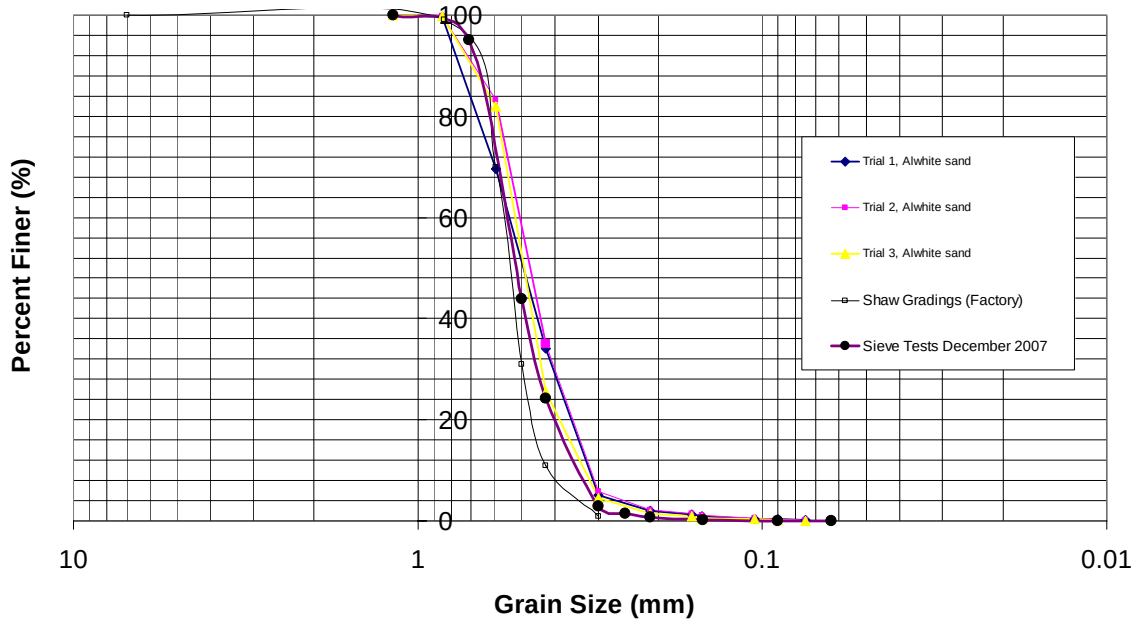

Figure 5-5 Sand grain size distribution

Sand was dry pluviated at the target relative density to form the bedding layer. The pipe was placed on the bed and soil pluviation was continued until the target cover was obtained. A flat surface was achieved by passing a vacuum over the top of sand at a constant elevation.

5.4.2 Instrumentation and measurement

The carriage (and pipe displacement) was measured using a non-contact laser displacement sensor with a range of 30 to 130mm. The pipe load components were recorded using 2 Stroud cells as described in section 5.3.1.

In the clay tests, pore pressure transducers were placed at depths throughout the bed to monitor clay consolidation. An LVDT displacement sensor was also placed on the soil surface of all tests to monitor surface settlement. The upward movement of pipe was also measured by two LVDT's that were connected to the ball races.

5.4.3 Test Procedure

The test procedure is briefly described in this section. The activities can be divided into four phases: (1) test bed preparation, (2) preparation of test package, (3) centrifuge test,

and (4) post-test activities. In-flight centrifuge activities included the re-consolidation of soil under self-weight and pipe displacement.

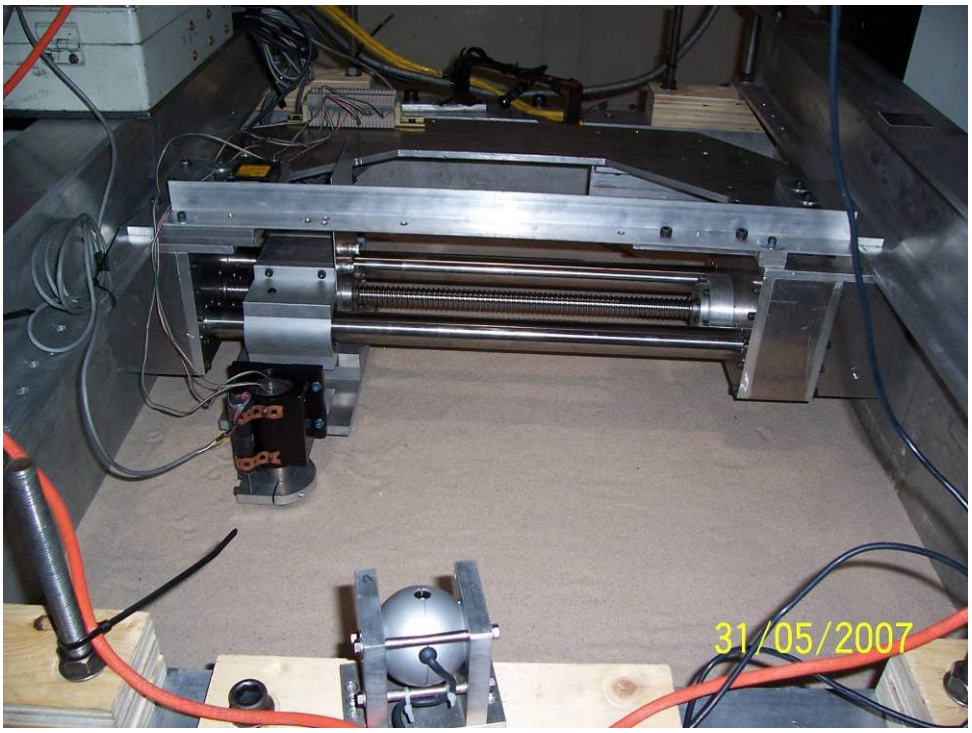

Figure 5-6 Pipe segment prior to lateral loading.

The test bed was prepared as described in section 5.4. The test package was then completed by placing the actuator on the strongbox, and connecting the buried pipe section to the actuator carriage, Figure 5-6. The instrumentation was connected to the signal conditioning system and a web camera mounted to observe the actuator movement. The completed test package was placed in the centrifuge.

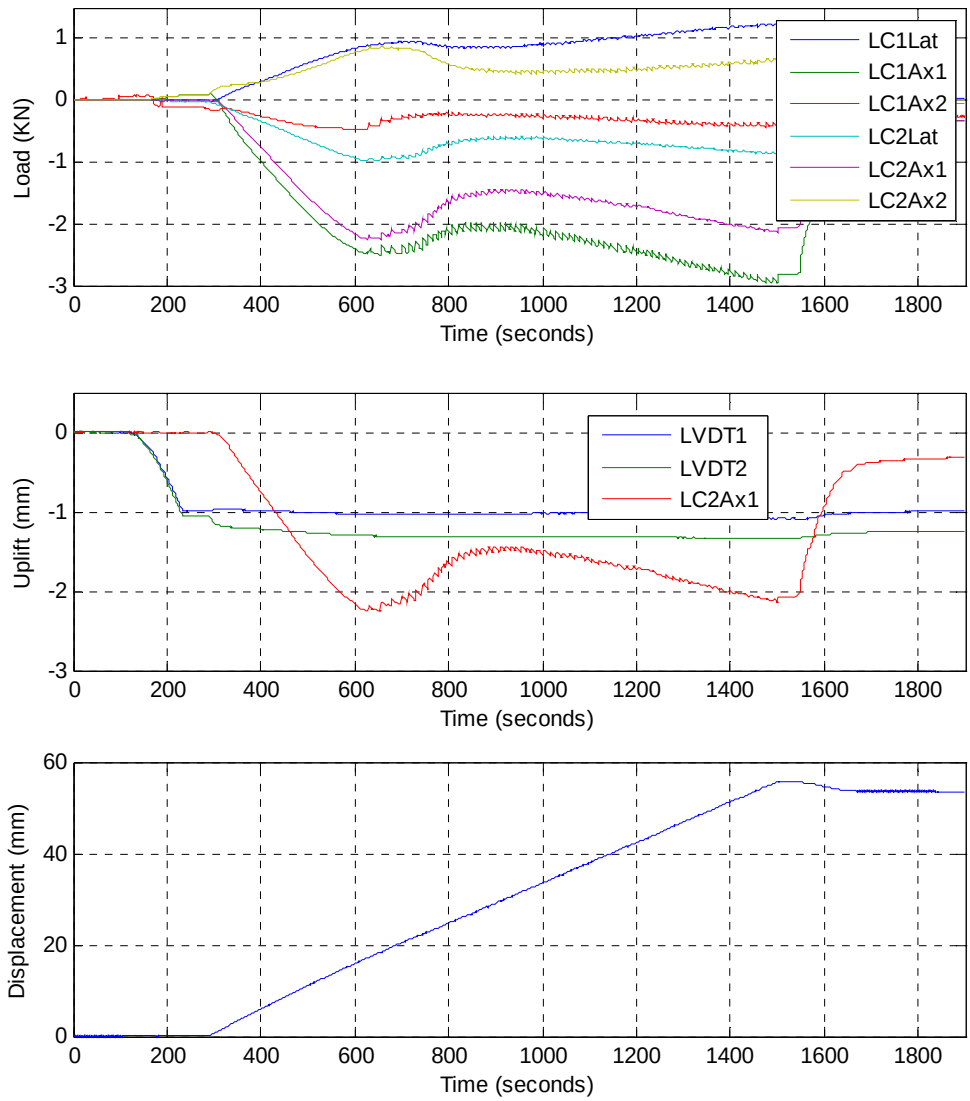

Figure 5-7 Typical data record for pipe displacement in sand

The data acquisition was commenced and the centrifuge accelerated to 45.4 rpm to apply 12.3g at the pipe elevation. The soil bed was consolidated under the increased gravity. This was near instantaneous for the dry sand testbed. It took about five hours to consolidate the soil sample with a water table set at the pipe invert. The progress of consolidation was monitored by pore water pressure dissipation and surface settlement.

A typical data record for pipe displacement in sand is shown in Figure 5-7. The 3 figures show a) the three components of load measured by the two load cells, b) the uplift of both ends of the pipe section with respect to the carriage (referenced to a load cell component), and c) the carriage displacement. The centrifuge was accelerated to test speed between 100 and 250 seconds. There was no subsequent consolidation. The pipe was moved via horizontal actuator between 300 and 1500 seconds. The rate of pull for all experiments was 0.4mm/sec for all tests. The total displacement of the pipe was in the range of 1.5-2D. The movement distance was measured by using a laser distance finder. The pipe loads were relieved by moving the carriage back slightly between 1550 and 1650 seconds. The centrifuge was then stopped.

After all in-flight activity had been completed; the package was photographed and then removed from the centrifuge. Hand shear vane and water content tests were done to confirm the undrained shear strength of clay soil.

5.4.4 Clay shear strength and water content

Up to 6 undrained shear strength measurements were measured using a hand vane for the clay soil before and after each test flight. Water content profiles were also measured post test, Figure 5-8. Table 5-2 shows that the native soil properties for the last three tests were reasonably the same in terms of water content and post-test undrained shear strength. The first lateral pipe test showed post test strength lower than the other 3 tests, with a consistently higher water content.

Table 5-2 Clay test strength and water content summary

	Average Undrained Shear Strength (kPa)		Average Water content (%)	Inflight shear strength (kPa)
Test	Pre-test	Post-Test		
Lateral	21.3	16.8	30.5	25
60 deg	19.2	20.0	29.7	30
20 deg	19.7	19.8	29.7	30
Axial	20.7	20.0	29.7	30

The undrained shear strength from post test vane shear tests is different from in-flight shear strength due to stress relaxation and other effects, Bolton et al (1993). The vane shear tests were performed in at 1g, while the pipes were pulled under higher effective stresses at 12.3g level. Water content and inflight shear strength measurements made by Paulin et al (1995) for very similar soil conditions were correlated to estimate the soil undrained shear strength during a test under 12.3g acceleration,. The inflight shear strength was found to vary from 25 to 30kPa for the 4 clay tests, Table 5-2.

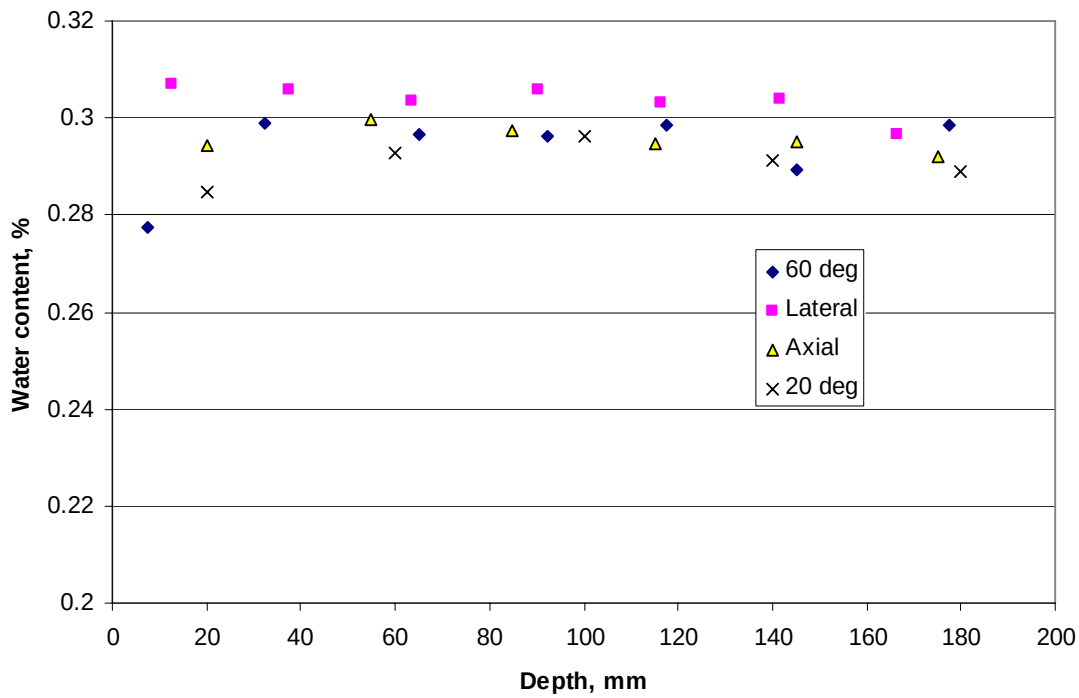

Figure 5-8 Water content profiles for clay tests

5.5 Sand Test Results

The four centrifuge model tests in sand were completed following the procedures and techniques described above. The pipe section was displaced purely axially, laterally, Figure 5-9, and at 60 and 20 degrees to the pipe axis in tests 1 to 4. The displacement exceeded one pipe diameter to fully mobilize the peak resistances normal to and along the pipe axis as shown in Figure 5-10. The results of the finite element analyses are compared to these data from reduced scale physical model tests in section 5.7.2.

Figure 5-9 Pipe segment after lateral loading, sand test 1.

The pipe response is normalized for displacement by the pipe diameter, D and for load by the product of the bulk weight, γ, pipe diameter, burial depth, H and the pipe segment length, L in Figure 5-11. Each test result is shown by a pair of lines of the same colour. The solid line corresponds to the lateral resistance and the dashed line to the axial resistance. The lateral test mobilised some axial resistance and was therefore not a pure lateral displacement. The 20 and 60 degrees tests show very similar patterns of response in both load components. In each of these tests the first peaks in both lateral and axial resistance occurred at the same pipe displacement of 0.45 and 0.9D.

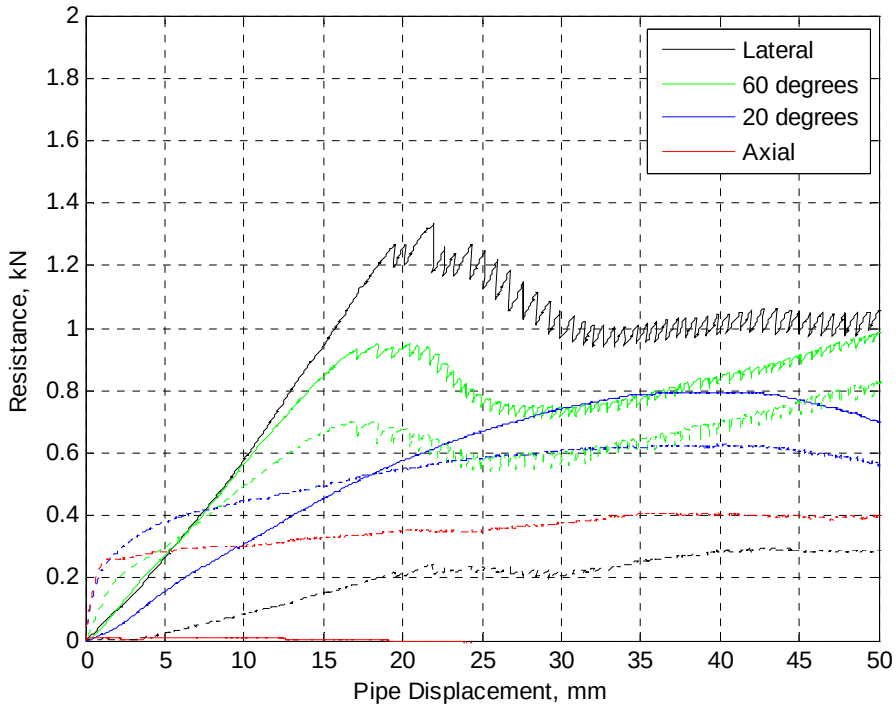

Figure 5-10 Pipe response during sand tests

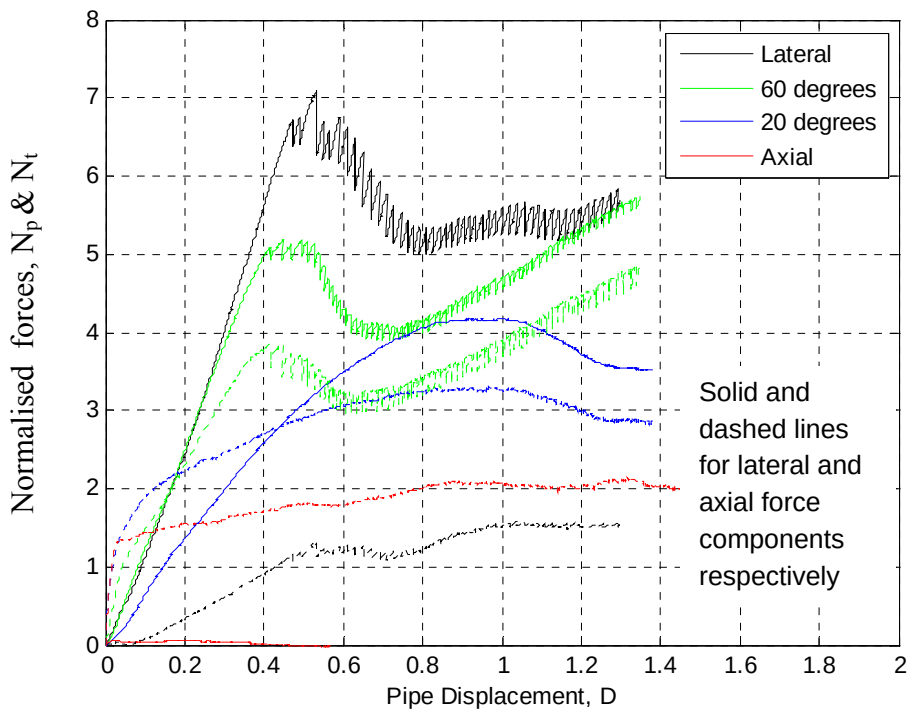

Figure 5-11 Normalized pipe response from sand tests

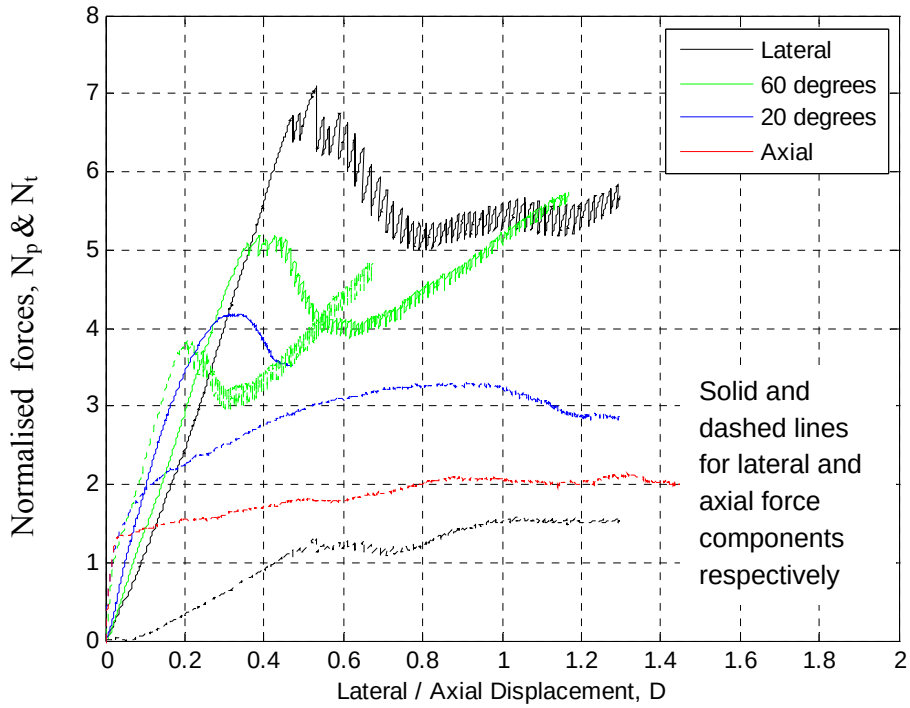

Figure 5-12 Normalized pipe response with displacement vectors from sand tests

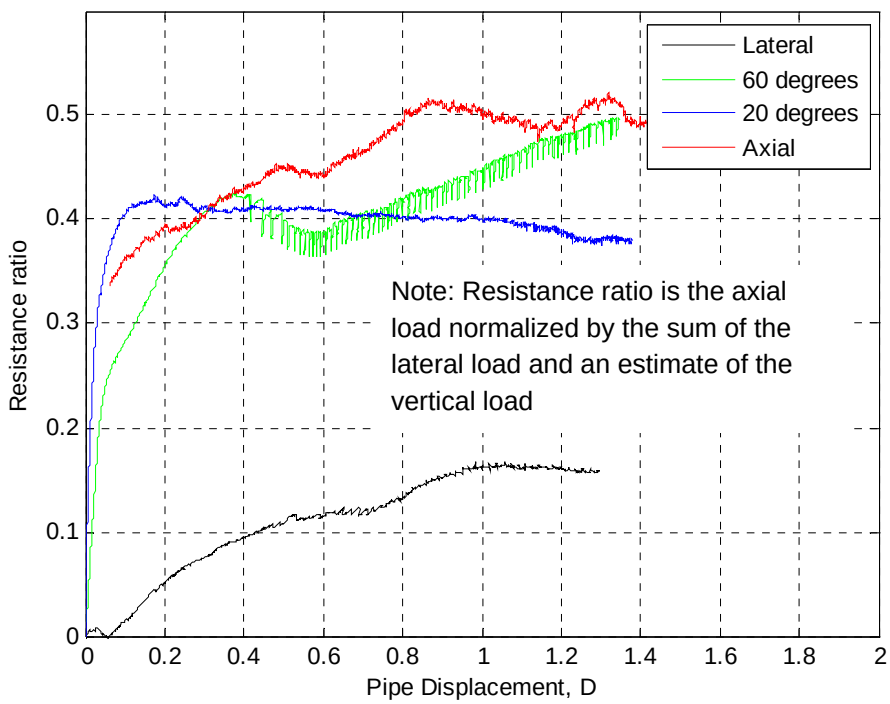

Figure 5-13 Axial resistance ratio for sand tests

The pipe displacement is decomposed into the axial and lateral pipe displacement components, Figure 5-12. The lateral load mobilization follows practically the same backbone 'elastic' curve before peak load. The lateral, 60 and 20 degree tests peak at decreasing lower load levels as increasingly more strength capacity is mobilised in the axial direction. The displacement to peak load, up to 0.5D for the lateral test, is greater than expected from Honegger and Nyman (2001). This is attributed to sand disturbance (similar to trench effects) around the pipeline during sand placement, Phillips et al (2004).

The lateral to axial load curve similarity observed in Figure 5-11 is further investigated by assessing the axial resistance ratio, Figure 5-13. The ratio is determined by dividing the axial load resistance by the lateral load resistance and an estimate of the initial soil self weight load acting around the pipe perimeter, taken as 0.5(1+Ko)γ HDL and assuming Ko is unity. This ratio is presented against the normalized axial pipe displacement in Figure 5-14. The 4 tests follow a remarkably similar pattern, even for the initial stiffness of the lateral test result, despite the vertical load estimate. The first axial load peak is around 0.1D, 4mm, consistent with the new PRCI guidelines at a ratio of between 0.4 and 0.5. The 0.4 plateau ratio is consistent with the interface friction coefficient of the dry sand acting on the steel pipe surface of around 22 degrees.

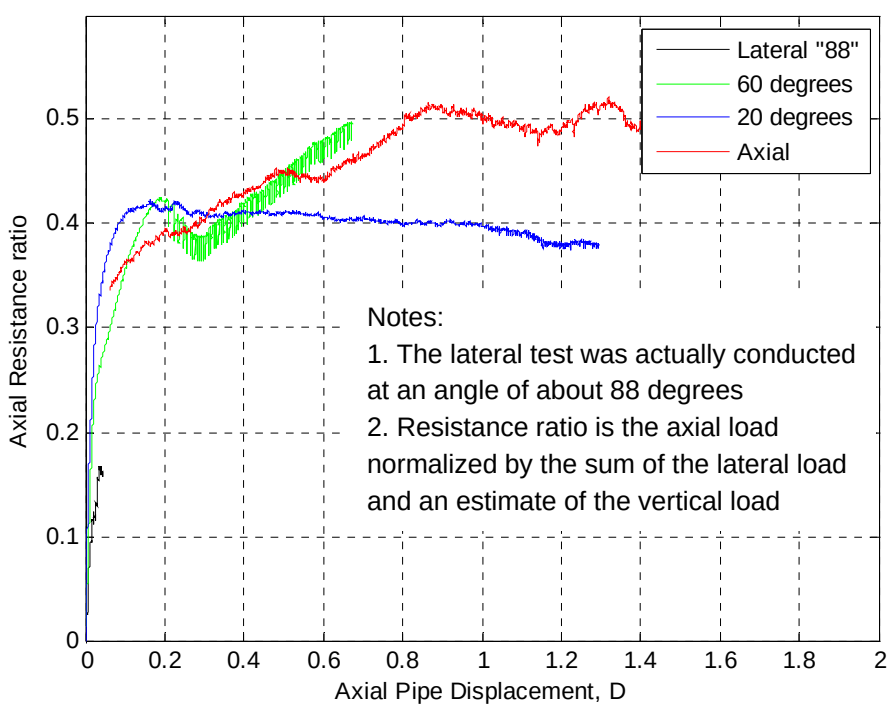

Figure 5-14 Axial resistance ratio development with axial displacement

5.6 Clay Test Results

The four centrifuge model tests in medium silty clay were completed following the procedures and techniques described above. The pipe section was displaced purely laterally, at 60, Figure 5-15, and 20 degrees to the pipe axis and axially in tests 5 to 8. The displacement exceeded one pipe diameter to mobilize the peak resistances normal to and along the pipe axis as shown in Figure 5-16. (The spikes in the axial load trace for the 20 degrees test were artifacts from the apparatus). The results of the finite element analyses are compared to these data from reduced scale physical model tests in section 5.7.1.

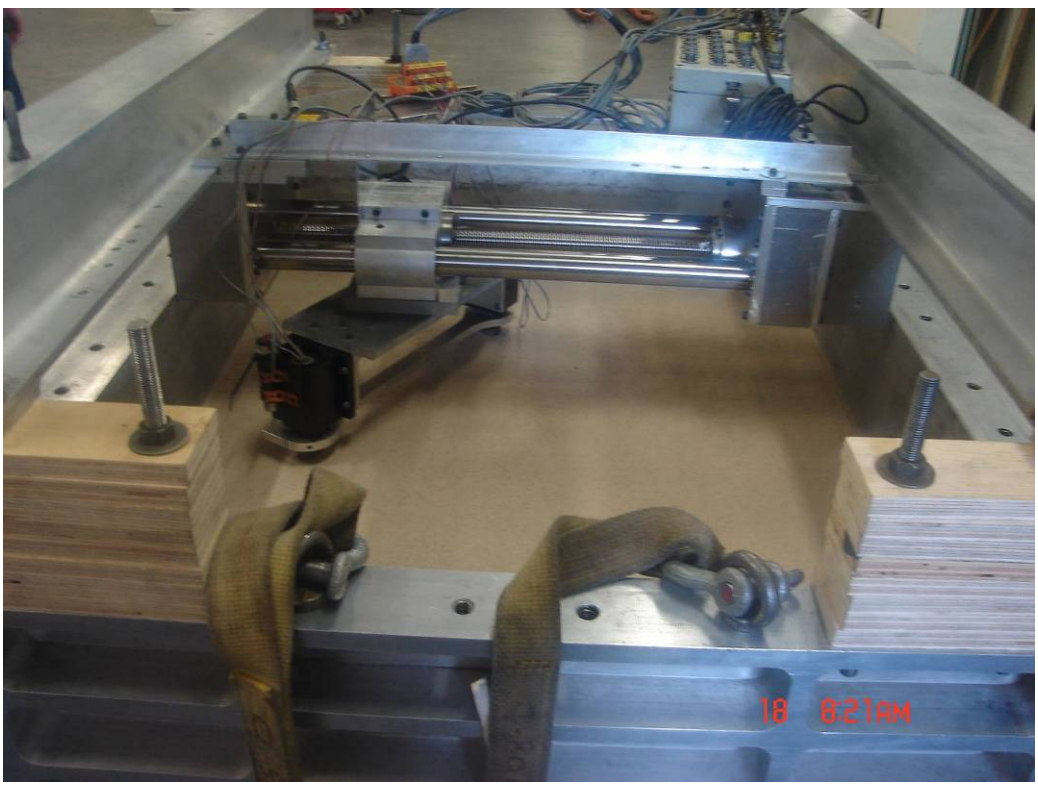

Figure 5-15 Model Test of Inclined Pipeline Loading in Clay

The pipe response is normalized for displacement by the pipe diameter, D and for load by the product of the undrained strength, C_u, pipe diameter and the pipe segment length, L in Figure 5-17. Each test result is shown by a pair of lines of the same colour. The solid line corresponds to the lateral resistance and the dashed line to the axial resistance. The 20

and 60 degrees tests show very similar pattern of response to both load components. In each of these tests the peaks in lateral and axial resistance occurred near the maximum pipe displacement. The 20 and 60 degree tests mobilize a much higher axial resistance than the purely axial test. The axial test capacity is not then controlled by the limited undrained strength. Rather, the additional axial capacity results from the frictional resistance provided by the mobilized lateral resistance.

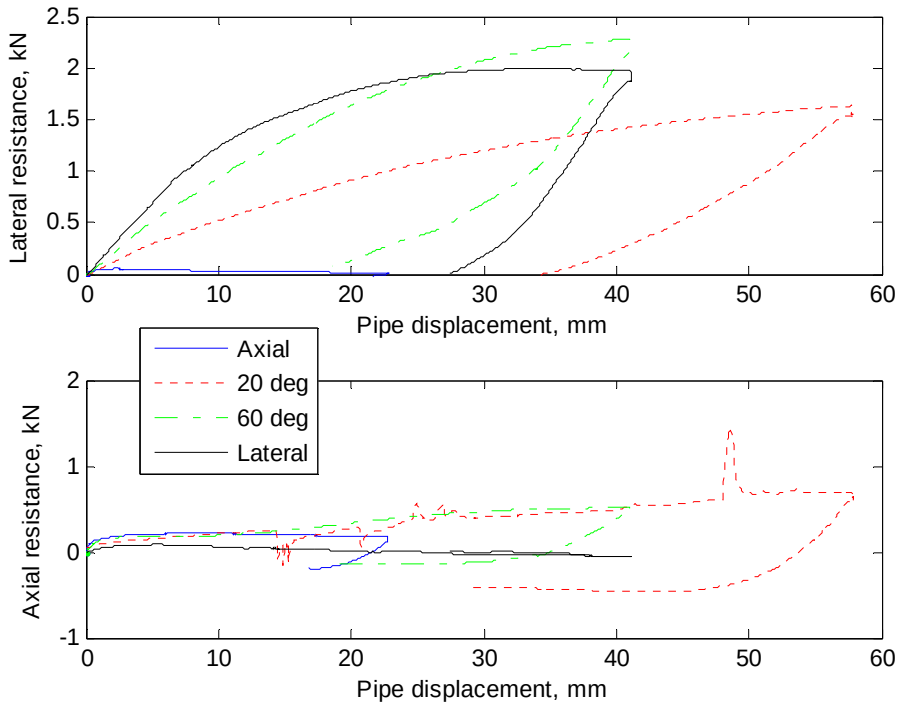

Figure 5-16 Pipeline Force Response under Inclined Loading

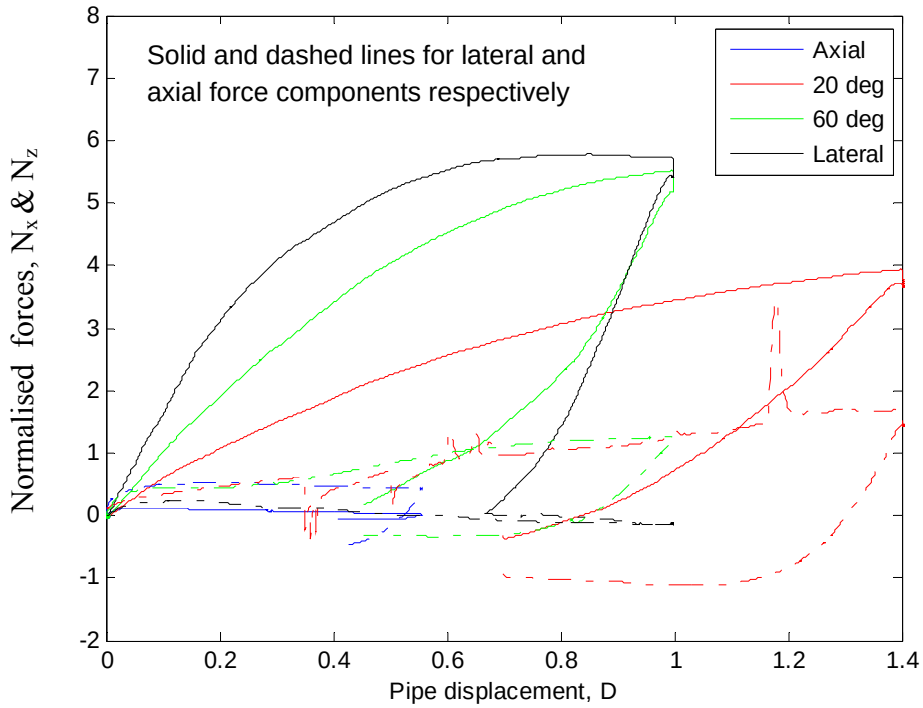

Figure 5-17 Normalized pipe response from clay tests

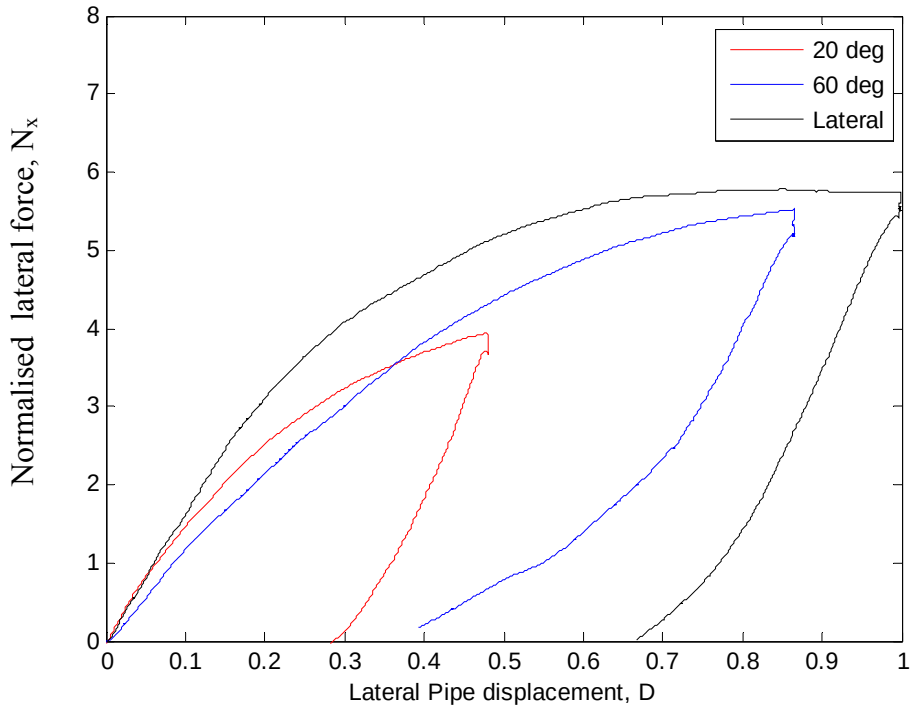

Figure 5-18 Normalized lateral pipe response with displacement vectors

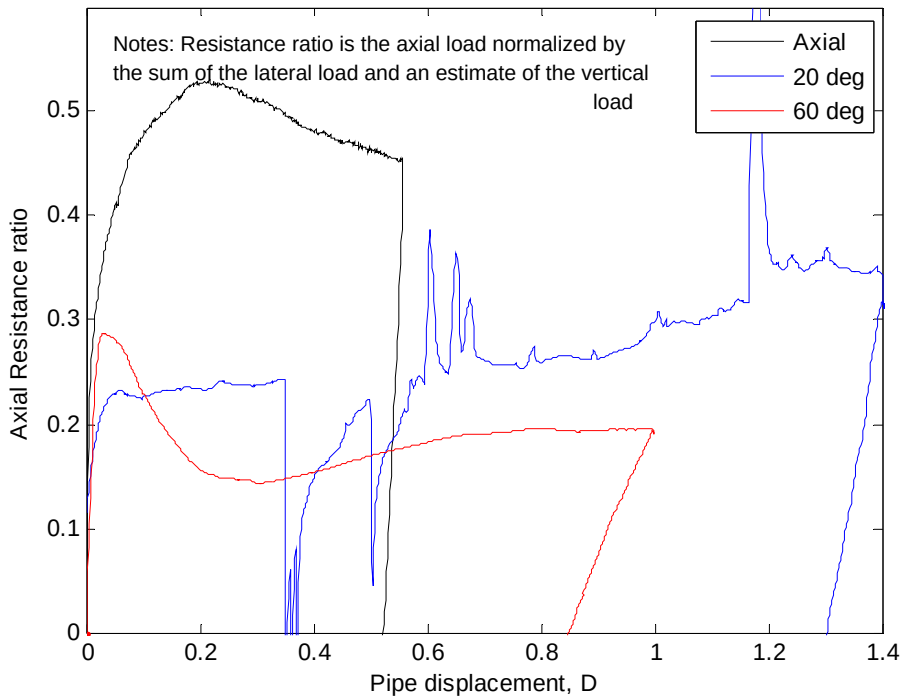

Figure 5-19 Axial resistance ratio development with axial displacement

The pipe displacement is decomposed into the lateral pipe displacement component, Figure 5-18. The lateral load mobilization follows practically the same backbone 'elastic' curve before peak load. The lateral, 60 and 20 degree tests peak at decreasing lower load levels as increasingly more strength capacity is mobilised in the axial direction. The displacement to peak load, up to 0.7D for the lateral test, is greater than expected from Honegger and Nyman (2001). This is again attributed to 'trench effects' around the pipeline, Phillips et al (2004).

The lateral to axial load curve similarity observed in Figure 5-17 is further investigated by assessing the axial resistance ratio, Figure 5-19. The ratio is determined by dividing the axial load resistance by the lateral load resistance and an estimate of the initial soil self weight load acting around the pipe perimeter, taken as $0.5(1+Ko)\gamma$ HDL and assuming Ko is unity. The axial test ratio is consistent with the friction coefficient between the pipe and soil, similar to observed in Figure 5-14 for sand.

The assessed ratio decreases to around 0.3 and 0.2 for the 20 and 60 degree tests. This is attributed in the former test to the generation of positive excess pore pressures around the front face of the pipe. These decrease the effective normal stress acting on the pipe which

reduces the frictional axial resistance. The 60 degree test is also similarly affected, and further the increased lateral resistance component decreases the available axial capacity given the finite shear strength. The first axial load peak is around 0.2D, 8mm, consistent with the new PRCI guidelines.

5.7 Numerical & Physical Model Comparison

5.7.1 Clay tests

The measured pipe response is compared in a normalized form to finite element predictions in Figure 5-20 to Figure 5-23 for loading lateral, at 60 and 20 degrees to the pipe axis and in the axial direction respectively. The finite element analysis comparison was similar to that presented in section 1 but using the actual test geometry and soil strength parameters. However, the axial resistance along the pipe was controlled by the pipe soil interface friction, after C-CORE (2003) rather than a limiting shear stress as used in section 3.2. Effective stresses and pore pressure generation were not considered as the analyses in this report for clay assume undrained behaviour with the soil as a single phase material.

The predicted peak loads for all 4 load cases for both the axial and lateral loading components are close to the asymptotes from the measured loads. This was the focus for these limit load analyses. The initial loading, including the elastic response, is not well predicted. This prediction could be improved by including the trench effects in the analyses as well as a more complex calibrated soil model with sub-yield plasticity, as demonstrated in section 4.6 and C-CORE (2003). The unloading curves in the experiments provide a better comparison to the initial loading in the analyses, as trench effects and sub-yield behaviour are not so pronounced.

The key observation in both the experimental and numerical results is the comparative behaviour of the axial to lateral resistance components. Although the lateral loading was conducted under undrained conditions, the axial resistance is not limited to a constant fraction of the undrained shear strength. The peak normalized pure axial resistance, Figure 5-23 of 0.45 is equivalent to an α factor of 0.14 for an undrained strength of 30kPa. This factor is consistent with Paulin et al (1998) and Rizkalla et al (1996), Figure 2-2. These factors are lower than the PRCI guideline value of around unity. Under oblique 20 degree loading, the normalized axial resistance peaks between 1 and 1.5 in the numerical and experimental results, Figure 5-22. That's a two to three fold increase in the

α factor. This increase is attributed to the development of frictional axial resistance from the increased lateral bearing load.

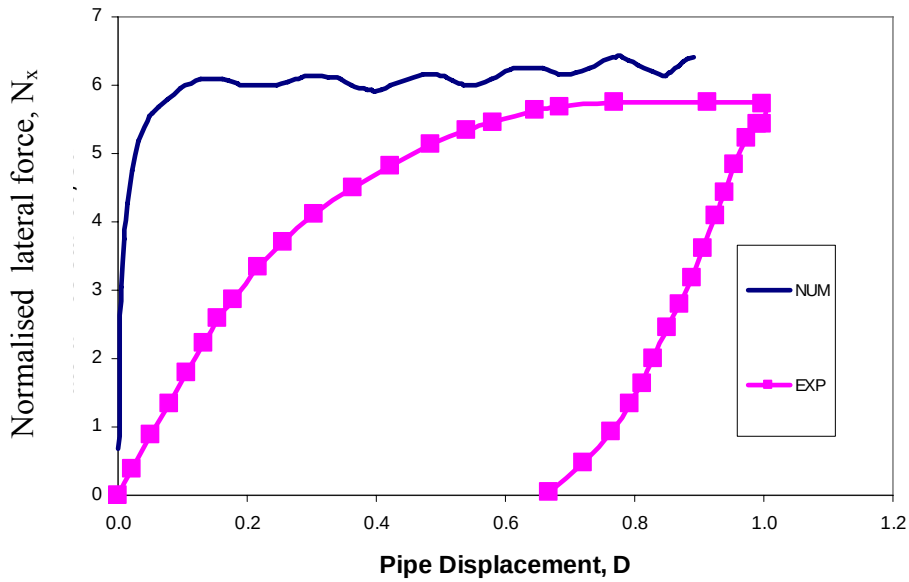

Figure 5-20 Pipe response comparison for lateral clay test conditions

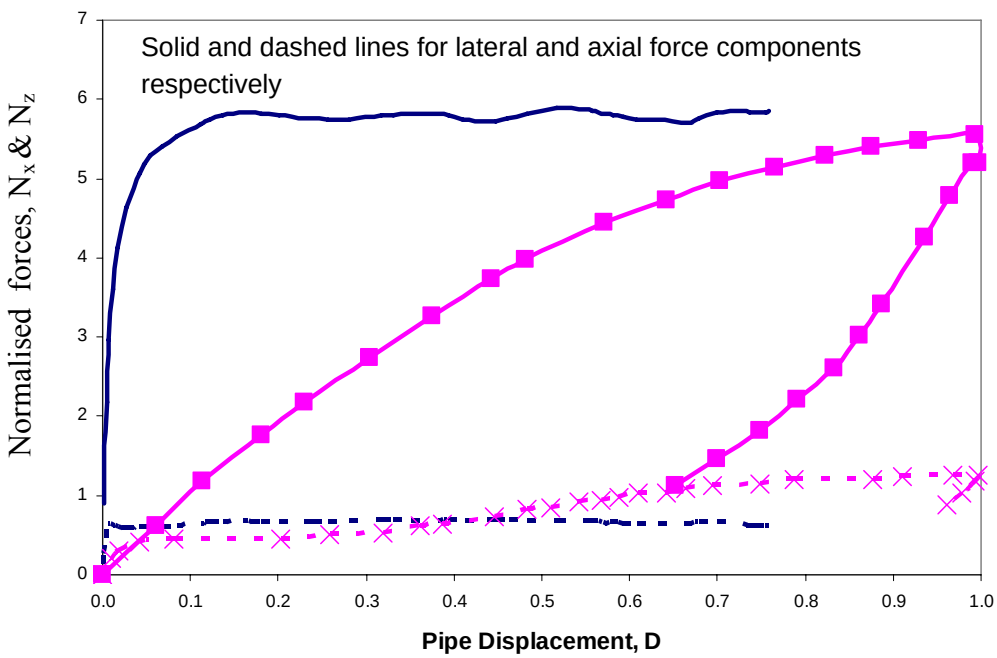

Figure 5-21 Pipe response comparison for 60 degree clay test conditions

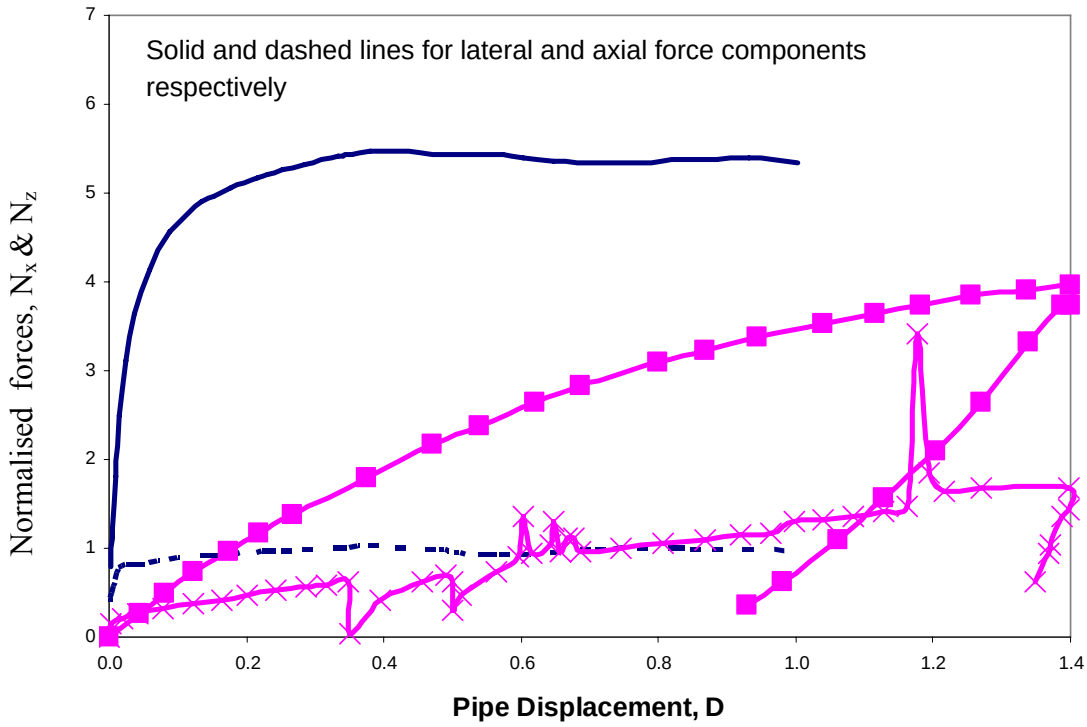

Figure 5-22 Pipe response comparison for 20 degree clay test conditions

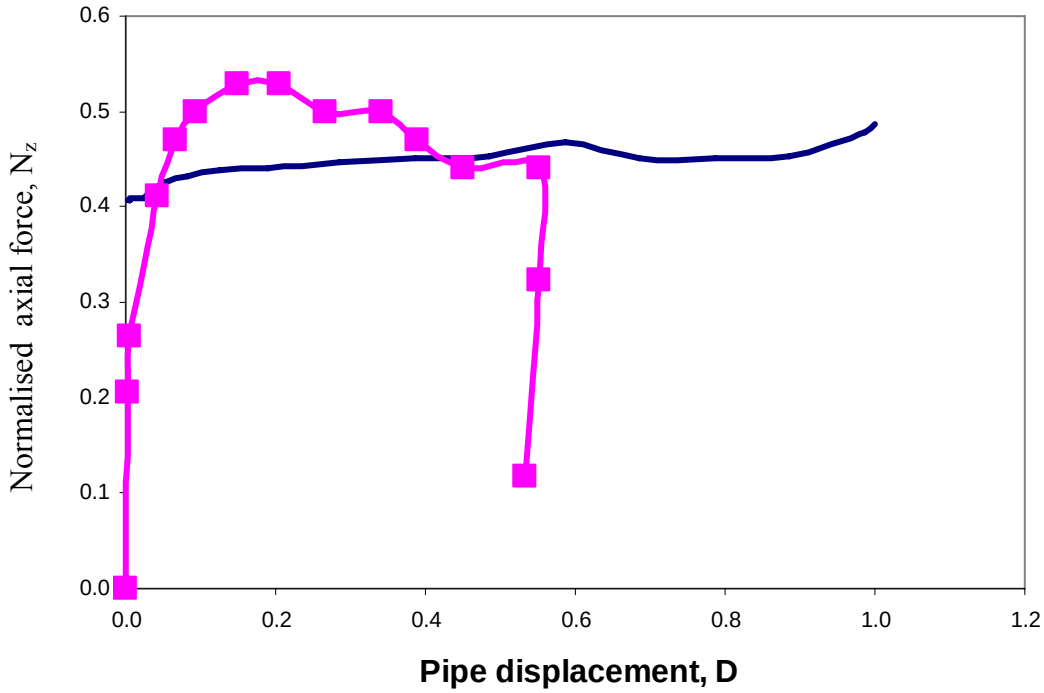

Figure 5-23 Pipe response comparison for axial clay test conditions

5.7.2 Sand tests

The normalized pipe response to oblique loading in sand can be compared for the experimental and numerical results between Figure 5-11 and Figure-4-12 & Figure 4-15. The experimental results, Section 5.5 are for an H/D ratio of 1.85 in dry sand with a peak friction angle of 42 degrees, section 5.4.1. The numerical results are for H/D ratios of 1.5 and 2.5 with a peak friction angle of 46 degrees, Table 4-1 and section 4.4.

The form of the pipe loading curves is similar with post peak softening followed by increased resistance from surcharging effects, Figure 5-11 and Figure 4-15. The magnitudes of the curves are not compared due to the use of finite cohesion in the analyses for numerical stability, Table 4-1. The physical tests have a larger displacement to peak load partly due to the effect of local sand density variations immediately around the pipe installation which was not simulated in the analyses.

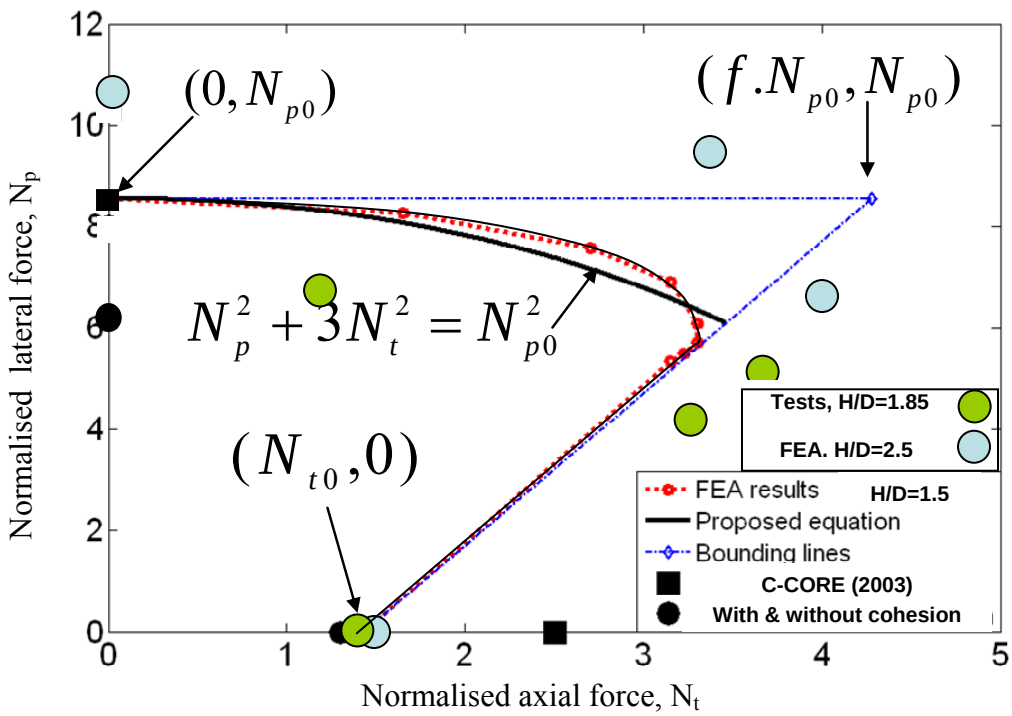

Figure 5-24 Interaction diagram for oblique loading in sand, H/D ~ 2

The peak axial and lateral resistance components are compared in Figure 5-24, developed from Figure 4-16. The numerical results in red and cyan are for burial depths, H/D of 1.5 and 2.5 respectively. The latter results are from Figure-4-12f. The test results for H/D of 1.85 are the 4 points in green. The 4 points are for axial, 20 degree, 60 degree to lateral

loading with increasing lateral resistance. The envelopes formed by the 3 datasets are very similar in shape, and comprise of 2 failure criteria. The lower criterion is for failure along the pipe soil interface, and the upper criterion for failure through the soil mass in bearing. For the 60 degree loading, both numerical analyses clearly predict failure for the upper criteria. In the physical test, failure is close to the intersection of the two criteria, or maybe controlled by failure along the pipe interface.

All 3 datasets show the pure axial resistance around 1.3 to be consistent with the guideline value proposed in C-CORE (2003) assuming only friction with no cohesion. The pure lateral resistance guideline comparison to the numerical analysis was discussed in section 4.5. The pure lateral guideline value for no cohesion is consistent with the physical test lateral value, given the slight differences in burial depth and peak friction angle.

Overall, there is good consistency for the peak axial and lateral load components between the physical data, the numerical analyses and the C-CORE (2003) guidelines, including the proposed bounding equations described in section 3.4.2.

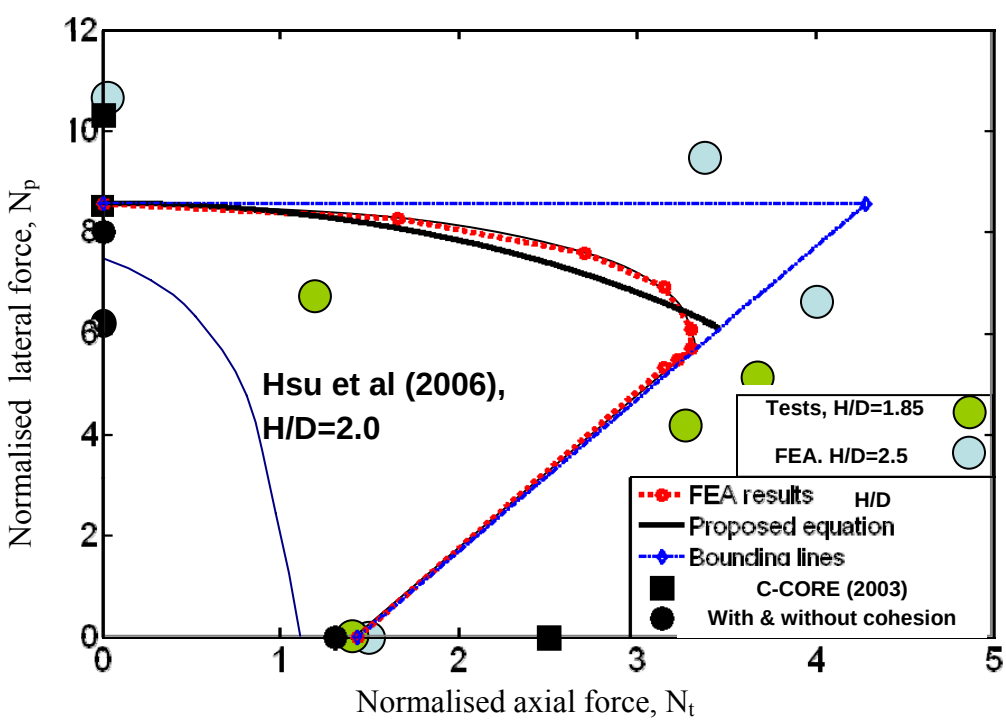

Figure 5-25 Interaction diagram comparison for oblique loading in sand, H/D ~ 2

Hsu et al (2006) present comparable results of oblique physical load tests for steel pipe segments of either 0.15 or 0.23m diameter buried at an H/D of 2.0 in dry dense sand with a peak friction angle of 42 degree. They developed closed form solutions to fit their measurements, Figure 2-14. Their resulting interaction diagram is superimposed on Figure 5-24 as Figure 5-25. The pure axial and lateral loading results are reasonably consistent with the results of this study. The form of the interaction envelope between these end points is however quite different. The present study from independent physical and numerical results indicates much higher load capacities for oblique loading between the two end points.

The reason for the discrepancy is unknown. However, under oblique loading at say 60 degrees Hsu et al (2006) measurements do not appear to fully mobilise the available soil bearing strength as approximated by equation 3.1. A comparison of test methods and soils may assist in clarifying this discrepancy.

6 IMPROVED PIPELINE RESPONSE MODELING

The structural finite element method (FEM) is generally used to model the mechanical response of a buried pipeline subject to relatively complex ground movement events. The purpose of this assessment was to identify potential alternatives to current practice. This study included an investigation of how this pipe response model could be improved in 3 main areas namely the soil spring formulation, the pipe formulation and using a continuum, rather than a structural, FEM simulation.

In this study, the finite element analysis employed the general purpose, commercial software package ABAQUS/Standard v6.4. A three-dimensional structural finite element model was used to idealise the continuum pipeline/soil interaction behaviour as described in section 2. For the baseline analyses, the pipeline was modeled using 3-node quadratic PPE32 elements, which assumes a constant hoop stress, and the soil response was modeled by 2-node nonlinear SPRINGA elements. Variants to this baseline are described in the following sections.

The pipeline element was formulated on Timoshenko beam theory, which assumes linear elastic transverse shear behaviour, and was defined by three displacement and three rotational degrees of freedom per node using quadratic shape functions. Additional variables account for an average hoop stress due to internal pressure effects and are based on thin-wall pipeline theory. The pipeline stress-strain constitutive relationship was defined by isotropic, elastoplastic behaviour with a von Mises yield surface and isotropic hardening rule. The stress-strain relationship was defined using the Ramberg-Osgood formulation.

The soil response was defined by nonlinear relationships defined by DGHC (2007). The force-displacement relationships were defined at the pipeline springline. A fully backfilled trench with native soil was assumed in the present analysis. The effects of backfilling and trench geometry have been considered in other studies conducted by the authors, eg Phillips et al (2004b).

6.1 Alternative Soil Spring Formulations

Currently, the soil spring formulation is typically considered to be uncoupled as shown in section 2.6. That is the axial, lateral and vertical soil response is assumed to be independent of each other. Soil has limited strength and cannot mobilise its full resistance in each of these directions simultaneously. Section 5.7 clearly demonstrates

dependencies between the axial and lateral soil response from this study. Section 2.7 has demonstrated similar dependencies between the vertical and lateral soil response.

The baseline FEM analysis was modified to account for the axial to lateral soil interaction. The soil was represented by a series of strut elements, rather than the SPRINGA elements. These strut elements had the same elastic stiffness as the springs they replaced. However, the soil resistance limits in the two orthogonal directions were made mutually dependent using Fortran subroutines, following the strategy outlined in Appendix C, Section 11. The effects of independent as compared to dependant behaviour are examined for 3 increasingly complex pipeline systems subject to ground movement.

6.1.1 Simple downslope pipeline movement

The first example was a X60, 20" pipeline with a wall thickness of 8mm buried to a depth of one meter in clay. The pipeline geometry is illustrated in Figure 6-1.

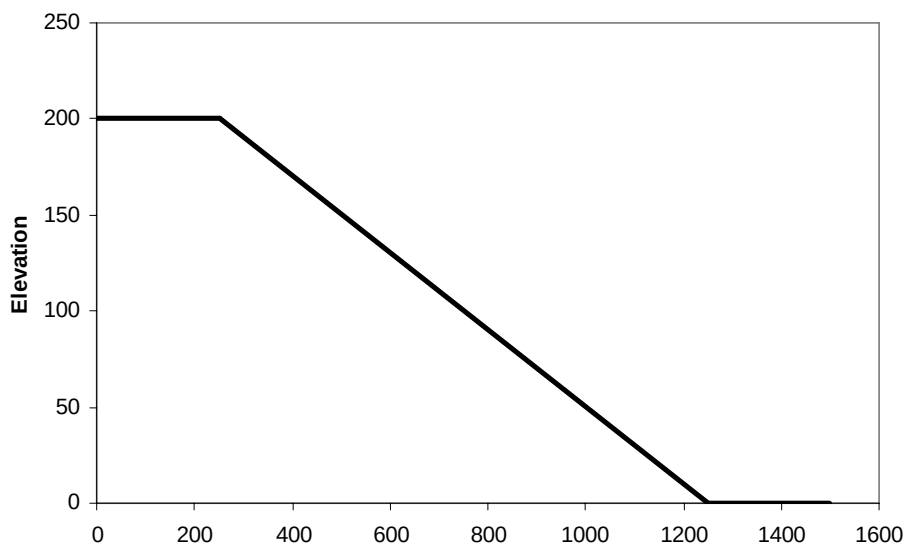

Figure 6-1 Simple downslope pipeline geometry

The soil was considered to have an undrained strength, Su of 30 kPa, an effective unit weight, γ of 8 kN/m3 and a soil-pipe interface friction angle, δ of 20 deg. The soil axial –lateral peak resistance interaction diagram, based on Figure 3-8, as bounded by the dashed lines,

Figure 6-2 represents the proposed soil response limits. The region bounded by the solid lines represents current practice with no interaction.

The pipeline was perturbed by abrupt mid slope soil displacement of 1m magnitude at 30 degrees with respect to pipe centerline over a 250m length. No vertical movement of the pipe was considered

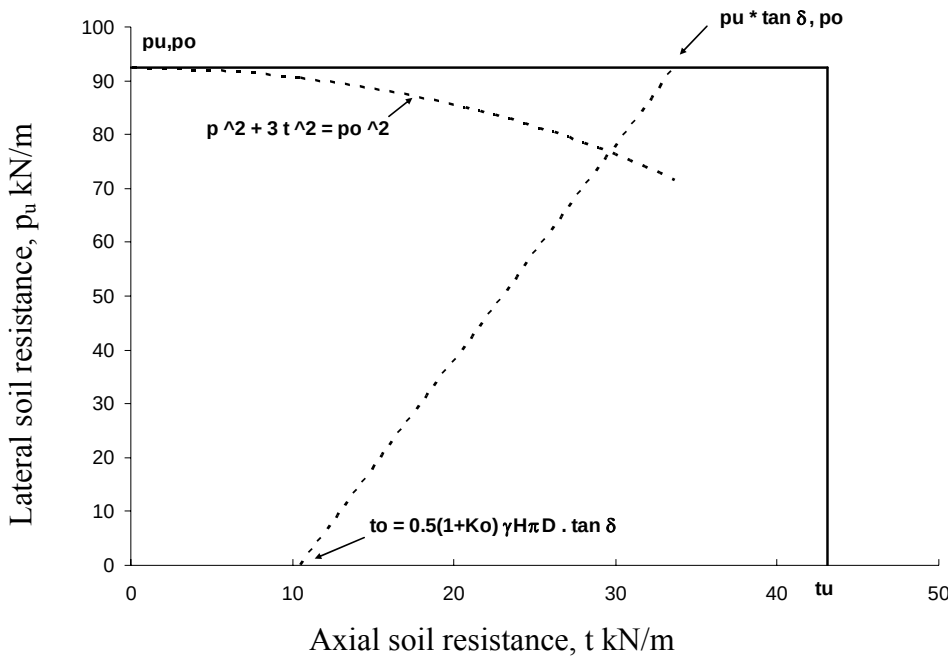

Figure 6-2 Lateral to axial soil reaction interaction diagram

Figure 6-3 and Figure 6-4 present a summary of results. The results show that, by accounting for the axial to lateral interaction, the strain developed in the pipeline is reduced. The maximum compressive strain considering interaction is about 0.8%.

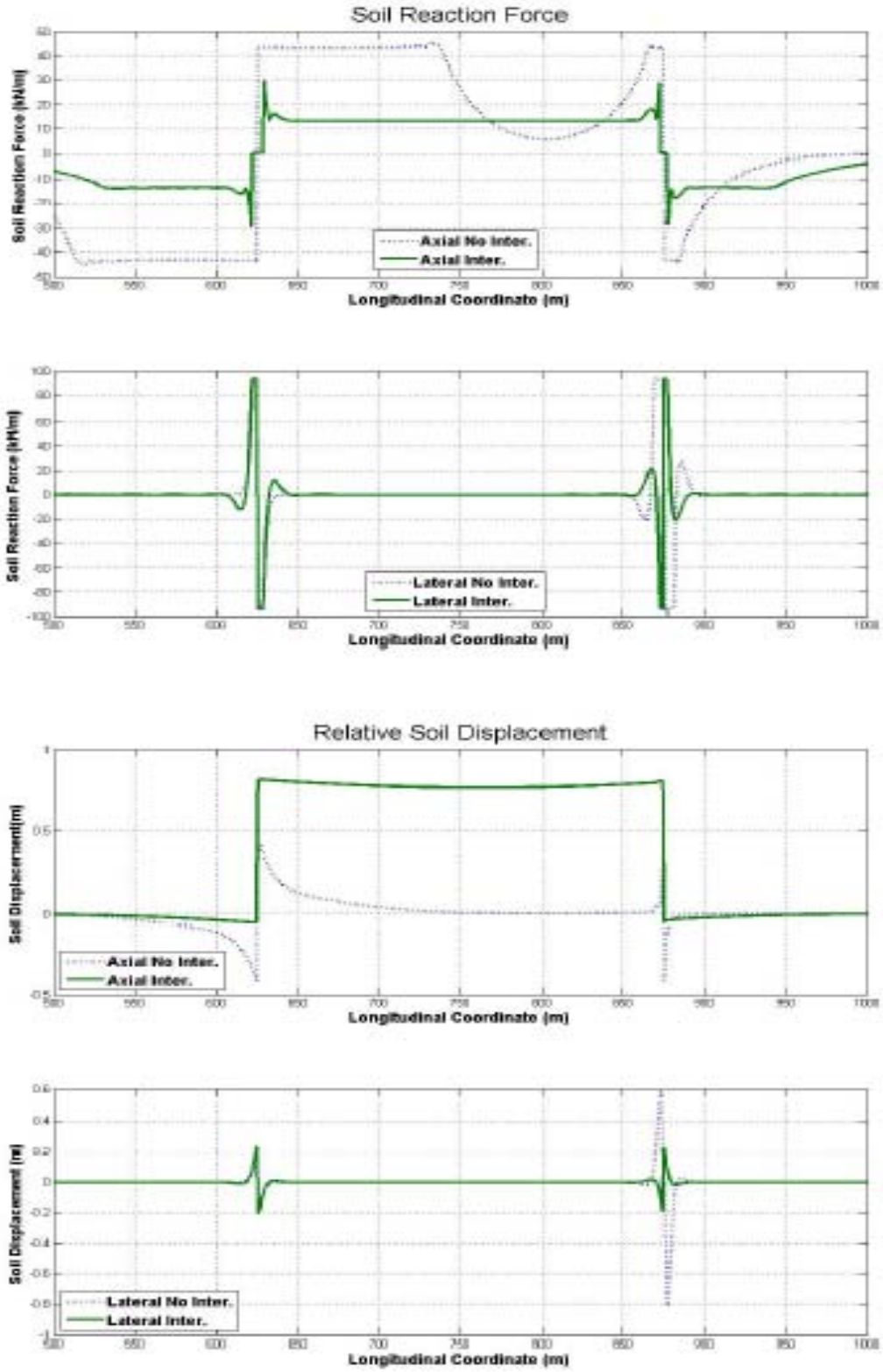

Figure 6-3 Simple downslope pipe-soil response

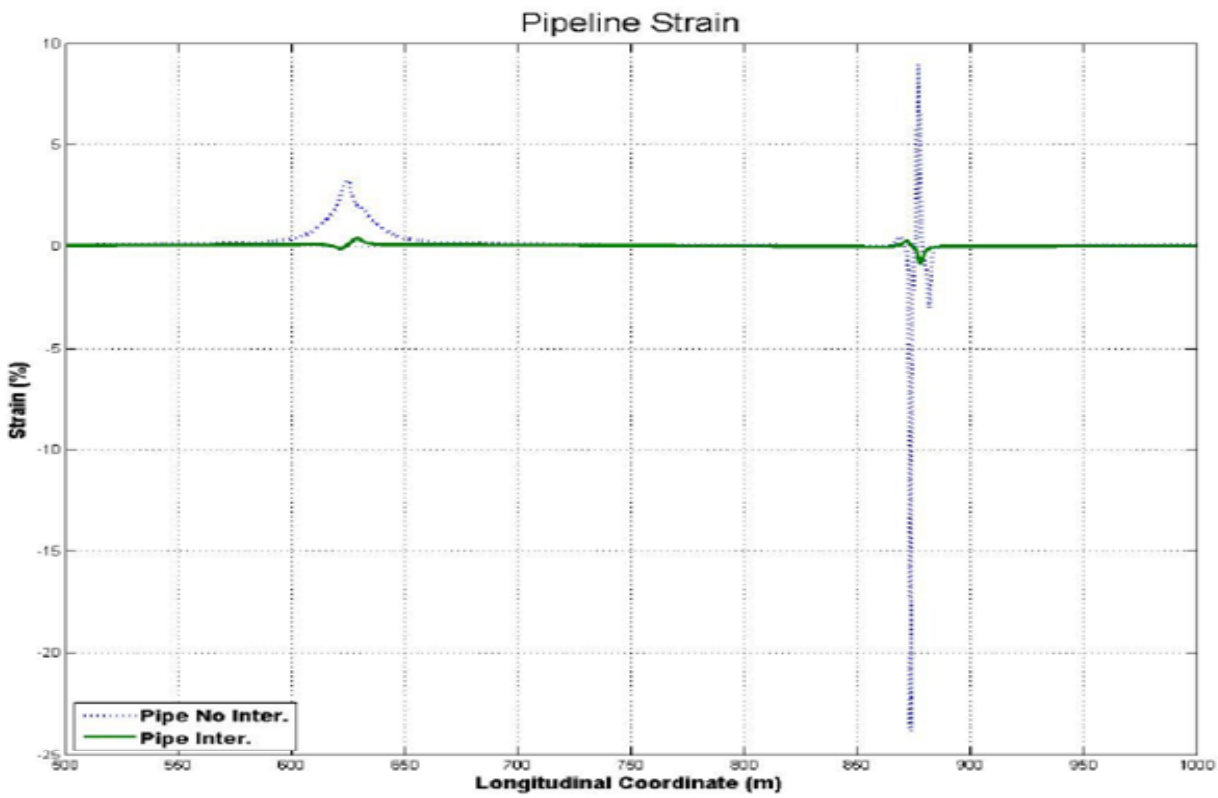

Figure 6-4 Simple downslope pipeline strain response

6.1.2 Simple lateral slide

The second example considers a 600m long pipeline in clay crossing a 50m wide lateral slide. The pipe has an outside diameter of 0.406m, a wall thickness of 12.9mm and is of 414 MPa grade, with an internal pressure of 7.5MPa. The native and backfill soil is a clay of 80kPa undrained shear strength. The 3 orthogonal soil reactions, for no interaction, were defined by DGHC (2007) as shown in Table 6-1. The axial and lateral independent reactions are superimposed on Figure 6-5 which shows the dependency assumed between the axial and lateral reactions, based on the maximum lateral reaction and the interface friction between the pipe and soil. The maximum dependant axial resistance slightly exceeds the prescribed t_u value for this analysis, but is not capped at the t_u value.

Table 6-1 Simple lateral slide soil independent reactions

tu_(kN/m)	xu_(m)	pu_(kN/m)	yu_(m)	qu_u_(kN/m)	zu_u_(m)	qu_d_(kN/m)	zu_d_(m)
80.4	0.005	311.63	0.069	217.97	0.135	311.6	0.089

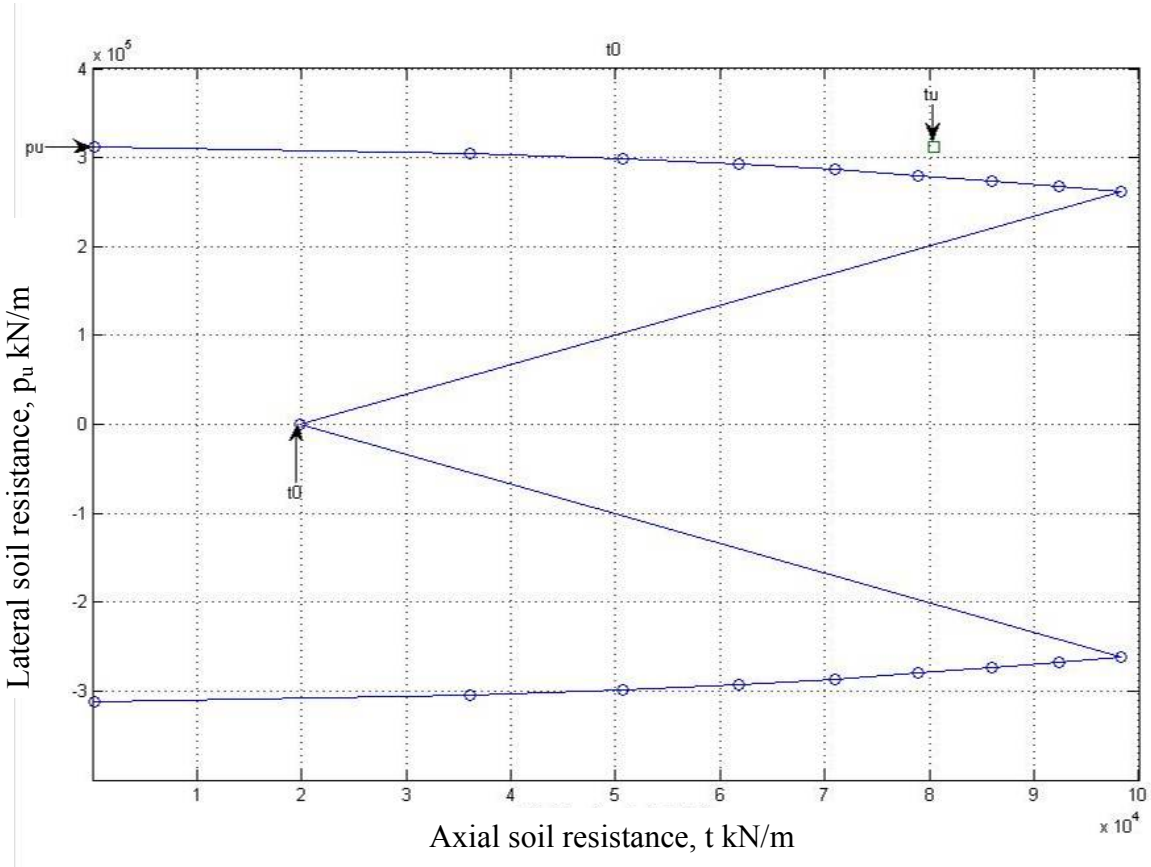

Figure 6-5 Lateral slide soil reaction interaction curve

Figure 6-6 and Figure 6-7 compare the pipe response without and with consideration of the interaction effect to a simple 5m lateral slide movement. Figure 6-7 indicates a slight boundary effect on the pipe response, this analysis was rerun considering a much longer pipe length with practically identical results. Again, consideration of the interaction reduces the maximum pipe strains from 6.8 to 4.0%. Conversely, a longer length of pipeline outside of the slide area is affected due to the reduction in axial resistance in the absence of mobilised lateral load. A slight boundary effect is introduced by this length increase. The comparison is repeated for a 5m displacement for a near lateral slide movement crossing the pipe axis at 30 degrees. Similar observations are seen in Figure 6-8 and Figure 6-9 with the pipe strain reducing from 2.9 to 2.3% due to the interaction effects, and a longer zone of influence. Figure 6-9 indicates a slight boundary effect on the pipe response, this analysis was rerun considering a much longer pipe length with practically identical results.

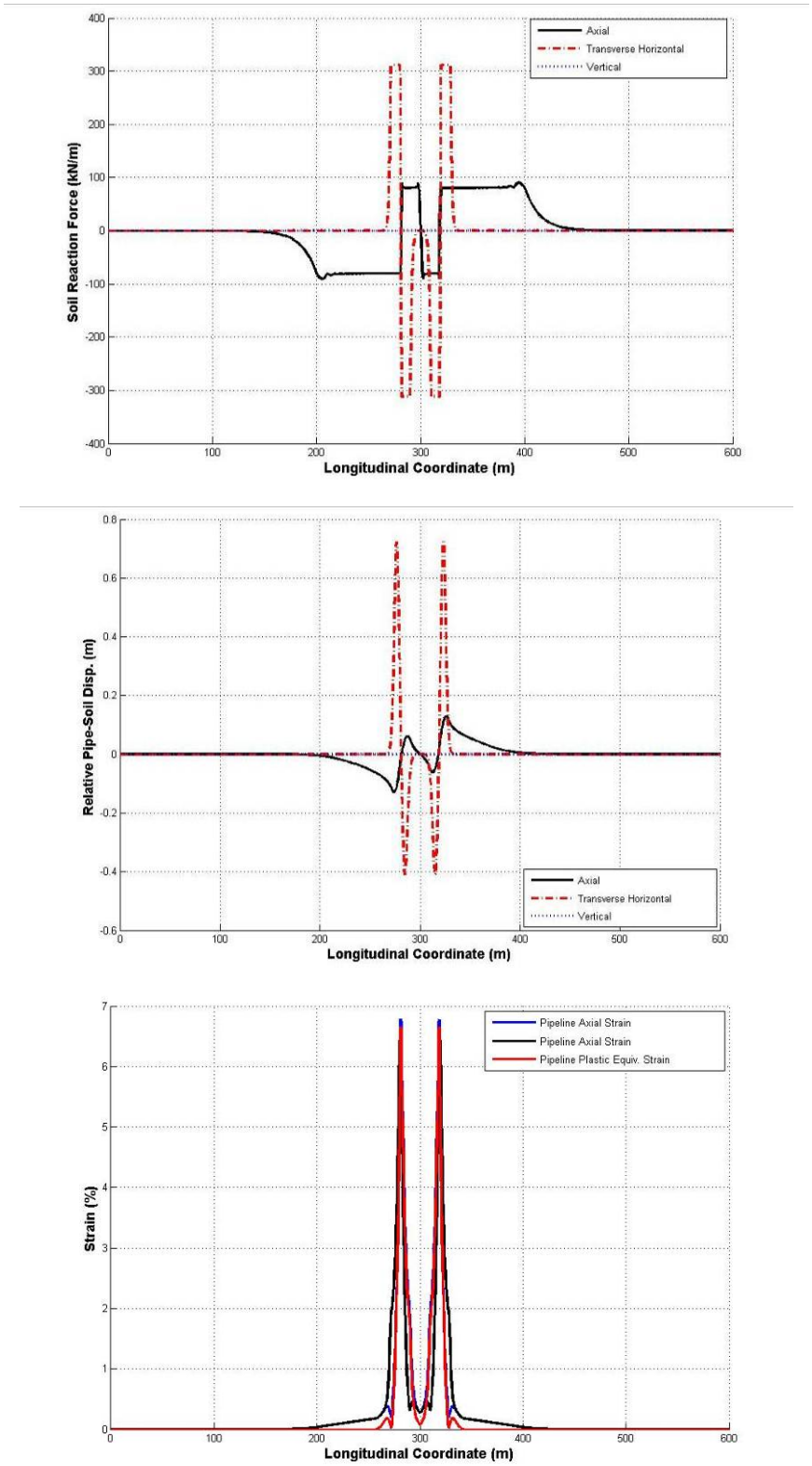

Figure 6-6 Simple lateral pipe-soil response with no interaction effect:

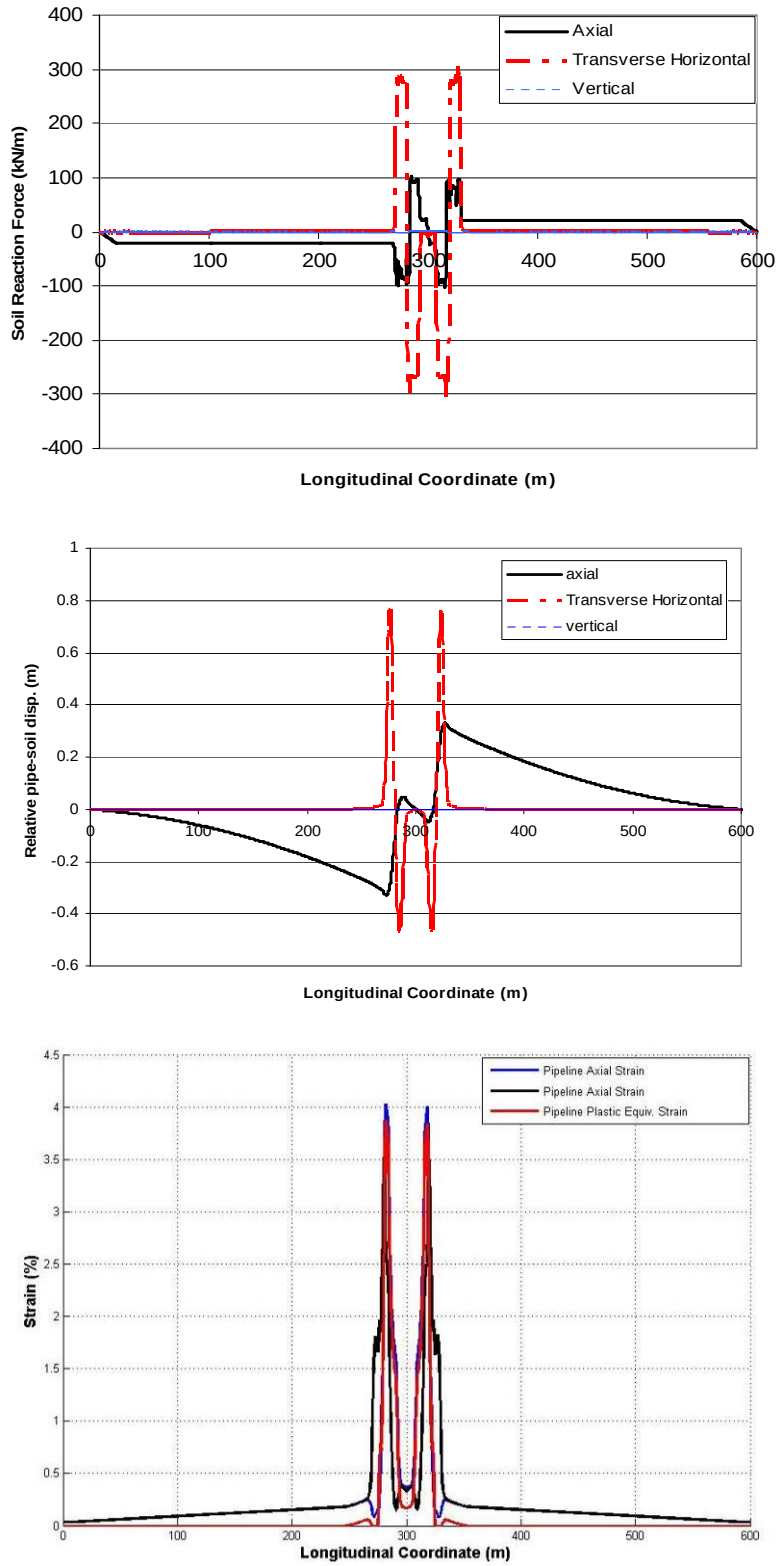

Figure 6-7 Simple lateral pipe-soil response considering the interaction effect

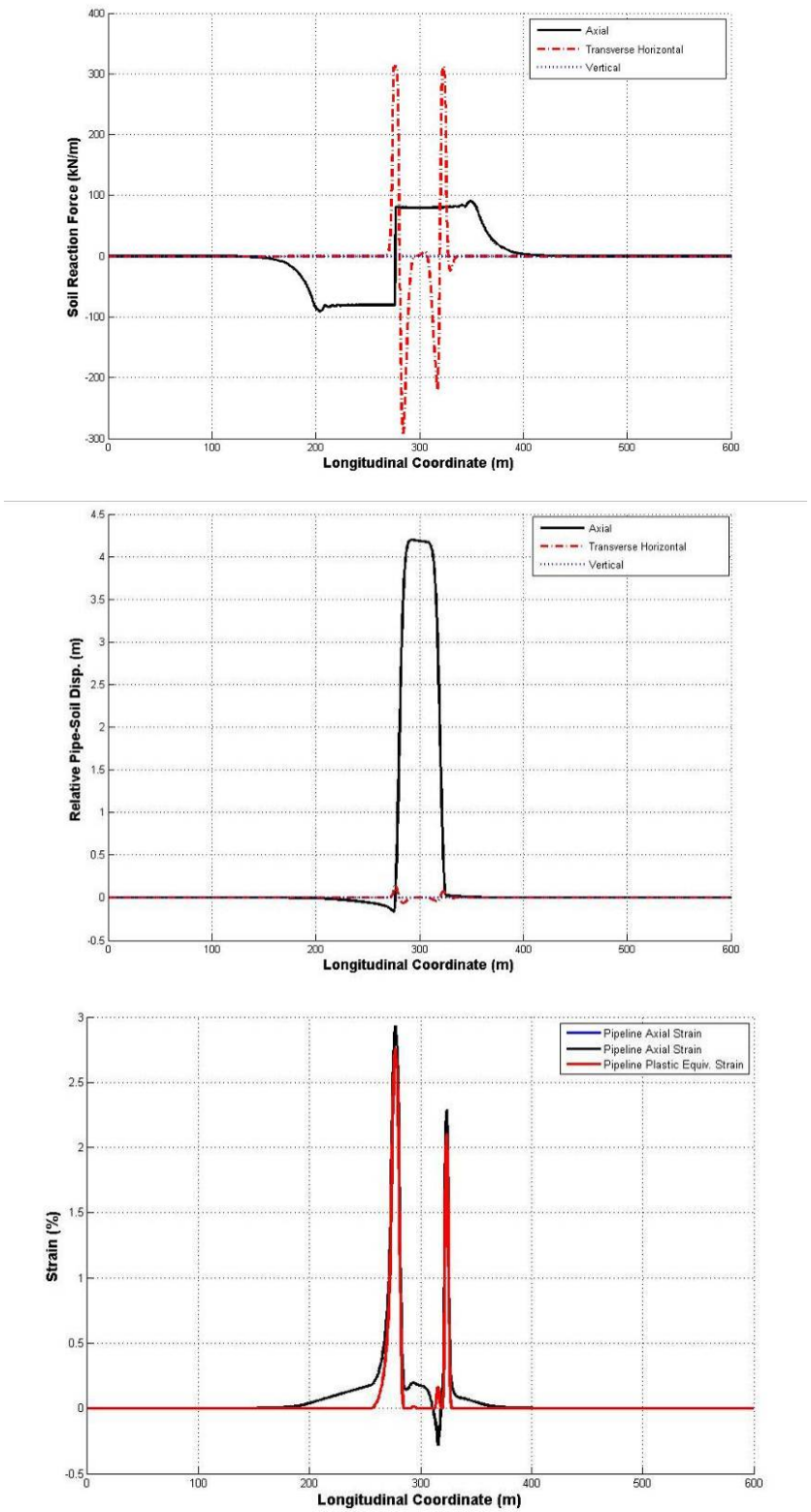

Figure 6-8 Skewed lateral slide pipe-soil response with no interaction effect

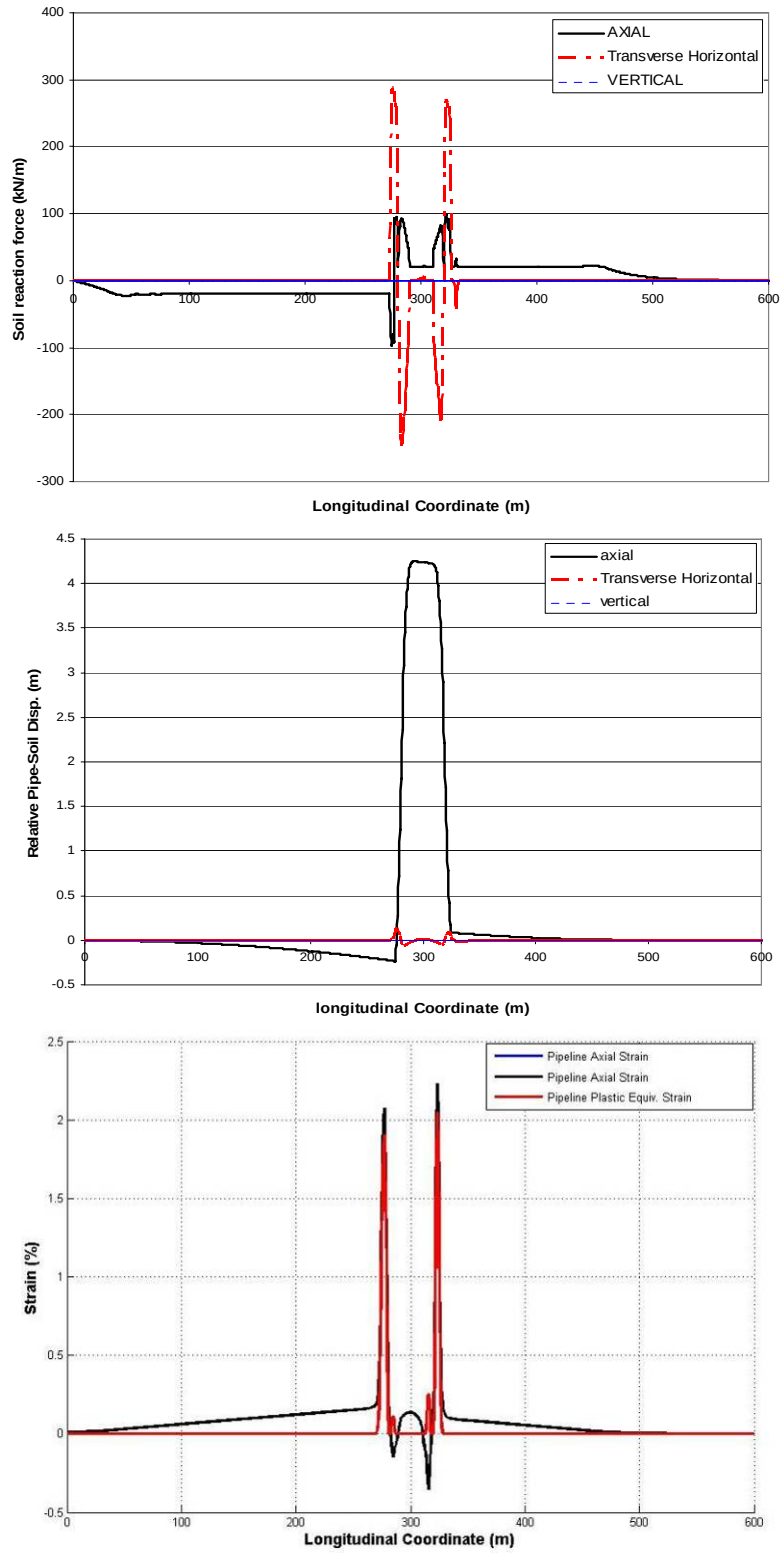

Figure 6-9 Skewed lateral slide pipe-soil response considering the interaction effect

6.1.3 Three dimensional pipeline example

The final example is for 2# 170m X70 pipeline alternatives in sand subject between 68m to 128m length to 5 m lateral and 1.2 m vertical displacements, Figure 6-10, specified by DGHC (2007) with the associated soil reactions in Table 6-2. These soil reactions are compared in Figure 6-11 and Figure 6-12. The axial resistance considering interaction exceeds the specified axial limit value as the effect of the mobilised lateral bearing pressure is not considered when calculating the limit, as shown for example in Table 2-1. The two pipe alternatives are either the NG 32" diameter line with a 0.688" wall thickness and 1436 psi internal pressure, or the NGL 14" diameter line with a 0.25" wall thickness and 1508 psi internal pressure.

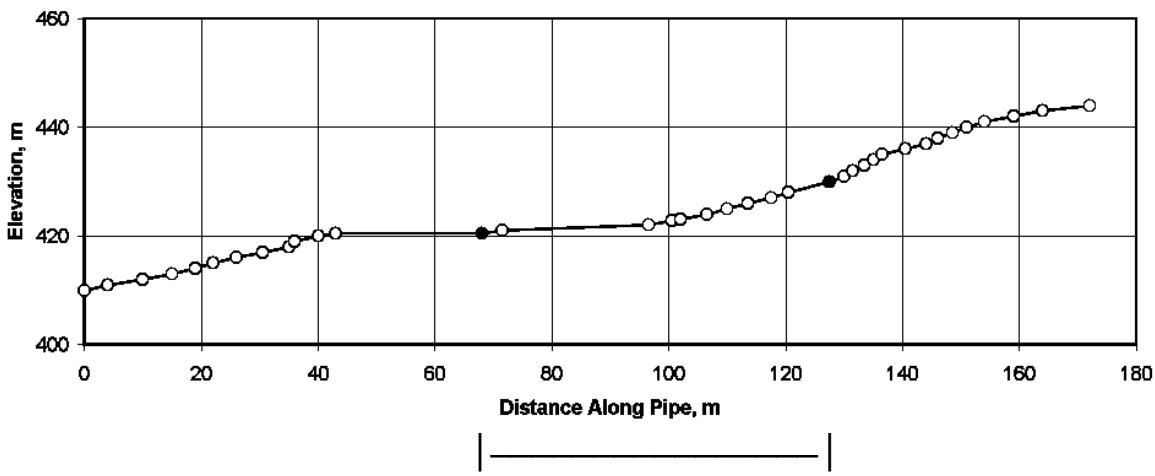

Figure 6-10 Pipeline alternatives subject to lateral and vertical displacement.

Table 6-2 Soil reactions for NG and NGL pipelines

	tu	xu	pu	yu	qu_u	zu_u	qu_d	zu_d
	Axial	D at Axial	Horizontal	D at Horizontal	Uplift	D at Uplift	Bearing	D at Bearing
	kN/m	mm	kN/m	mm	kN/m	mm	kN/m	mm
NG Line	33.0	5.0	185.0	84.0	39.0	26.0	619.0	102.0
NGL Line	22.0	5.0	167.0	98.0	68.0	34.0	360.0	51.0

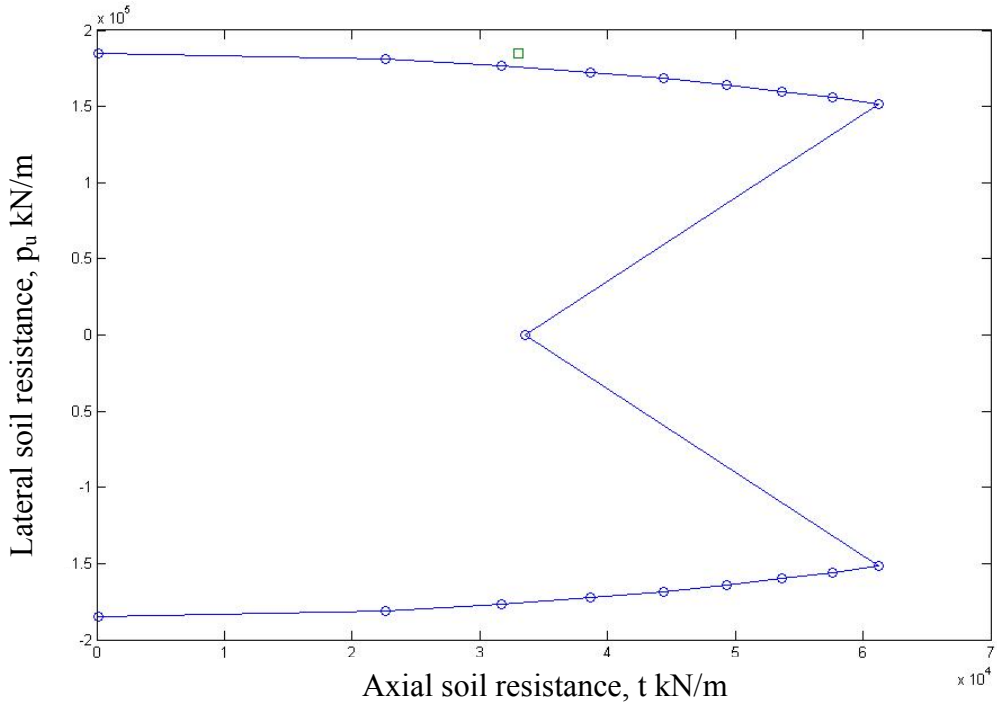

Figure 6-11 NG pipeline soil reaction interaction curve.

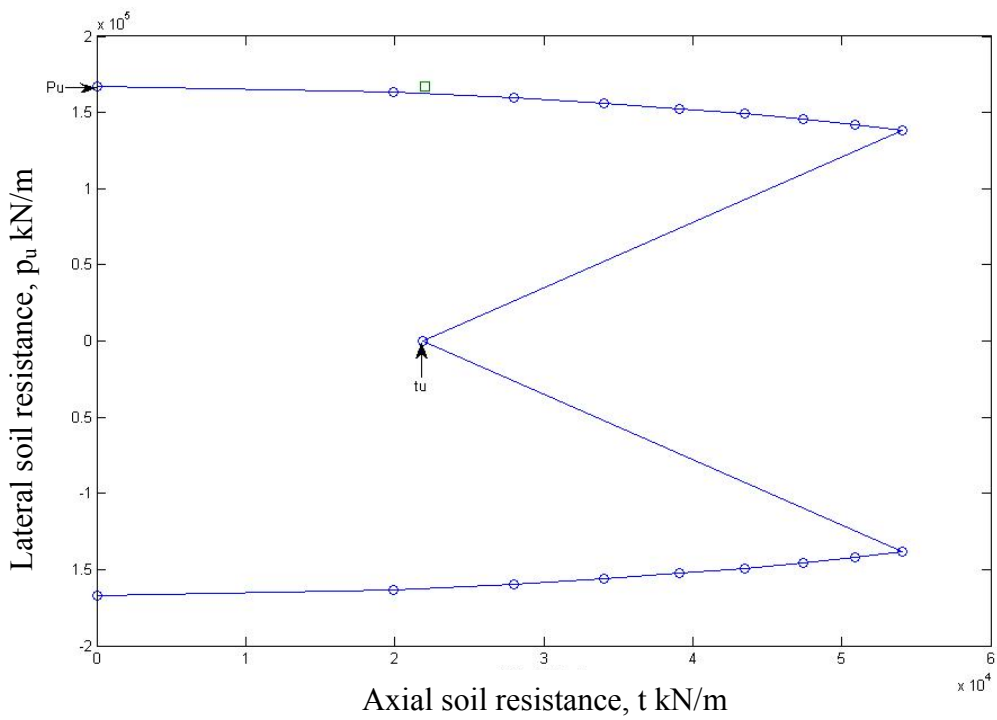

Figure 6-12 NGL pipeline soil reaction interaction curve

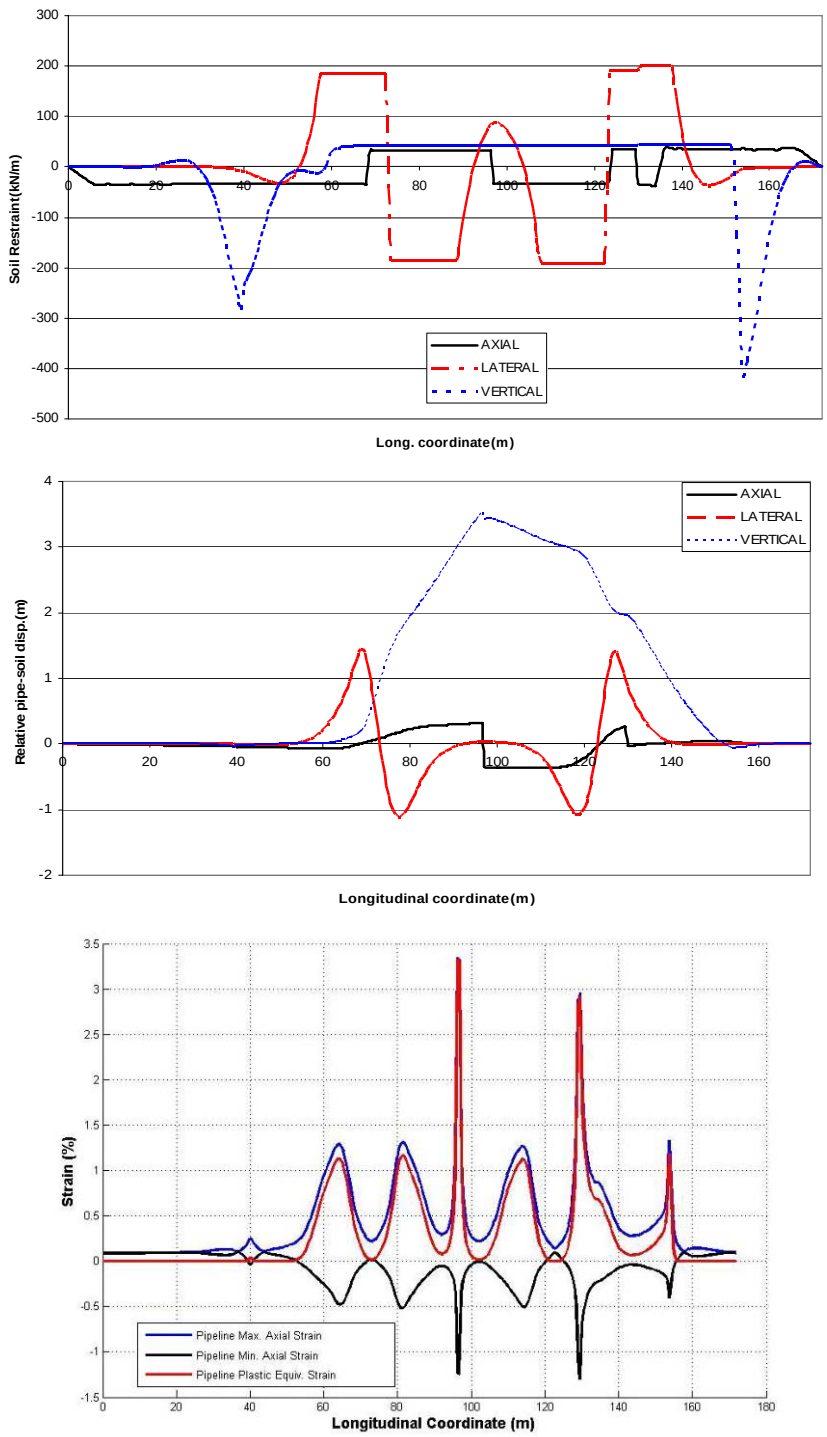

Figure 6-13 NG pipe-soil response in sand with no interaction effect

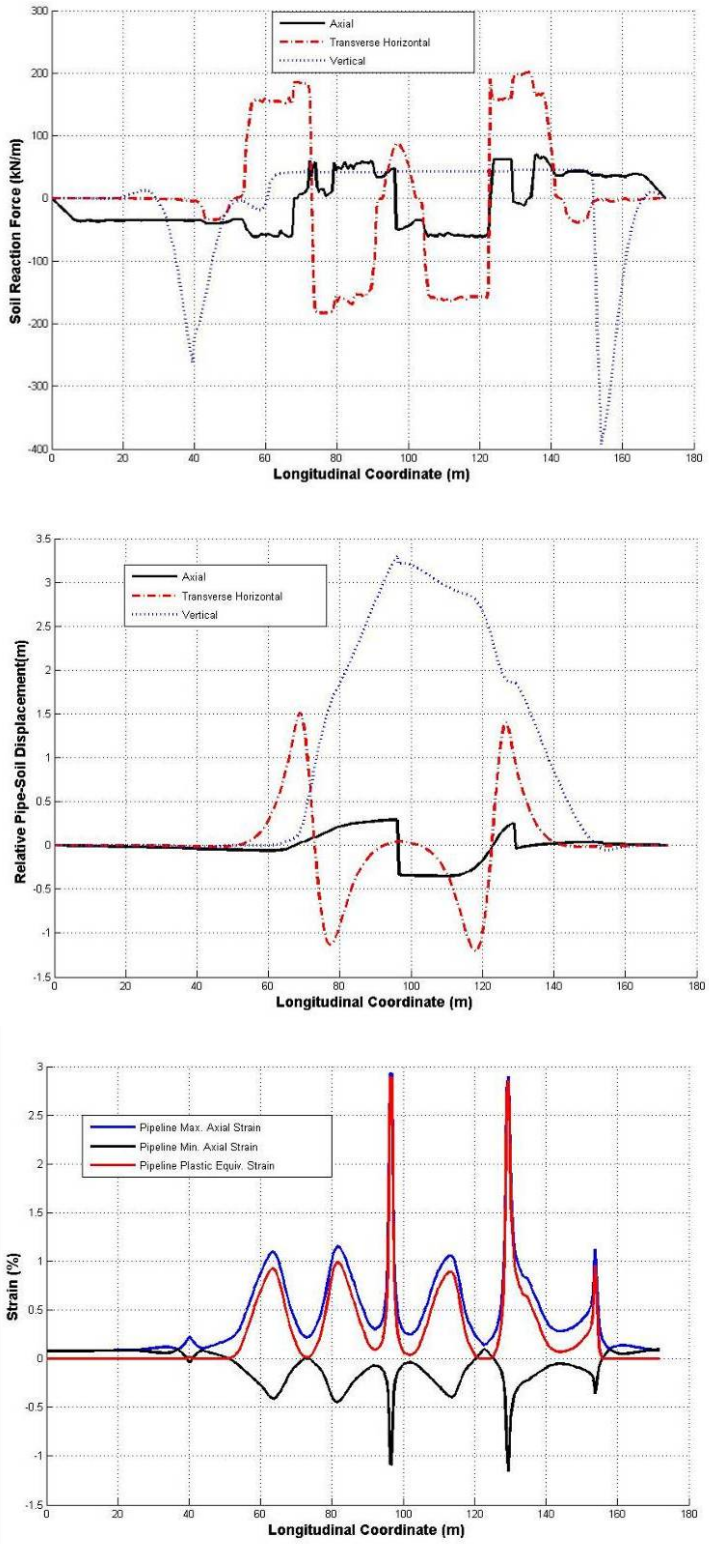

Figure 6-14 NG pipe-soil response in sand considering the interaction effect

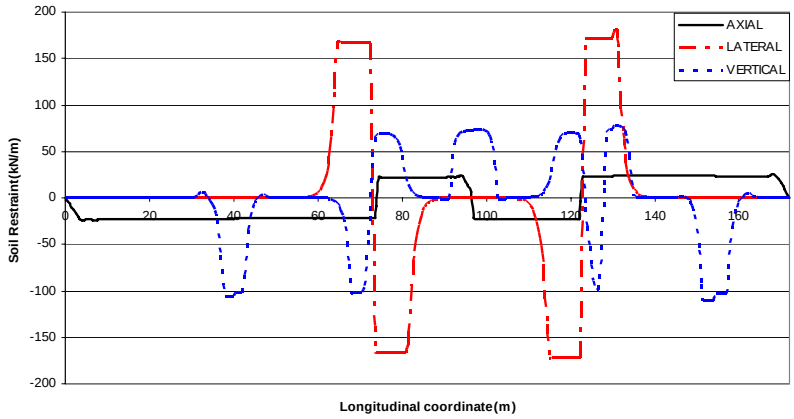

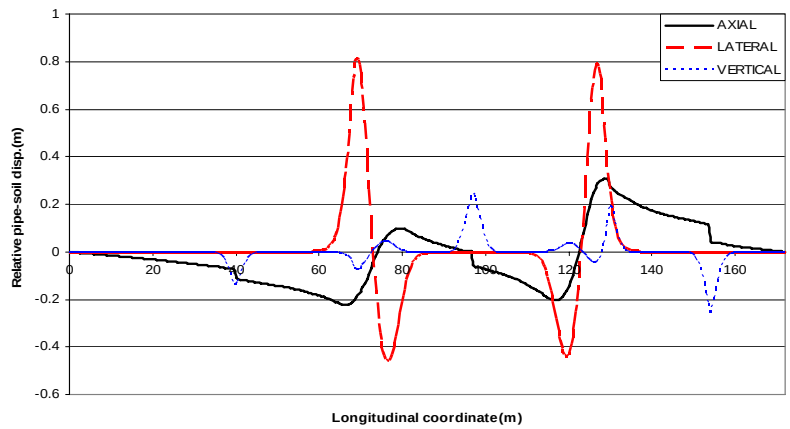

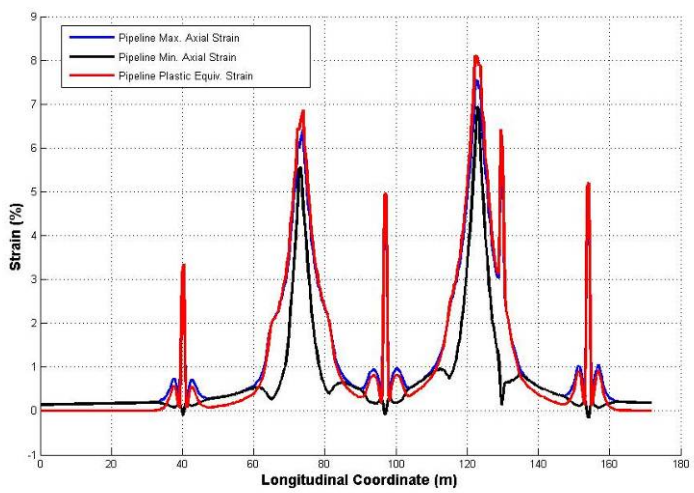

Figure 6-15 NGL pipe-soil response in sand with no interaction effect

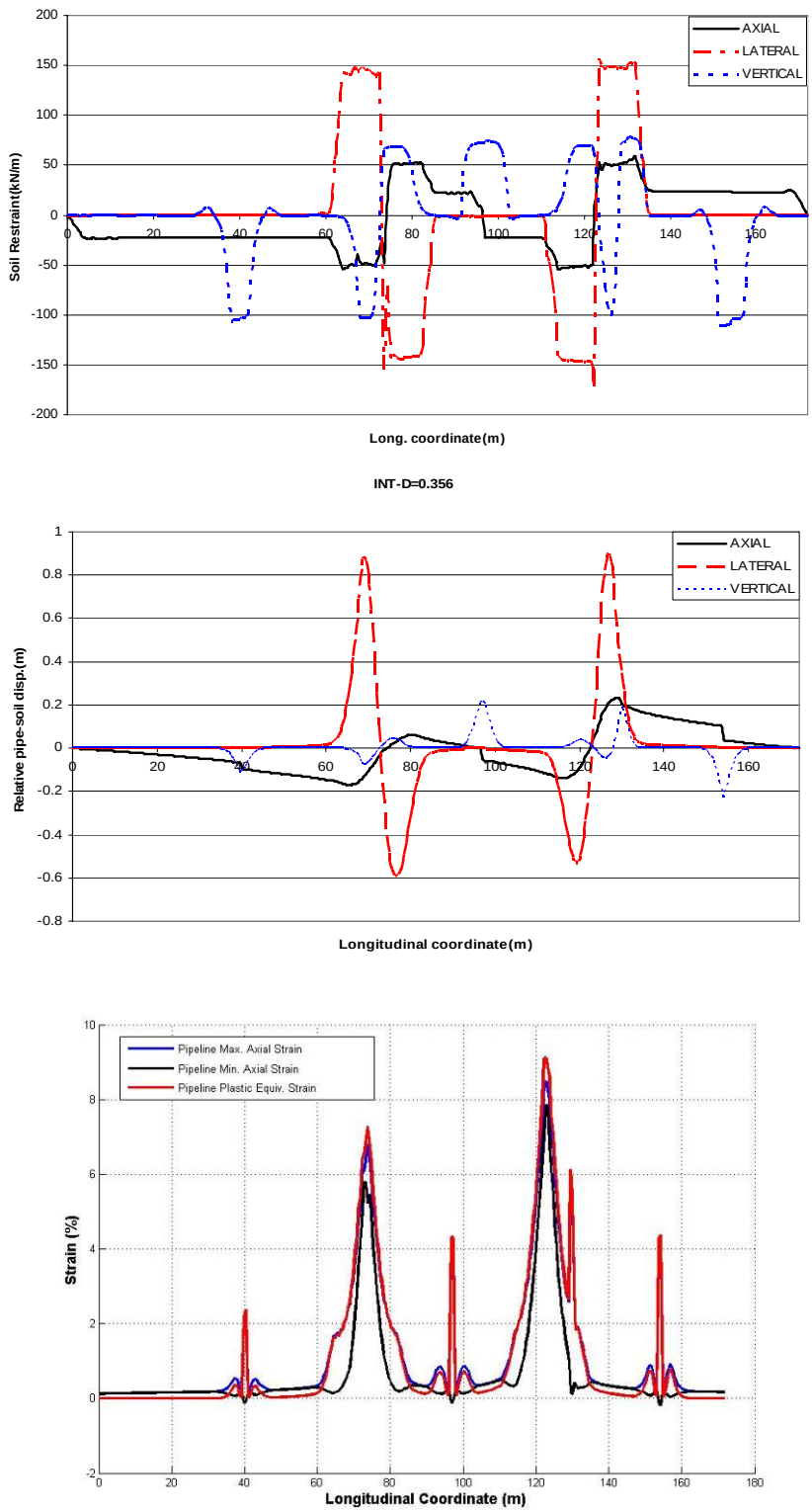

Figure 6-16 NGL pipe-soil response in sand considering the interaction effect

The responses of the NG and NGL pipelines, without and with interaction effects, are shown in Figure 6-13 & Figure 6-14 and Figure 6-15 & Figure 6-16 respectively. These analyses indicate a slight boundary effect on the pipe response, they were rerun considering a much longer pipe length with practically identical results. For the more flexible NGL pipeline, smaller strain peaks are seen at changes in direction around 40m, 95m, 130m and 155m. Larger strain peaks are seen at 65m and 125m associated with the ground displacement transition. For this pipeline, all of the strains at the direction changes are reduced by consideration of the interaction effects. The large plastic strain peaks are slightly increased by interaction consideration. For the NG pipeline, Figure 6-13 & Figure 6-14, the strain peaks are not so apparent due to the spanning effect of the stiffer pipeline. However, all of the strain peaks are reduced by consideration of the interaction effect. The interaction diagrams, Figure 6-11and Figure 6-12, show the axial resistance for interaction to be larger than the prescribed limit value. The peak strain reductions observed from interaction are considered to be due to the slight reduction in lateral resistance when interaction is considered. This strain reduction is considered to be more than offset by the increased axial resistance assessed at the strain peaks at 65m and 125m associated with the ground displacement transition in Figure 6-16.

It is important to account for the interaction between axial and lateral soil resistance in a pipe-soil (beam-spring) structural analysis for aseismic ground movement. The current practice soil spring formulation may over predict pipe bending strains if interaction effects are not considered. In clays, the axial resistance may be controlled by the pipe interface friction and be less than that calculated using the α.Su limit. In sands, the axial frictional resistance can exceed that calculated using the PRCI guideline, due to mobilised lateral bearing pressure contribution to the clamping force. Despite this increase, lower pipe strains from interaction effects may ensue due to the associated reduction in lateral resistance. This strain reduction may be offset by increased axial resistance under some conditions.

6.2 Alternative Pipeline Mechanical Formulation

The pipe formulation offers a second potential alternative to improve current practice in finite element modeling of pipe-soil interaction during ground movement.

An “ELBOW” element is available in ABAQUS 6.7.1, which according to the ABAQUS User’s Manual “are intended to provide accurate modeling of the nonlinear response of initially circular pipes and pipebends when distortion of the cross-section by ovalization

and warping dominates the behavior". This is accomplished using shell theory in the formulation of the element.

The comparative analysis was carried out for quadratic beam and quadratic elbow elements, PIPE32 and ELBOW32 respectively. The simple downslope pipeline conditions of section 6.1.1 without soil interaction effects were adopted.

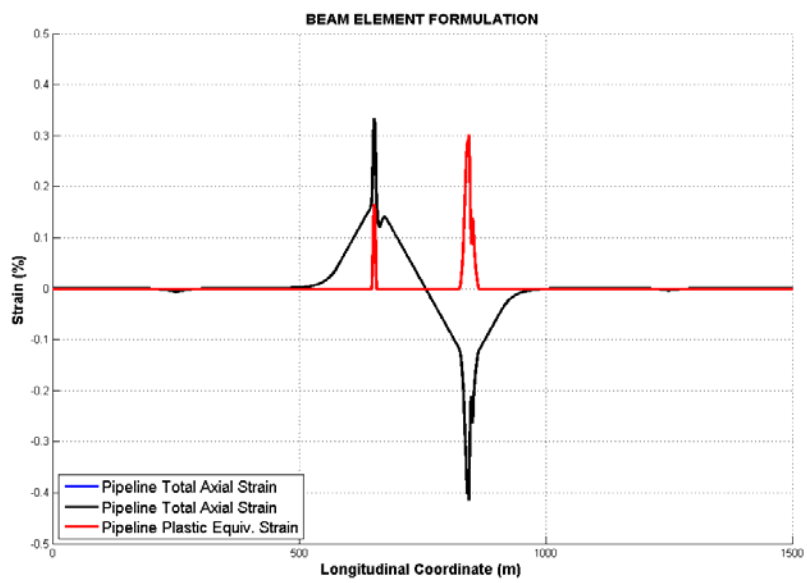

Figure 6-17 Simple downslope pipeline with beam element formulation

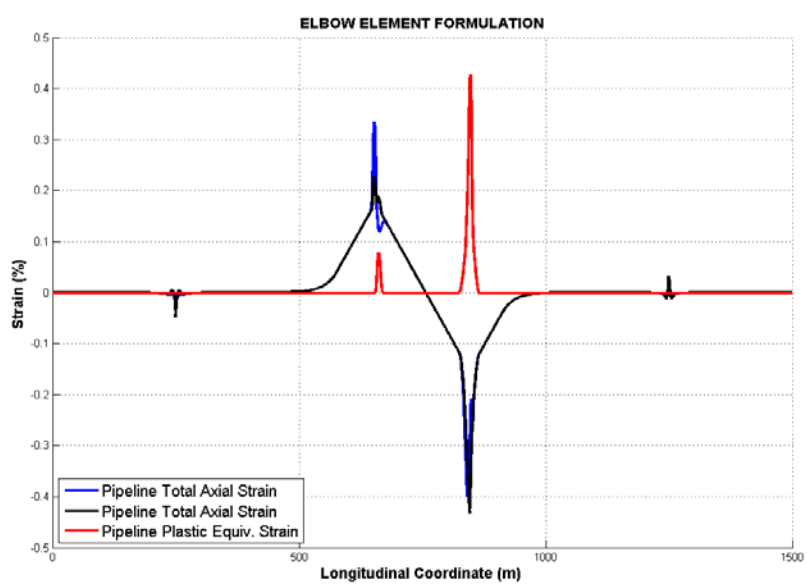

Figure 6-18 Simple downslope pipeline with elbow element formulation

Figure 6-17 and Figure 6-18 illustrate for this particular case that there are only slight differences between the elbow and pipe elements when the first mode of ovalization was used in the elbow element. This may be partially attributed to slight variation in the circumferential position in which the results were taken. The elbow elements therefore offer a viable pipe formulation alternative when distortion of the cross-section by ovalization and warping dominates the pipe behavior.

It is uncertain how the full shell element formulation may behave when connected to a structural spring. It is believed that this effectively creates a point load on one side of the pipe which may cause unrealistic ovalisation of the pipe section.

Continuum shell elements were therefore considered as an improvement to existing finite element models. This allows for a more detailed representation of the pipes behaviour and stress patterns. However, implementation of the soil springs would be very complex as they would have to account for differential pressure circumferentially around the pipe as well as a complex displacement field. This would be in addition to the number of elements required. If this level of detail is required continuum modeling is the only option feasible at the present as demonstrated in the next section.

6.3 Continuum Pipeline/Soil Interaction Analysis

Significant advances with FEA codes and improvements in computer performance in recent years means that full three dimensional continuum FEA of soil-pipe systems are becoming a practical design option. This alternative was investigated to gauge the differences between structural and continuum finite element modeling of pipe-soil interaction under ground movement.

Continuum numerical procedures to model coupled ground movement/pipeline interaction events, within the current limitations of adaptive mesh techniques, should be advanced. A coupled model was developed to analyse the mechanical response of a nominal 559mm (22″) outside diameter pipeline with 25.4mm wall thickness and material grade of 414MPa (X60) to a ground movement event. The pipeline was pressurised to 40MPa and buried with a clearance depth of 0.5m beneath an 8m wide by 2m deep rough rigid indenter in uniform clay conditions with undrained shear strength of 100kPa. Passage of the 15 degree sloped indenter over the pipeline caused significant

ground movement, similar to those induced by slope movement. The effects of these ground movements on the buried pipe were assessed.

The coupled model is illustrated in Figure 6-19. In the continuum model the soil was modelled by linear brick elements with a Von Mises yield criteria and the pipeline was modelled using shell elements with a general contact surface at the interface. The continuum mesh size was insufficient due to computer memory to include the full pipeline anchor length. Structural pipeline/soil spring elements were therefore used to model far-field kinematic effects (e.g. soil resistance and pipeline axial feed-in) during the ground movement event. A reference node defined the connection between the pipeline continuum and structural elements with the assumptions of a plane, non-warping section. The structural-based pipeline/soil interaction modelling procedures are common practice, section 2.6 and details are provided in Kenny et al. (2004).

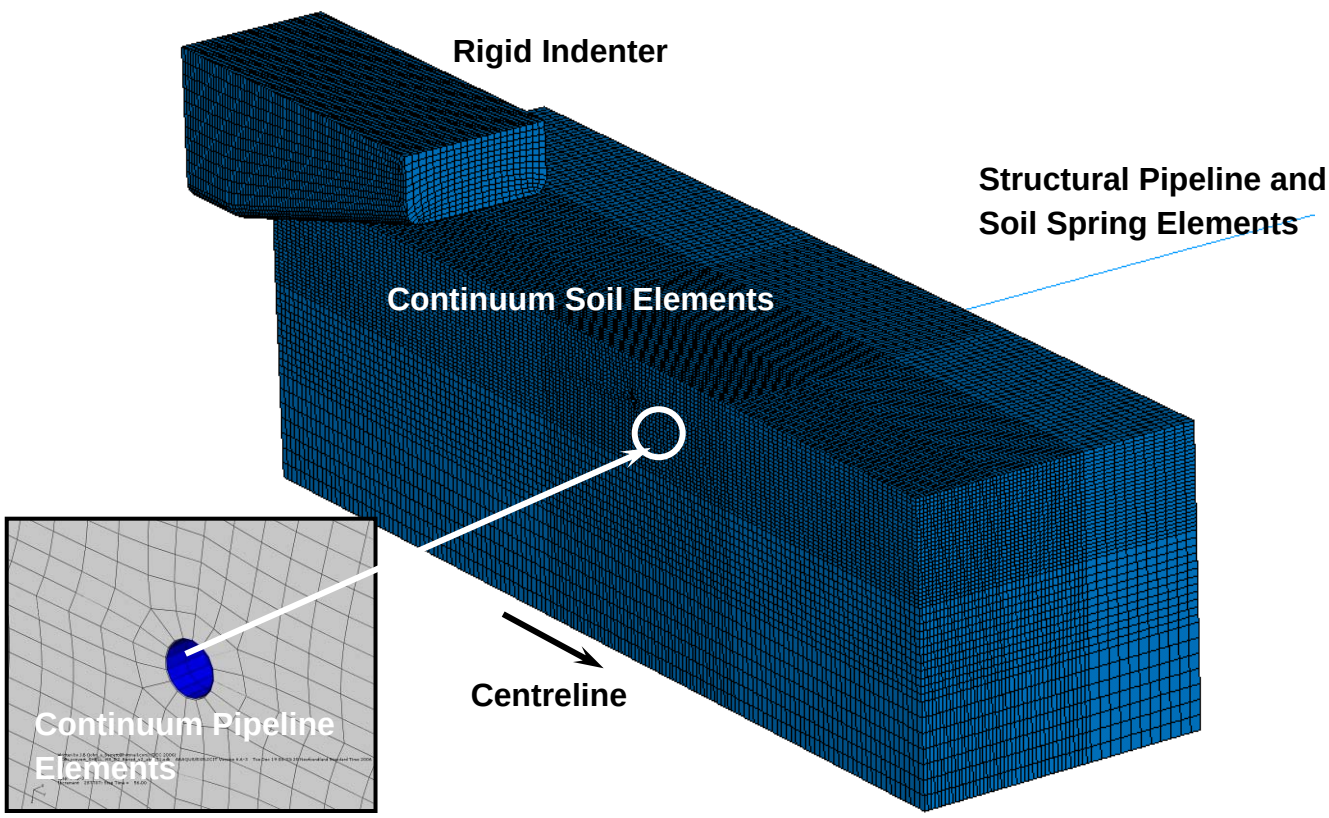

Figure 6-19 Continuum FEA of indenter – soil – buried pipe system

As shown in Figure 6-20, the pipeline has yielded at the indebter centreline and points of curvature inflection. This preliminary analysis illustrates that a fully coupled ground movement/ soil/pipeline interaction model can be successfully implemented.

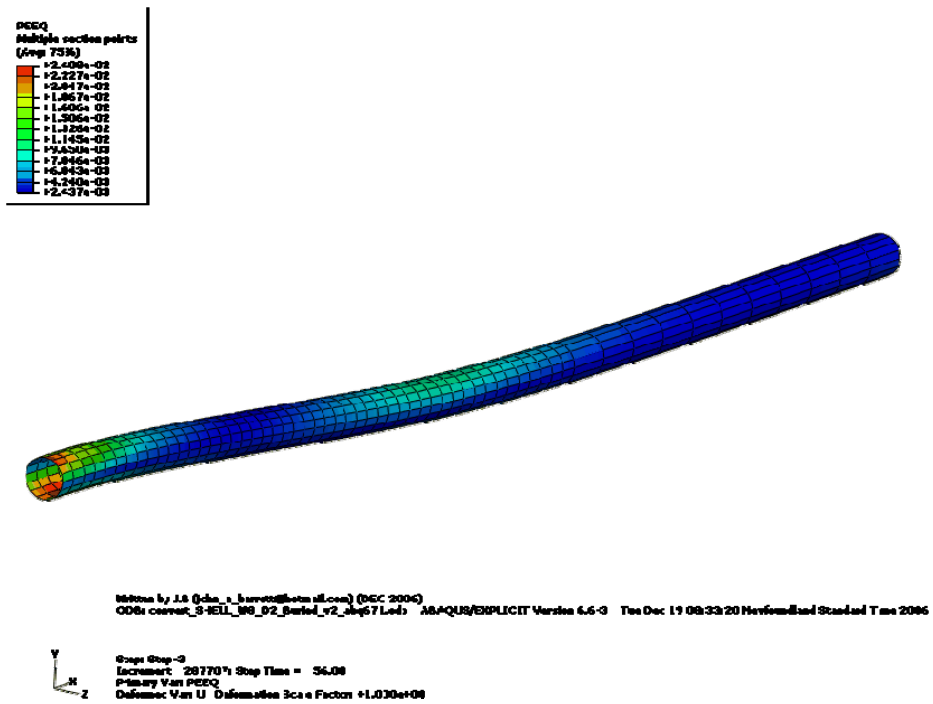

Figure 6-20 Plastic equivalent strain of continuum pipe

The continuum FEA results were compared to those of a typical structural FEA analysis. The structural model consisted of quadratic beam elements (PIPE32) and calibrated structural spring elements (SPRINGA) using the traditional PRCI soil-spring response. The applied ground deformations were imposed based on the continuum FE analysis of the soil in the absence of the pipe, as shown in Figure 6-21.

The deflected pipe shapes in the vertical and horizontal planes are also shown in that figure from the 2 analyses. There is less pipe deflection in the continuum analysis as the full restraint of the soil surrounding the pipe has been simulated, including such effects as shear transfer. This lower deflection results in lower pipe strains, Figure 6-22. The patterns of strain in the pipe are quite similar between the 2 analyses.

Continuum FEA of ground movement effects on buried pipelines do overcome many of the deficiencies recognized in the structural FEA of the same systems, and therefore be more representative of the real situation.

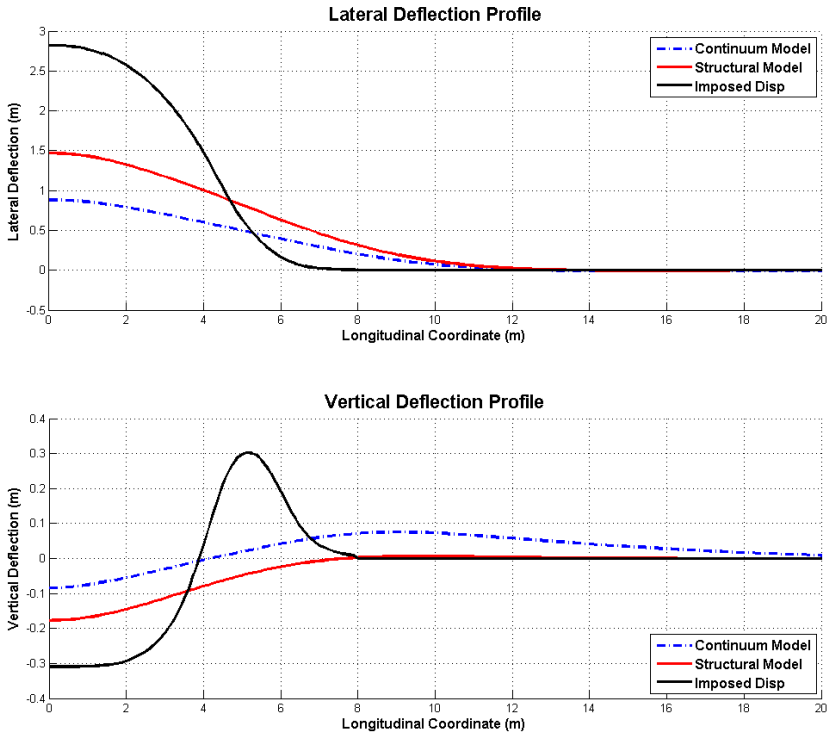

Figure 6-21 Comparison of pipe deflected shape and soil movement

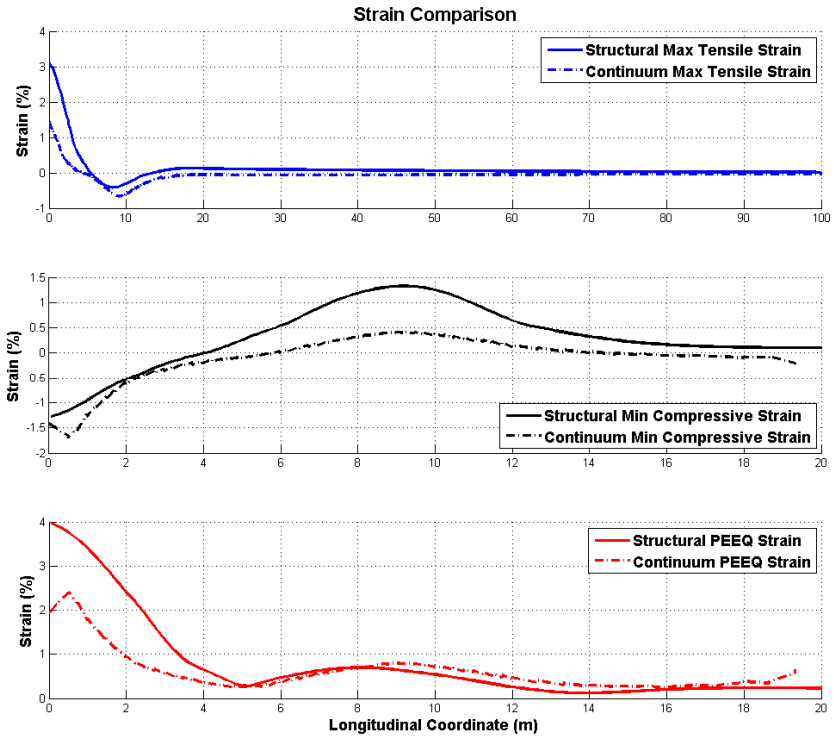

Figure 6-22 Comparison of pipe strains

7 SUMMARY AND CONCLUSIONS

PRCI is leading a program to develop a comprehensive set of guidelines and recommended practices for evaluating pipelines in areas subjected to large-scale ground movements. The 5 main program tasks include definition of large ground displacement hazards, development of pipeline/soil interaction models, improved pipeline response modeling, utilization of pipeline geometry monitoring to assess pipeline condition and, options to mitigate risks of large ground displacement.

This engineering report presents Task 2: Improved Pipeline/Soil Interaction Modeling and Task 3: Improved Pipeline Response Modeling, which are the responsibility of C-CORE. An assessment of INSAR current practice for remote sensing applications under subtask 5.3 of Task 5: Options to Mitigate Risks of Large Ground Displacement, is included in Appendix B.

Current guidelines for pipeline/soil interaction modelling include those prepared for PRCI by Honegger and Nyman (2004). Recent research for lateral buried pipe loading in both sands and clays show that the pipe resistance should be considered as a function of both the soil strength and its weight for shallow to medium burial depths. The resistance is also capped at deeper depths as the failure mechanism localizes around the pipe. The lateral resistance in sand is currently best predicted by the Trautmann and O'Rourke (1985) relationships.

The axial resistance, especially for slow loading rates, results mainly from friction caused by normal effective soil stresses acting around the pipe circumference. These stresses are usually estimated from the initial stresses in the soil, but should also include bearing stresses mobilised by pipe movement in the transverse direction, and consideration of static pore water pressure effects.

Transient pore water pressure effects should be also considered for faster loading rates, such as seismic loading conditions. Very high pore suctions, typically 5 times the total normal stress level, (or true soil adhesion), are required for the axial resistance to be controlled by the undrained strength factored by an adhesion factor, rather than friction at the interface. Recent research has shown that axial resistance does increase with transverse loading.

Soil has a finite shear resistance. Significant research has shown that combined vertical upward and lateral resistances to pipe motion are limited by this finite resistance. This oblique loading effect should be reintroduced into future guideline revisions. There is limited research on the combination of axial and transverse resistance, which is a main focus of this study.

The centrifuge model test simulations and the numerical simulations have independently confirmed the importance of combined axial and lateral soil resistance to pipe motion in soil of finite strength in both dry sand and saturated clay. The physical tests and the analyses gave very similar results in terms of the load resistance of the soil. The deformational response differed partly due to the trench disturbance or similar effects present in the physical models.

The pure lateral or axial resistances assessed from the simulations were consistent with those expected from the guidelines proposed by C-CORE (2003) which included self weight effects in clay and appropriate bearing factors for sand. The oblique loading conditions produced an interaction envelope under axial and lateral load comprised of 2 different failure criteria. For low load angles less than about 10°, the criterion is sliding along the interface between the pipe and soil. For larger angles, after a transition, the second criterion is shear failure through the soil mass.

The physical tests in sand and clay showed the axial resistance under interface sliding to be controlled by the pipe interface friction, when the vertical loads acting on the pipe were also included. The clay tests also showed the mitigating effects of pore pressure generation from the mobilised lateral bearing pressure for the soil conditions considered. The numerical simulations confirmed that very high pore water suctions would be required for the sliding mode to be controlled by the clays undrained strength.

The shear failure criterion was found to be well approximated in sand and clay using a Von Mises type failure criterion to account for pipe bearing stress from lateral load combined with pipe shear stress induced from the axial load. The interaction envelope was defined by monotonic oblique pipe displacement. Numerical simulations in clay confirmed that this envelope was also appropriate to account for resistance changes associated with changes in load direction.

The lateral load mobilization with the lateral displacement component followed practically the same backbone ‘elastic’ curve before peak load in both the sand and clay

tests. The lateral, 60 and 20 degree tests peak at decreasing lower load levels as increasingly more strength capacity is mobilised in the axial direction.

Three worked examples showed effects of the interaction between axial and lateral soil resistance in pipe-soil (beam-spring) structural analysis for aseismic ground movement. The current practice soil spring formulation generally predicted higher pipe bending strains when interaction effects were not considered. In clays, the axial resistance may be controlled by the pipe interface friction and be less than that calculated using the adhesion limit. In sands, the axial frictional resistance can exceed that calculated using the PRCI guideline, due to mobilised lateral bearing pressure contribution to the clamping force. Despite this increase, lower pipe strains from interaction effects may ensue due to the associated reduction in lateral resistance through consideration of the finite strength. This strain reduction may be offset by increased axial resistance under some conditions.

The pipe beam formulation will not accommodate localized section changes, as pipeline performance limits permit higher bending strains and more ovalisation. Higher order ‘elbow’ elements have been shown to be a viable alternative formulation when distortion of the cross-section by ovalization and warping dominates the pipe behavior.

Consideration of interaction effects between adjacent soil springs is not required when the soil is modeled as a continuum. This study has demonstrated that continuum finite element modelling is a viable alternative to structural modelling for detailed consideration of short pipe section subject to ground movement. The structural model is adopted to simulate the pipe anchor lengths outside of the ground movement area.

8 REFERENCES

Akinmusuru, J. O. (1978). "Horizontally loaded vertical plate anchors in sand." J. Geotech. Eng. Div., Am. Soc. Civ. Eng., 104~2!, 283–286.

ALA (2001) Guideline for the Design of Buried Steel Pipe - July 2001, American Lifelines Alliance.

Altaee, A., Fellenius, B.H. and Salem, H. (1996). Finite element modelling of lateral pipeline-soil interaction. Proceedings, 15th Offshore Mechanics and Arctic Engineering, OMAE, Houston, TX, USA, vol. 5, Pipeline Technology, pp.333-341.

ASCE (1984). Guidelines for the Seismic Design of Oil and Gas Pipeline Systems. American Society of Civil Engineers, Committee on Gas and Liquid Fuel Lifelines, Technical Council on Lifeline Earthquake Engineering, ASCE, New York.

Audibert, J.M.E., and Nyman, K.J. (1977). Soil restraint against horizontal motion of pipes. Journal of the Geotechnical Engineering Division, ASCE, 103(10), 1119-1142.

Bolton, M.D., Gui, M.W. and Phillips, R. (1993) Review of miniature soil probes for model tests. Proceedings of 11th South East Asian Geotechnical Conference, Singapore, May 1993.

Bruschi, R., Monti, P., Bolzoni, G., and Tagliaferri, R. (1995). Finite element method as numerical laboratory for analysing pipeline response under internal pressure, axial load, bending moment. Proceedings, 14th Offshore Mechanics and Arctic Engineering, OMAE, Houston, TX, USA, vol. 5, Pipeline Technology, pp.389-401.

Bruschi, R., Glavina, S., Spinazze, M., Tomassini, D., Bonanni, S., and Cuscuna, S. (1996). Pipelines subject to Slow Landslide Movements: Structural Modelling vs Field Measurement. Proceedings, 15th Offshore Mechanics and Arctic Engineering, OMAE, Houston, TX, USA, vol. 5, Pipeline Technology, pp.343-353.

Cappelletto, A., Tagliaferri, R., Giurlani, G., Andrei, G., Furlani, G., and Scarpelli, G. (1998). Field full scale tests on longitudinal pipeline-soil interaction. Proceedings of International Pipeline Conference 1998, Calgary, vol. 2, pp.771-778.

Cathie D.N., Jaeck, C., Ballard, J.C., and Wintgens, J.F. (2005). Pipeline Geotechnics-State of the Art. Proceedings of International Symposium on Frontiers in Offshore Geotechnics ISFOG 19 – 21 September 2005, Perth, Western, Australia.

C-CORE (1998). Large scale modelling of soil/pipe interaction under moment loading – Laboratory testing report. Contract Report for Geological Survey of Canada, C-CORE Publication 98-C23.

C-CORE (2003). Extended model for Pipe Soil Interaction. Final report prepared for Pipeline Research Council International, C-CORE Report R-02-044-113, August 2003.

Cocchetti G., C. di Prisco, A. and Galli W. (2007) Soil-pipeline interaction along active fault systems. 16th Int Offshore and Polar Eng Conf, Lisbon, Portugal, July 1-6, 2007

Das, B.M. (1985). Resistance of Shallow Inclined Anchors in Clay. Proceedings, Uplift Behavior of Anchor Foundations in Soil, ASCE, pp. 86-101.

De Beer, E. E., (1970), "Experimental Determination of Shape Factor and Bearing Capacity Factors of Sand," Geotechnique, Vol. 20, No. 4, 387-411.

DGHC (2007) Example Ground Movement Cases. Email to C-CORE of 20 August 2007.

Dickin, E. A., and Leung, C. F. (1983). "Centrifugal model tests on vertical anchor plates." J. Geotech. Eng., 109(12), 1503–1525.

Dickin, E.A. (1988). Stress-displacement of buried plates and pipes. Centrifuge 88 - Proceedings of the International Conference on Geotechnical Centrifuge Modelling, J.F. Corté (ed.), A.A. Balkema, Rotterdam, pp.205-214.

Finch, M 1999. Upheaval buckling and floatation of rigid pipelines: The influence of recent geotechnical research on the current state of the art. Offshore Technology Conference, OTC10713.

Finch, M., Fisher, R., Palmer, A. & Baumgard, A. 2000. An integrated approach to pipeline burial in the 21st century. Proc. Deep Offshore Technology 2000.

Guo, P. (2005). Numerical Modeling of pipe-soil Interaction under Oblique Loading. Journal of Geotechnical and Geoenvironmental Engineering, ASCE, 131(2): 260-268.

Guo, P., and Stolle, D.FE. (2005). Lateral Pipe-Soil Interaction in Sand with Reference to Scale Effect. Journal of Geotechnical and Geoenvironmental Engineering, ASCE, 131(3): 338-349.

Hansen, J.B. (1961). The ultimate resistance of rigid piles against transversal forces. Bulletin 12, Danish Geotechnical Institute, Copenhagen, Denmark, pp.5-9.

Honegger, D.G. (1999). Field measurement of axial soil friction forces on buried pipelines. Proceedings of the Fifth U.S. Conference on Lifeline Earthquake Engineering, Technical Council on Lifeline Earthquake Engineering, Monograph No. 16, American Society of Civil Engineering.

Honegger, D.G., and Nyman, J. (2001). Manual for the Seismic Design and Assessment of Natural Gas Transmission Pipelines. Pipeline Research Council International Project PR-268-9823.

Honegger, D.G., and Nyman, J. (2004). Guidelines for the Seismic Design and Assessment of Natural Gas and Liquid Hydrocarbon. Pipelines Pipeline Research Council International Project PR-268-9823.

Honegger, D.G., Weijewickreme, D, and Karimian, H. (2006). Assessment of Geosynthetic Fabrics to Reduce Soil Loads on Buried Pipelines. Pipeline Research Council International Project PR-268-03111.

Hsu, T.W. (1996). Soil Restraint against Oblique Motion of Pipelines in Sand. Canadian Geotechnical Journal, 33: 180-188.

Hsu, T.W., Chen, Y.J., and Wu, C.Y. (2001). Soil Friction Resistance of Oblique Pipelines in Loose Sand. Journal of Transportation Engineering, ASCE, 127(1): 82-87.

Hsu, T.W., Chen, Y.J., and Hung, W.Y. (2006). Soil Restraint to Oblique Movement of Buried Pipes in Dense Sand. Journal of Transportation Engineering, ASCE, 132(2): 175-181.

Itasca Consulting Group Inc. (2000). FLAC, version 4.0. Itasca Consulting Group Inc., Minneapolis, Minn.

Jefferies, M.G. (1993). Nor–Sand: A simple critical state model for sand. Geotechnique, 43(1): 91–103.

Karimian, S.A. (2006). Response of Buried Steel Pipelines subjected to Longitudinal and Transverse Ground Movement. A draft Ph.D. thesis, University of British Colombia, Vancouver, Canada.

Kennedy RP, Chow AW and Williamson RA (1977) Fault movement effects on buried oil pipeline. P617-633. ASCE Transportation Engineering Journal.

Kenny, S., Bruce, J., King, T., McKenna, R., Nobahar, A. and Phillips, R. (2004). "Probabilistic design methodology to mitigate ice gouge hazards for offshore pipelines." Proc., IPC'04, Paper No. IPC04-0527, 9p.

Kim, H-S., Kim, W-S., Bang, I-W., and Oh, K.H. (1998). Analysis of stresses on buried natural gas pipeline subjected to ground subsidence. Proceedings, International Pipeline Conference, vol. 2, Calgary, AB, Canada, pp.749-756.

Krstelj, I. (1996). Behaviour of laterally loaded pipes in dry and saturated sand (centrifuge testing). Ph.D. thesis, Princeton University.

Kulhawy, F.H.C., Trautmann, C.H., Beech, J.F., O'Rourke, T.D., and McGuire, W. (1983). Transmission line structure foundations for uplift-compression loading. Report No. EL-2870, Electric Power Research Institute.

Machan, G., and Squier, L.R. (1983). Bitumen coating on piles to reduce downdrag. Public Roads, vol. 46, No. 4, pp.142-151.

Mackenzie, T.R. (1955). Strength of Deadman anchors in clay. M.Sc. Thesis, Princeton University, Princeton, USA.

Martin, C. M., and Houlsby, G.T. (2001). Combined loading of spudcan foundations on clay: Numerical modelling. Geotechnique, 51(8):687–699.

Merifield, R.S., Sloan, S.W. & Yu, H.S. 2001. Stability of plate anchors in undrained clay. Geotechnique 51(2): 141- 153.

Meyerhof, G.G. (1955). Influence of roughness of base and ground-water conditions on the ultimate bearing capacity of foundations. Geotechnique, vol. 5, pp.227-241.

Meyerhof, G. G. (1963). Some recent research on the bearing capacity of foundations. Canadian Geotechnical Journal, 1(1):16-26.

Meyerhof, G.G. (1973). Uplift resistance of inclined anchors and piles. Proceedings, 8th International Conference on Soil Mechanics and Foundation Engineering, Moscow, Vol. 2, pp. 167-172.

Murff, J.D. (1996). The geotechnical centrifuge in offshore engineering. OTRC Honors Lecturer, Proc. Offshore Technology Conference, Houston, Texas.

Neely, W. J., Stuart, J. G., and Graham, J. (1973). "Failure loads of vertical anchor plates in sand." J. Soil Mech. Found. Div., 99(9), 669–685.

Nyman, K. J. (1982). Soil response against the horizontal-vertical motion of pipes. Preprint 82-534, Presented at Proceedings of ASCE National Convention, New Orleans.

NEN 3650 Nederlandse Norm (1991). Eisen voor Stalen Transportleidingsystemen (Requirements for Steel Pipeline Transportation Systems). Publikatie Uitsluitend ter Kritiek.

O'Rourke, M.J., and Liu, X. (1999). Response of buried pipelines subjected to earthquake effects. Monograph Series, MCEER.

O'Rourke, T.D., Wang, Y., and Shi, P. (2004). Advances in Lifeline Earthquake Engineering. Proceedings of the 13WCEE, Vancouver, Canada, Paper No. 5033.

Ovesen, N. K. (1964). "Anchor slabs, calculation methods, and model tests." Bulletin No. 16, The Danish Geotechnical Institute, Copenhagen.

Paulin, M.J. (1998). An investigation into pipelines subjected to lateral soil loading. Ph.D. Thesis, Memorial University of Newfoundland, St. John's, Canada.

Paulin, M.J., Phillips, R., and Boivin, R. (1995). Centrifuge modelling of lateral pipeline/soil interaction - Phase II. International Conference on Offshore Mechanics & Arctic Engineering, Copenhagen, June 1995, vol. V, pp 107-123.

Paulin, M.J., Phillips, R., and Boivin, R. (1996). An experimental investigation intolateral pipeline interaction. International Conference on Offshore Mechanics &Arctic Engineering, Florence, June 1996, vol. V, pp 313-323.

Paulin, M.J., Phillips, R., Clark, J.I., Hurley, S., and Trigg, A. (1997). Establishment of a full-scale pipeline/soil interaction test facility and results lateral and axial investigations in sand. Proceedings, 16th International Conference on Offshore and Arctic Engineering (ASME - OMAE 1997), vol. 5, pp.139-246.

Paulin, M.J., Phillips, R., Clark, J.I., and Boivin, R. (1998a). An experimental investigation into lateral pipeline/soil interaction - phase II. Centrifuge 98 -

Proceedings of the International Conference Centrifuge 98, A.A. Balkema, Rotterdam, in press.

Paulin, M.J., Phillips, R., Clark, J.I., Trigg, A., and Konuk, I. (1998b). A full-scale investigation into pipeline/soil interaction. Proceedings of 1998 International Pipeline Conference, ASME, Calgary, AB, June 1998, vol. 2 pp. 779-787.

Phillips, R., Nobahar, A., and Zhou, J. (2004a). Trench Effects in Pipe-Soil Interaction. Proceedings of IPC2004, International Pipeline Conference, Alberta, Canada.

Phillips, R., Nobahar, A., and Zhou, J. (2004b) Combined Axial And Lateral Pipe-Soil Interaction Relationships. Proc IPC2004, Intl Pipeline Conf, Alberta, Canada.

Popescu, R. (1999). Finite element analysis of pipe/soil interaction phase 1 - two-dimensional plane strain analyses. Contract Report for the Geological Survey of Canada. C-CORE Publication 99-C23, June.

Popescu, R., and Konuk, I. (2001). 3D finite element analysis of rigid pipe interaction with clay. Proceedings of 10th International Conference on Computer Methods and Advances in Geomechanics, Tucson, AZ, vol. 2, pp. 1203-1208.

Popescu, R., Guo, P., and Nobahar, A. (2001). 3D Finite Element Analysis of Pipe/Soil Interaction. Final Report for Geological Survey of Canada, Chevron Corp. and Petro Canada, C-CORE Contract Report 01-C8.

Popescu, R., Phillips, R., Konuk, I., and Deacu, D. (1999). Numerical and Physical Analysis of Pipe-Soil Interaction, Proceedings, 52nd Canadian Geotechnical Conference, Regina, Sask., pp.437-444.

Rizkalla, M., Trigg, A., and Simmonds, G. (1996). Recent Advances in the Modeling of Longitudinal Pipeline/Soil Interaction for Cohesive Soils, Proceedings of the 15th International Conference on Offshore Mechanics and Arctic Engineering, vol. V, pp. 325-332.

Rowe, R.K., and Davis, E.H. (1982a). The Behaviour of Anchor Plates in Clay. Geotechnique, 32(1), 9-23.

Rowe, R.K., and Davis, E.H. (1982b). The Behaviour of Anchor Plates in Sand. Geotechnique, 32(1), 25-41.

Scarpelli, G., Sakellariadi, E., and Furlani, G. (1999). Longitudinal Pipeline-Soil Interaction: Results from Field Full Scale and Laboratory Testing. In Geotechnical Engineering for Transportation Infrastructure, p511, Barends et al. (eds), Balkema, Rotterdam, ISBN 90 5809 0477. (also 12th ECSMGE, 1999).

Schofield A.N. (1980). Cambridge geotechnical centrifuge operations. Geotechnique 20, 227-268.Murff (1996).

Sladen, J.A. (1992). The Adhesion Factor: Application and Limitations. Canadian Geotechnical Journal, 29, 326-333.

Smith, J. E. (1962). "Deadman anchorages in sand." Tech. Rep. R-199, U.S. Naval Civil Engineering Laboratory, Port Hueneme, Calif.

Stroud, M.A (1971) Sand under low stress levels in simple shear apparatus. PhD thesis. Cambridge University.

Tomlinson, M.J., (1957). The Adhesion of Piles Driven in Clay Soils, Proceedings, Fourth International Conference on Soil Mechanics and Foundation Engineering, London, England, Vol. 2, pp. 66-71.

Trautmann, C.H., and O'Rourke, T.D. (1983). Behaviour of pipe in dry sand under lateral and uplift loading. Geotechnical Engineering Report 83-6, Cornell University, Ithaca, New York.

Trautmann, C. H., and O'Rourke, T. D. (1985). "Lateral force displacement response of buried pipe." J. Geotech. Eng., 111(9), 1077–1092.

Turner, J.E. (2004). Lateral Force-displacement Behavior of Pipes in Partially Saturated Sand. M.Sc. thesis, Cornell University.

Vanden Berghe, J-F, Cathie, D. & Ballard, J.-C. (2005) Pipeline uplift mechanisms using finite element analysis, Int. Conf. Soil Mech. Foundation Eng., Osaka.

Vesic, A.S. (1971). Breakout resistance of objects embedded in ocean bottom. Journal of the Soil Mechanics and Foundations Division, ASCE, 97(9), 1183-1205.

Yimsiri, S., Soga, K., Yoshizaki, K., Dasari, G.R., and O'Rourke, T.D. (2004) Lateral and Upward Soil-Pipeline Interactions in Sand for Deep Embedment Conditions. Journal of Geotechnical and Geoenvironmental Engineering, 130(8): 830-842.

9 APPENDIX A : ABAQUS/STANDARD IMPLEMENTATION

9.1 Hardening/Softening

The implementation procedure of hardening law in ABAQU/STANDARD used section 4.5 in this study is shown in Figure 9-1. Subroutine USDFLD (Figure 9-2) was used along with the following portion of data file (Figure 9-2) to account for changes in the material yield conditions based on the plastic strain magnitude. Details regarding the meaning of each line are available in ABAQUS documentation. Other constitutive parameters can also be updated using subroutine USDFLD. For instance, the dependence of soil elastic modulus on the effective mean normal stress level is considered using the same implementation procedure in section 4.6.

```
** MATERIALS
**
*Material, name=PIPE
*Elastic
 2e+08, 0.3
*Material, name=SOIL
*Elastic
8000., 0.4
*USER DEFINED FIELD
*DEPVAR
1
****Dependence of friction and dilation angles on the plastic strain level
*MOHR COULOMB, DEPENDENCIES = 1
37.5,2.4,0,0.0000
39.0,4.3,0,0.0014
41.2,7.2,0,0.0050
42.3,8.6,0,0.0088
43.5,10.3,0,0.0162
43.7,10.6,0,0.0245
42.3,8.7,0,0.0338
39.3,4.7,0,0.0527
37.2,2.1,0,0.0707
36.1,0.7,0,0.0969
35.6,0.0,0,0.1434
35.3,0.0,1,0.3877
35.3,0.0,2,1.1125
35.3,0.0,3,1.4164
35.3,0.0,0,10.0
****Dependence of cohesion on the plastic strain level is neglected
*MOHR COULOMB HARDENING
5.0,0
**
```

Figure 9-1 Implemention of hardening law in ABAQUS/STANDARD.

```
      SUBROUTINE USDFLD(FIELD,STATEV,PNEWDT,DIRECT,T,CELENT,
     1 TIME,DTIME,CMNAME,ORNAME,NFIELD,NSTATV,NOEL,NPT,LAYER,
     2 KSPT,KSTEP,KINC,NDI,NSHR,COORD,JMAC,JMATYP,MATLAYO,
     3 LACCFLA)
C
      INCLUDE 'ABA_PARAM.INC'
C
      CHARACTER*80 CMNAME,ORNAME
      CHARACTER*3  FLGRAY(15)
      DIMENSION FIELD(NFIELD),STATEV(NSTATV),DIRECT(3,3),
     1 T(3,3),TIME(2)
      DIMENSION ARRAY(15),JARRAY(15),JMAC(*),JMATYP(*),
     1 COORD(*)
C
C
C               GET EQUIVALENT PLASTIC STRAIN
      CALL GETVRM('PE',ARRAY,JARRAY,FLGRAY,JRCD,JMAC,JMATYP,MATLAYO,
     2 LACCFLA)
      PEMAG = ARRAY(8)
      FIELD(1) = PEMAG
      STATEV(1) = FIELD(1)
      RETURN
      END
```

Figure 9-2 Subroutine USDFLD used for hardening/softening

9.2 Elastic Stiffness

The implementation procedure of hardening law in ABAQU/STANDARD used section 4.5 in this study is shown in Figure 9-3 and Figure 9-4. Two field variables are considered in this study: FIELD (1) = equivalent plastic strain magnitude (to update shear strength and dilation parameters as discussed in section 4.5), and FIELD (2) = $(p/p_o)^n$ to update the elastic stiffness, *E* as shown in subroutine USDFLD, Figure 9-3. Figure 9-4 shows the implementation procedure in an ABAQUS/STANDARD data file. At any time step, if the value of a state variable (obtained from subroutine USDFLD) is within the given ranges for the corresponding field variable (e.g. shown in Figure 9-4), the desired material property is estimated based on interpolation. Further details and necessary explanations are available in ABAQUS documentation.

```
      SUBROUTINE USDFLD(FIELD,STATEV,PNEWDT,DIRECT,T,CELENT,
     1 TIME,DTIME,CMNAME,ORNAME,NFIELD,NSTATV,NOEL,NPT,LAYER,
     2 KSPT,KSTEP,KINC,NDI,NSHR,COORD,JMAC,JMATYP,MATLAYO,
     3 LACCFLA)
C
      INCLUDE 'ABA_PARAM.INC'
C
      CHARACTER*80 CMNAME,ORNAME
      CHARACTER*3  FLGRAY(15)
      DIMENSION FIELD(NFIELD),STATEV(NSTATV),DIRECT(3,3),
     1 T(3,3),TIME(2)
      DIMENSION ARRAY(15),JARRAY(15),JMAC(*),JMATYP(*),
     1 COORD(*)
C
      SAVE KINCOLD
      DATA KINCOLD /0/
C                ATMOSPHERIC PRESSURE
      PATM = 100.
C                GET CONFINING STRESS VALUE
      CALL GETVRM('SINV',ARRAY,JARRAY,FLGRAY,JRCD,JMAC,JMATYP,MATLAYO,
     2 LACCFLA)
      PRESS = ARRAY(3)
C               PRINT NEGATIVE STRESS, ONCE PER INCREMENT
      IF (PRESS.LE.0.0) THEN
        IF (KINC.GT.KINCOLD) THEN
              WRITE (6,1000) KSTEP, KINC, NOEL, NPT ,PRESS
1000          FORMAT(2I4,I7,I4,E12.5)
         KINCOLD = KINC
        END IF
      END IF
C               UPDATE MODULUS DURING THE GEOSTATIC STEP
      IF (KSTEP.EQ.1) THEN
       IF (PRESS.LT.10.0) PRESS = 10.0
       PE = 0.5
       PRESS = (PRESS/PATM)**PE
C
       FIELD(2) = PRESS
       STATEV(2) = FIELD(2)
      END IF
C
C               GET EQUIVALENT PLASTIC STRAIN
      CALL GETVRM('PE',ARRAY,JARRAY,FLGRAY,JRCD,JMAC,JMATYP,MATLAYO,
     2 LACCFLA)
      PEMAG = ARRAY(8)
      FIELD(1) = PEMAG
      STATEV(1) = FIELD(1)
      RETURN
      END
```

Figure 9-3 Subroutine USDFLD for elastic stiffness variation

```
** MATERIALS
**
*Material, name=PIPE
*Elastic
 2e+08, 0.3
*Material, name=SOIL
****Dependence of elastic modulus on confinig pressure
*ELASTIC, DEPENDENCIES = 2
**** E = Eo * (p/p0)^n
7.6E+3, 0.3, 0, 0, 0.31
7.6E+3, 0.3, 0, 10.0, 0.31
24.5E+3, 0.3, 0, 0.0, 1.0
24.5E+3, 0.3, 0, 10.0,1.0
49E+3, 0.3, 0, 0.0, 2.0
49E+3, 0.3, 0, 10.0,2.0
98E+3, 0.3, 0, 0.0, 4.0
98E+3, 0.3, 0, 10.0,4.0
147E+3, 0.3, 0, 0.0, 6.0
147E+3, 0.3, 0, 10.0,6.0
*USER DEFINED FIELD
*DEPVAR
2
****Dependence of friction and dilation angles on the plastic strain level
*MOHR COULOMB, DEPENDENCIES = 1
37.5,2.4,0,0.0000
39.0,4.3,0,0.0014
41.2,7.2,0,0.0050
42.3,8.6,0,0.0088
43.5,10.3,0,0.0162
43.7,10.6,0,0.0245
42.3,8.7,0,0.0338
39.3,4.7,0,0.0527
37.2,2.1,0,0.0707
36.1,0.7,0,0.0969
35.6,0.0,0,0.1434
35.3,0.0,1,0.3877
35.3,0.0,2,1.1125
35.3,0.0,3,1.4164
35.3,0.0,0,10.0
****Dependence of cohesion on the plastic strain level
*MOHR COULOMB HARDENING, DEPENDENCIES = 1
17.0,0,0,0.0000
19.0,0,0,0.0014
20.8,0,0,0.0050
21.0,0,0,0.0088
20.6,0,0,0.0162
18.8,0,0,0.0245
16.1,0,0,0.0338
11.2,0,0,0.0527
8.5,0,0,0.0707
8.0,0,0,0.0969
8.0,0,0,0.1434
8.0,0,0,0.3877
8.0,0,0,1.1125
8.0,0,0,1.4164
8.0,0,0,10.0
```

Figure 9-4 Implementation of state-dependent material properties

10 APPENDIX B : ASSESSMENT OF INSAR CURRENT PRACTICE FOR REMOTE SENSING APPLICATIONS

10.1 Synthetic Aperture Radar (SAR) Interferometry

Synthetic aperture radar (SAR) technology, in combination with interferometry, has the ability to measure topography or ground movement. The technique is called Interferometric Synthetic Aperture Radar (InSAR), and in the context of its use in measuring relative ground movement, it is often referred to as Differential InSAR, or DInSAR. When SAR is mounted on a satellite, InSAR provides a convenient means of measuring ground movement, often without the deployment of field personnel or the expense of aircraft. Wherever vertical differential movement occurs due to subsidence, slides, settling, or creep, InSAR can often estimate the differential movement to sub-centimeter accuracy. Several radar satellites are commercially available to collect InSAR data on corridors of interest. For some locations, historical data dating back to 1992 is also available which provides a unique ability to perform historical reviews of ground movement when other data sources do not exist.

10.2 Principles of Interferometry from Space

In recent years, spaceborne repeat-pass InSAR has received much attention for its ability to generate deformation maps with unprecedented accuracy (centimeter or millimeter level). SAR is an active sensor that was developed as a means of overcoming the limitations of real aperture radars. (Curlander and McDonough, 1991) SAR achieves relatively good resolution using a small radar antenna, which is an important consideration when dealing with satellites that are limited in size and are typically launched into orbits that are hundreds of miles above the Earth. To achieve this high resolution, SAR uses the motion of the radar along a flight path (or orbit) to form a ‘synthetic antenna’ that is much larger than its real aperture. This improves the resolution of the radar in the direction parallel to the satellite track, namely, the azimuth direction, as shown in Figure 10-1. To achieve a high resolution in the across track or range direction, the radar uses a frequency modulated waveform and pulse compression to simulate a very short pulse, hence a high-resolution echo. The typical horizontal, spatial resolution obtained via current satellite SAR ranges from 8-150 m, and resolutions typically used for InSAR are 8-30 m.

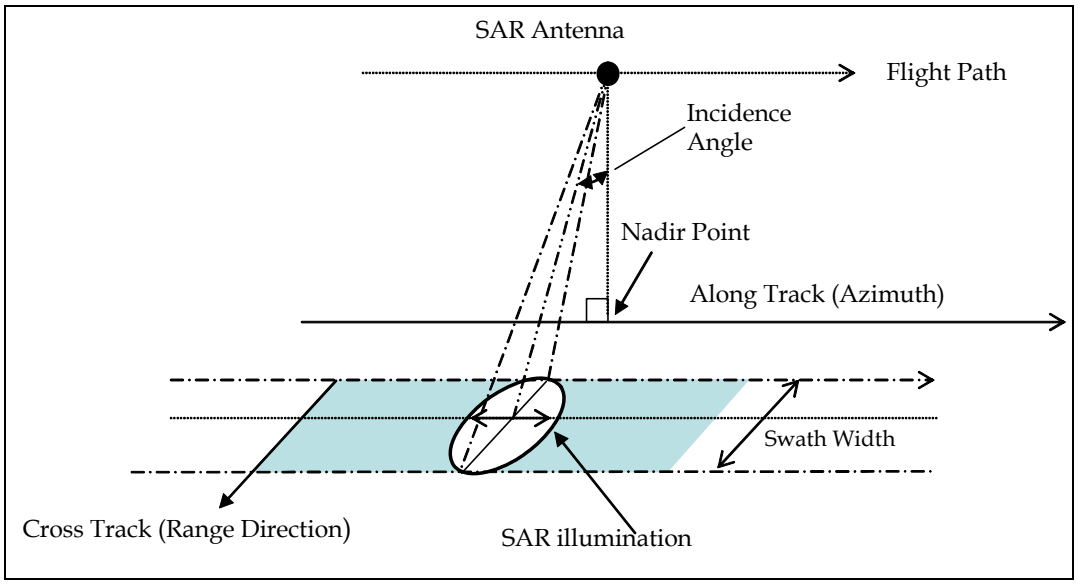

Figure 10-1 Geometry of synthetic aperture radar

Since the radar image contains the phase (ϕ) as well as the magnitude (A) of the backscattered radiation, topographic information can be derived from the difference in the phase, that is, the interferogram, between two images. (Massonnet and Feigl, 1998) In particular, Figure 10-2 is a simplified illustration of the variation in phase due to ground movement. The change in the distance (d) between the satellite and any point on the ground (change along the look direction of the SAR) is simply the fraction, as determined from the interferogram phase ($\phi_2 - \phi_1$) for the two images, of half the radar wavelength (λ). The conversion from measured change along the look direction to the actual ground movement relies on an understanding of the ground dynamics in order to interpret the direction, and hence magnitude, of movement. When possible, measurements from another look direction may also be used to help decipher the actual ground movement.

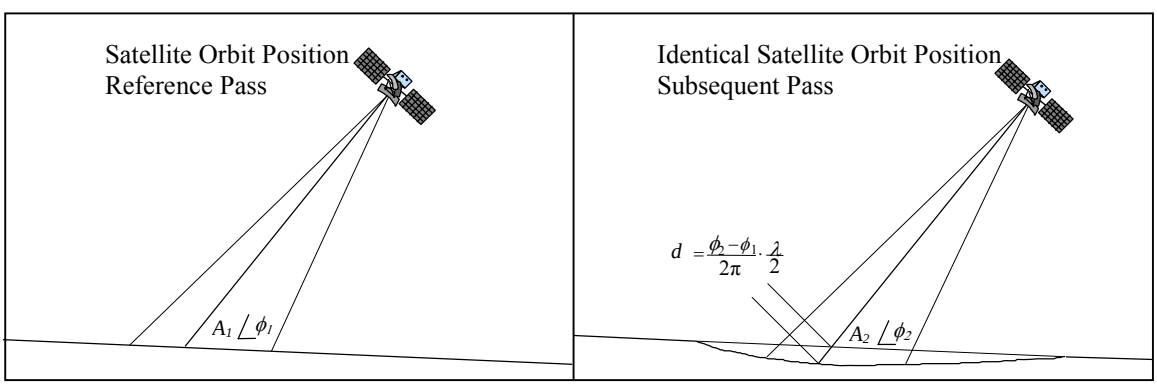

Figure 10-2 InSAR measurement of ground movement

InSAR is thus based on the combination of two complex (magnitude and phase) and co-registered (aligned) radar images of the same area from an almost identical perspective. The phase difference for each pixel in the resulting interferogram is a

measure of the relative change in distance between the scatterer (the ground) and the SAR antenna as shown in Figure 10-3. If the observation points for the two images composing the interferogram are slightly different, a digital elevation model (DEM) can be derived from the interferogram phase, assuming that no large-scale deformation has occurred between the recordings. (Zebker and Goldstein, 1986) On the other hand, deformation information can be derived if the SAR observation points are the same for the two images composing the interferogram, or if a DEM of the area is available. The latter is achieved by modeling the topographic phase contributions based on an input DEM and the geometry of the imaging. The phase contributions arising from the topography are then subtracted from the overall interferogram. This technique allows generation of very high accuracy (centimeter or millimeter level) deformation maps.

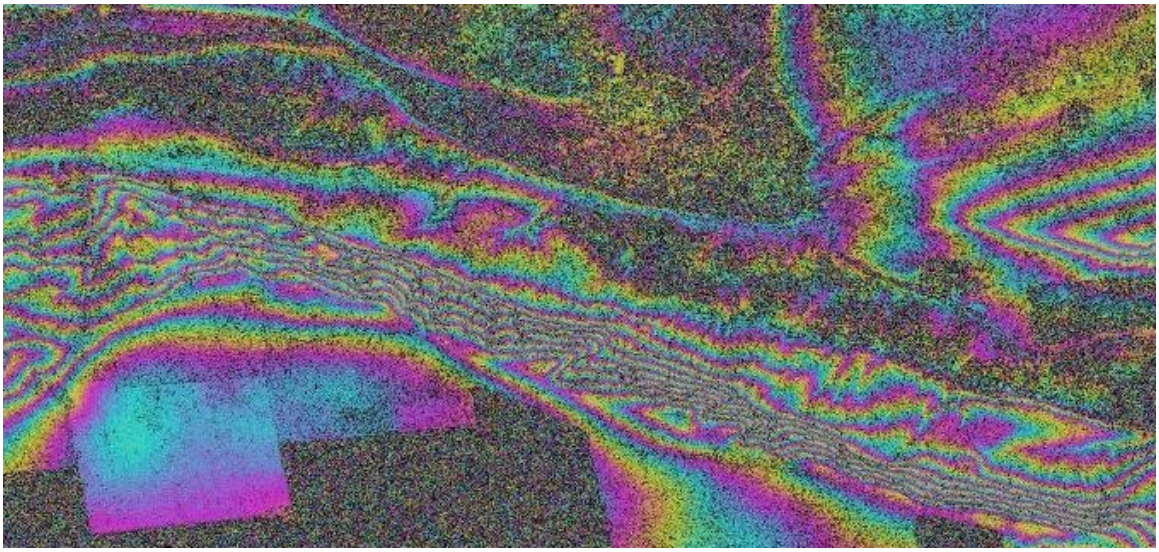

Figure 10-3 InSAR interferogram

InSAR is unique and hardly comparable to any conventional technique of deformation measurement. Although it is becoming more accepted, the technique has to date been used in a limited number of operational applications, such as volcano and earthquake monitoring as well as subsidence monitoring. Two European satellites (ENVISAT and ERS-2) and one Canadian satellite (RADARSAT-1), as well as data from previous European (ERS-1/2) and Japanese (JERS) satellites exist that are suitable for interferometric work. The spatial resolution for the SAR sensors on these satellites ranges from 30 m to 8 m – RADARSAT Fine Mode, and the orbit repeat cycles are 24 days (RADARSAT), 35 days (ENVISAT and ERS-1/2 for the majority of the mission time), and 44 days (JERS). The ERS-1/2 satellites were also operated in a tandem mode, with a 24-hour difference between the orbits of ERS-1 and ERS-2. Since there is only 24 hours between these tandem mode image acquisitions, there is generally good coherence, and hence the tandem mode is an excellent source of data for creating DEMs. The Shuttle Radar Topography Mission (SRTM) has generated DEMs at 30 m spatial resolution for areas of the Earth below 60° latitude (only 90 m resolution data have been released for areas outside the U.S.). The RADARSAT, ENVISAT, and ERS-1/2 SAR

systems all use a radar wavelength of 56 mm corresponding to a frequency of 5.3 GHz, which is within the C-band radio spectrum. The JERS SAR used a wavelength of 235 mm corresponding to a frequency of 1.3 GHz, which lies within the L-band radio spectrum.

The use of satellite imagery for InSAR is convenient in that one can monitor almost any region, or as many regions, in the world as desired with equal ease. InSAR has also been successfully demonstrated from SAR equipped aircraft. This is usually more expensive but it offers the advantages of providing higher spatial resolution and the ability to control the time of data acquisitions.

The following list outlines the general methodology of InSAR analysis;

- Select & procure SAR data on basis of meteorological data & satellite baseline.
- Extract/acquire digital elevation model (DEM) for use with the analysis.
- Perform InSAR analysis, which includes:
    - SAR image processing;
    - Image geo-referencing (to DEM and other site data);
    - Image pair registration;
    - Coherence measurement;
    - Interferogram production;
    - Phase unwrapping;
    - Phase conversion to deformation; and
    - Map product generation.
- Perform deformation analysis.
- Perform geotechnical analysis and correlation of InSAR deformation movement to in-situ data collections.

10.3 Factors Affecting InSAR Results

Because InSAR measures relative changes in phase, accuracy is on the order of fractions of a wavelength. For RADARSAT, ENVISAT and ERS satellites, one wavelength is 56 mm and measurements of ground subsidence on the millimeter scale have been demonstrated. However, the use of InSAR in the measurement of ground movement relies on accounting for any changes in the radar phase over the monitoring interval due to factors other than the change in the slant range distance. In particular, the radar phase will be affected by changes in the reflectivity (and the relative location) of the ground (temporal decorrelation), by changes in the viewing perspective (baseline decorrelation), and by changes in the atmosphere. In the worst cases, these factors will prevent the determination of ground movement from the interferogram phase. However, there are many cases where sub-centimeter and, indeed, millimeter accuracy can be achieved.

10.3.1 Temporal Decorrelation

Probably the most important limiting factor in the application of InSAR is temporal decorrelation of the ground between the interferometric acquisitions, and hence a loss of meaningful phase relation between corresponding pixels in an image pair. Temporal decorrelation usually results from changes in the complex reflection coefficient of the imaged surface. (Zebker and Villasenor, 1992) Changes in the reflection coefficient are generally due to variation in the moisture content or the vegetation. Thus, decorrelation times can be as long as months to years for arid terrain and as short as several hours to several days for rainy and / or forested areas. Sparsely vegetated terrain can have decorrelation times between several days to several months. Snow-covered and frozen terrains are generally coherent over short-terms, but are sensitive to melting and snowfall. Since each pixel in a SAR image is formed by the coherent sum of the backscatter from thousands of cells on the scale of the radar wavelength, temporal decorrelation can also result from the relative movement of the scattering cells within the SAR resolution. This is particularly relevant to slope movement, since in some instances relative motion of the ground on a scale smaller than the SAR resolution may occur.

Since C-band radar has a wavelength similar to the size of small-scale vegetation characteristics — such as crop structure, foliage, and tree canopy structure — SAR images at C-band are dependent on the variations of these features, which often occur on a daily or weekly timeframe. In contrast, longer wavelength L-band radar has a wavelength on the scale of tree trunk and branch structures, which generally change over a much longer timeframe. Thus, in vegetated areas, the longer wavelength SAR provides the possibility of obtaining useable interferometric pairs over longer timeframes than provided by C-band SAR.

The problem of temporal decorrelation due to changes in the complex reflectivity of the ground or the vegetation can be mitigated through the use of phase-stable targets, such as buildings, other anthropogenic infrastructure, rock or gravel outcroppings, or radar reflectors — as shown in Figure 10-4— that are installed specifically for this purpose. In these cases, however, the ground movement is measured at isolated points, and only if the spatial density of such points is high, can a continuous spatial estimate be made of the ground movement.

Figure 10-4 Reflectors can be used to mitigate the problem of temporal decorrelation

Radar reflectors may be either passive or active — the former most often being constructed from metal panels as shown in Figure 10-4, and the latter being constructed with receive and transmit antennas linked through an amplifier. Active reflectors are smaller but they require a power source and are generally more expensive. Passive reflectors come in several variations, including dielectric lens, flat panels (mirror-type), dihedrals (two perpendicular panels), and trihedrals (three-panel corner, as in Figure 10-4).

In recent years, interest has been increasing in the use of permanent scatterers for SAR interferometry. (Ferretti, et al., 2000, 2001, Werner, et. Al., 2003) It is based on identifying point targets that are coherent over an extended timeframe. By measuring the interferometric phase at such points over multiple timeframes, the topographic, atmospheric, and decorrelation noise contributions can be isolated, thereby permitting an accurate assessment of the differential phase due to ground movement. Specifically, the technique relies on using the characteristic temporal and spatial scales of these contributions to aid in their identification. Accuracies approaching a millimeter have been obtained based on interferogram stacks of 40 to 60 ERS-1/2 scenes.

10.3.2 Baseline Decorrelation

Variation in the phase occurs with different viewing geometries, since the relative locations of the scattering cells depend on the viewing position. (Zebker and Goldstein, 1986) The different viewing geometries are denoted by the satellite baseline, or the difference in orbit position from one satellite pass to the next. Satellite baseline position (both parallel and perpendicular) is illustrated in Figure 10-5. The variation in phase due to baseline is beyond the simple distance and phase relationship that is the basis of DEM and deformation measurements. The variation of phase with viewing geometry leads to a maximum separation between two observation locations that can be used for InSAR analysis. This maximum separation is called the critical baseline, and is dependent on the

radar wavelength, the sensor-target distance, the range resolution and the incidence angle (the angle of the satellite look direction from nadir, i.e., perpendicular to the ground). Further, the coherence of an interferometric pair depends on the spectral correlation between the two observations at different viewing geometries. (Gatelli, et al., 1994)

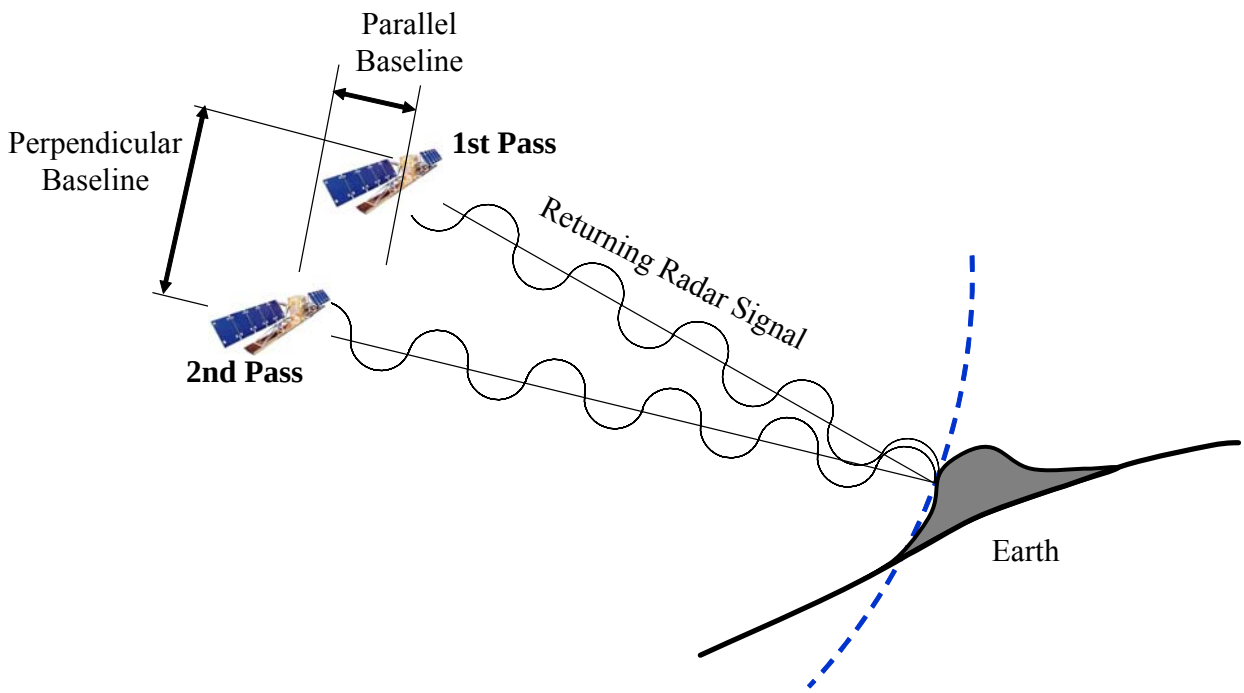

Figure 10-5 Orbit baseline changes can produce varying phase shifts

One should note that when a point target dominates the radar return within a SAR resolution cell, there is no baseline decorrelation. This, of course, assumes that the radar response from the point target is isotropic, at least within the variation of the SAR viewing geometries. The use of point targets, therefore, has the advantage that it is not sensitive to orbit baseline separation, so that it permits the use of available SAR images with larger baselines, often enabling more frequent monitoring.

10.3.3 Atmospheric Effects

There are numerous studies of the influence on InSAR of atmospheric effects, ranging from homogeneous effects to heterogeneities in both the troposphere and the ionosphere. (Tarayre and Massonnet, 1996) Phase shifts due to homogeneous atmospheres produce additional interferometric fringes and can be accounted for by adjusting the satellite baseline. Given sufficient coherence, heterogeneities can often be recognized on the interferogram. Alternatively, the variation due to atmospheric effects can be isolated from multiple interferograms. (Fruneau and Sarti, 2000) This is also the approach in using interferometric stacks and in permanent scatterers analysis. In particular, for large numbers of interferograms, the atmospheric effects can be identified as a random process over time and thereby separated from other contributions to the interferometric phase.

10.4 Slope Movement Monitoring

The use of InSAR to measure ground movement along slopes is not as common as other applications, such as measuring crustal deformation due to earthquakes and volcanoes, and measuring subsidence, especially in urban areas. There are issues associated with using InSAR that are accentuated when it is applied to measuring slope movement. This includes the sensitivity of the SAR system to the actual slope movement, based on its look-direction and spatial and temporal resolutions.

10.4.1 SAR Look Direction

For the current polar-orbiting SAR satellites, the look direction (except at high latitudes) is generally either east or west, for either ascending or descending orbits respectively, as shown in Figure 10-6. These SAR systems are, therefore, sensitive to movement along slopes facing either east or west, and insensitive to movements in either a north or south direction. Furthermore, if the SAR look direction faces the slope, then once again the SAR is not very sensitive to movement along the slope, and, in addition, the slope face may be imaged at close to the same SAR slant range, as seen in Figure 10-7. This effect is worst when the slope inclination is equal to the SAR incidence angle. For steeper slopes, the SAR image suffers from layover, since the upper section of the slope is closer to the sensor and therefore it appears to be laid over the lower section.

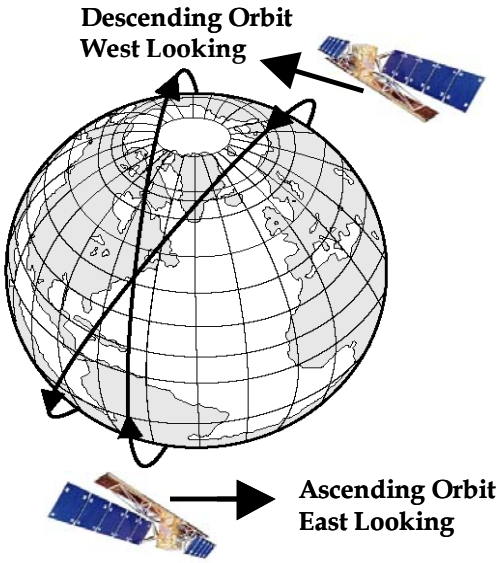

Figure 10-6 Polar orbiting satellites perspective (RADARSAT International, 1995)

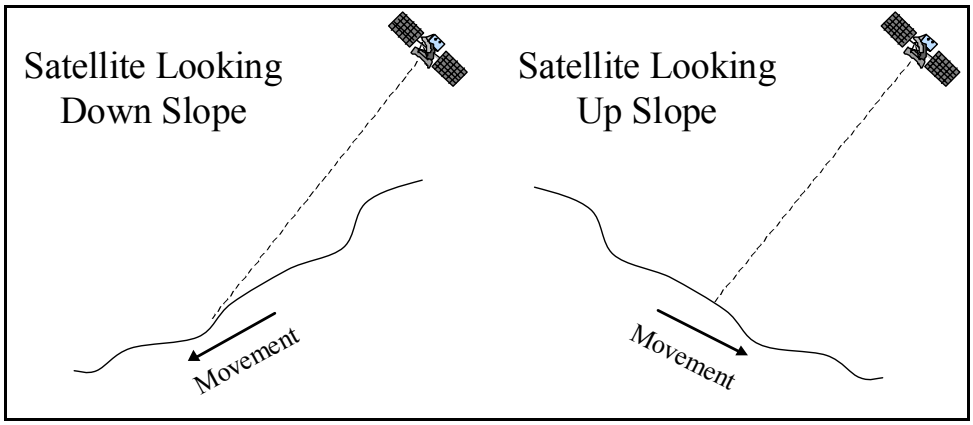

Figure 10-7 Example of satellite looking up-slope and down-slope

Movement along specific slopes is usually defined by characteristic spatial and temporal scales. These may or may not be congruous with the SAR spatial and temporal scales. In particular, small and / or fast moving slopes are difficult to measure using spaceborne InSAR, since the spatial resolutions of the available sensors at present are 8 m to 30 m, while the orbit repeat cycles are 24 days for RADARSAT and 35 days for ENVISAT and ERS-2. If movement along larger slopes is composed of different mechanisms acting on smaller blocks, then once again the spatial resolution of the SAR may be a limiting factor in identifying these mechanisms.

In instances where a slope has to be monitored at high spatial and temporal scales, ground-based SAR systems have been used. Such systems have been used, for example, to monitor landslides in Valdarno, Italy (Pieraccini, et al., 2003) and in Schwaz, Austria (Leva, et al., 2003). An additional advantage of employing this system for high frequency monitoring is that the temporal decorrelation is minimal over the short timeframe between acquisitions.

10.4.2 SAR Layover and Shadow

In addition to considering issues of coherence, baseline and atmosphere, slope monitoring with SAR must also consider the slope direction and steepness along with the SAR incident angle and look direction. During the SAR acquisition, radar shadow will occur whenever the radar is looking downslope and the radar incidence angle is greater than the slope angle. In this case, the area obscured by the top of the slope will obviously not be imaged. Conversely, if the radar is looking at the slope and the radar incidence angle is less than the slope angle, then the top of the slope will be imaged before, or laid over, the lower part. In areas of either layover or shadow, the particular SAR acquisition geometry cannot provide information on slope movement. ERS-1/2 has a fixed incidence angle of approximately 23°, which is considered to be steep. RADARSAT on the other hand has variable incidence angles. For the highest resolution imagery from RADARSAT (i.e. Fine Mode), the incidence angles vary from 36° - 48°. Further explanation of this effect is provided below.

When a spaceborne SAR looks down and to the side toward a steep mountain, many objects on the mountain's facing slope may appear to be located at the same distance from the satellite. Since those many objects are located at nearly the same distance from the SAR, their backscattered signals will return to the spacecraft at about the same time. The SAR sensor will interpret this as a single object located at that distance; consequently the SAR image will be very bright at that location, in which all those responses from the separate objects are mapped into one location. This is called foreshortening in the case with the objects' distances are closely spaced, or layover in the extreme case where responses from, say, a mountain's peak are positioned before surrounding locations. Figure 10-8 below shows an illustrative example of this for one particular incidence angle. In this case, the entire left side of the mountain cannot be imaged properly by the SAR.

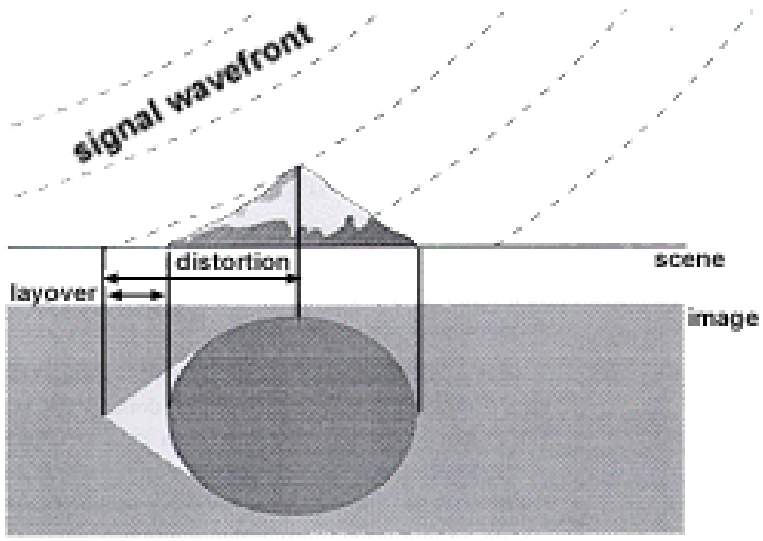

Figure 10-8 The concept of layover in SAR image acquisition

SAR illumination is much like solar illumination, and thus shadowing will also occur in cases where the front side of a slope or mountain creates a shade effect on the back side of the slope or mountain. An example of this is shown in Figure 10-9, except in this case, a much shallower incidence angle is used. After obtaining the very response from the front side of the slope, the SAR will suddenly sense very little or no response from the mountain's opposing face. Note that the mountain's back facing slope may be nearly parallel to the incoming radar, making it seem to the SAR that there are few responses for a significant distance.

Shadow is much worse for shallow incidence angles than for steep ones, Figure 10-9. In Figure 10-8, there was almost no shadow on the right side of the slope, but in Figure 10-9, the entire left side of the slope is shadowed. So, for example, ERS will have less shadow problems than RADARSAT-1. However, as Figure 10-9 shows, the satellite

does not have a problem imaging the left side of the slope, as did the satellite in Figure 10-8. This implies that there is a trade off; satellites with shallow incidence angles will have a more difficult time imaging all slopes of an area of high relief if there are regions of shadow. However, shallow incidence angles may be more suitable for imaging certain portions of some steep slopes, depending on the geometry of the slope.

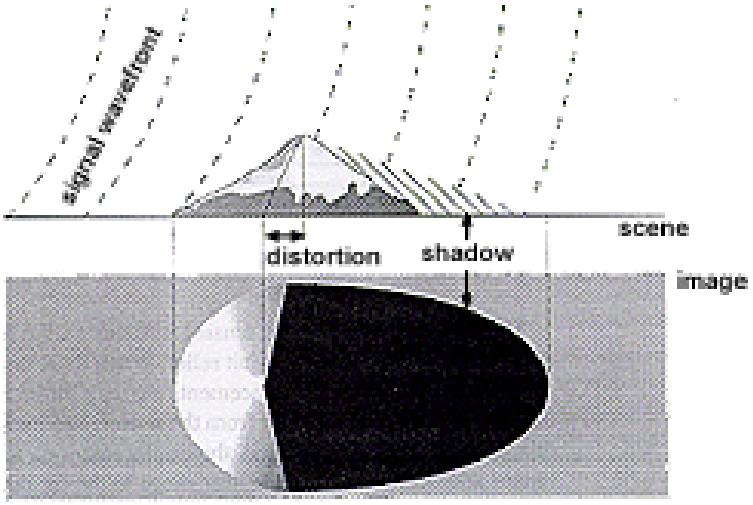

Figure 10-9 The concept of shadow in SAR image acquisition

10.5 Geo-referencing and Control of SAR Images

The native format of a SAR image and the resulting movement data derived by InSAR is a raster image of data points on a uniform grid pattern. These data are not unlike that of aerial photographs, however, points on the ground are representative of microwave radiation echoes (or interpreted ground movement) rather than solar illumination. As a consequence, SAR data can be placed on a ground coordinate system (i.e., geo-referenced) using methodologies already established for use in aerial or satellite photogrammetry. These methodologies usually involve the use of surveyed ground control points (GCPs) located in the region of interest that can fix a point in the image to a location on the ground.

10.5.1 Collection of GCPs for Geo-referencing of SAR Images

For aerial photography, usable GCPs are objects or monuments that can be easily identified and surveyed in the air photo such as the corners of buildings or road intersections. In the absence of easily identifiable GCPs (e.g., in a rural area), control points can be placed throughout a region of interest prior to image acquisition. For example, a large white cross or square placed on bare ground can serve as a convenient and inexpensive benchmark; this artificial monument can be surveyed and subsequently removed after the air photo is captured. A suitable number of these GCPs located (or

placed) throughout the air photo will allow the image to be tied to ground coordinates (e.g., state plane) and subsequently projected to a particular map projection (e.g., Universal Transverse Mercator, (UTM)).

Since SAR images are comprised of microwave echoes, the method of collecting GCPs is slightly different than that performed for air photos. Many objects that are highly visible in air photos are not visible to the SAR instrument. For example, painted white lines on a road are highly visible in an air photo but are invisible to the SAR. Therefore, GCPs must be selected that are highly visible to the radar and are easily geo-located or surveyed. For example, roadways are generally visible in SAR images and road intersections can be used as GCPs. Suitable natural GCPs include lakes and river edges (that generally are dark in SAR images) and ridgelines (that generally are bright in SAR images). Corner reflectors as shown previously in Figure 10-4 are most commonly used as artificial GCPs in SAR because they show up very brightly as point targets in the SAR image. They can also be pegged in place permanently if necessary and are easily surveyed with traditional equipment.

Rigorous geo-referencing of SAR images is particularly important for the application of InSAR. Raw SAR data received from image vendors is typically poorly geo-referenced with geo-referencing errors on the order of hundreds or thousands of metres. New generation satellites such as ENVISAT and RADARSAT-2 have much better base geo-referencing due to the availability of onboard Global Positioning System (GPS) for precision orbit estimation. This does not eliminate the importance of a rigorous manual geo-referencing procedure using GCPs from the most accurate source available. Manual geo-referencing allows a more accurate placement of the SAR image (and the interpreted InSAR derived movement data) in a coordinate system that is common with other forms of data, such as GIS layers (road networks, infrastructure, etc.), elevation models and topographic maps. This will facilitate a more accurate assessment of the implications of movement measurements with InSAR. In addition, InSAR requires the alignment of the SAR images with a digital elevation model to remove topographic phase; thus the precise alignment of SAR images to a reference coordinate system common with the elevation model is important. Otherwise, residual topographic phase might remain in the InSAR derived movement image, and in the extreme case, might mask actual movement data which would lead to incorrect movement interpretations.

10.5.2 Sources of SAR GCPs

As mentioned above, surveyed corner reflectors are one of the best sources of GCPs for SAR data. While this is the case, it is not always possible or even necessary to place corner reflectors in the region of interest. Cost of procurement and placement of reflectors may preclude their use in a project and a new SAR image must be acquired after reflector placement to reference previously acquired SAR images in data archives. Often, there are other equally suitable data available for geo-referencing purposes, which involve other raster or vector data that have been previously referenced using survey and

control methods. These data include topographic maps, orthophotography, and photogrammetry, and are described in the following subsections.

10.5.3 Topographic Maps

Topographic maps provide the most comprehensive coverage as a control source. Thus, this is the most readily available source of SAR GCPs. In general these are available for all areas at a scale of 1:50,000. These can be used to geo-reference SAR data to within 20 metres horizontal accuracy. Features such as road intersections, water body edges and ridgelines are easily identified on these maps and their corresponding geo-locations can be used as GCPs for the SAR image. For many InSAR projects, the geo-spatial accuracy obtainable using topographic maps is often more than suitable.

While these topographical maps are readily available, they are limited by the geo-spatial accuracy of the base map and the limited quantity of natural or manmade GCPs that may be available throughout the image. In the case of flat rural terrain with few roads or other infrastructure, it can sometimes be challenging to find more than a couple of suitable GCPs. The use of topographic maps might also result in inaccurate geo-referencing of the SAR images if the information on the topographic map is not up-to-date. For instance, recent road re-alignments may not be reflected in the topographic map, and this could lead to incorrect placement of the SAR image if the new road alignment was used as a source of GCPs. This is particularly relevant in this project; two of the three sites used in this project have had extensive road work performed within the last eight years.

Another convenient source of SAR GCPs is aerial photography that has been properly geo-referenced to a standard datum and orthorectified to a suitable map projection. These include orthophotography and site specific photogrammetry.

10.5.4 High Resolution Orthophotography

Existing digital orthophotography can provide highly accurate horizontal control, assuming availability in the study areas. Many counties or local consortiums maintain high resolution orthophotography as part of their electronic Geographic Information System (GIS). Pixel resolutions typically range from 15 – 60 cm. Since this is a 2-dimensional product, only horizontal control can be obtained. Vertical control could conceivably be obtained (interpolated) from the underlying Digital Elevation Model (DEM). Although these are not as accurate as a contour DTM, elevations obtained are certainly suitable for the desired application. Elevation inaccuracies could range up to 3 m.

10.5.5 Photogrammetry

Existing photogrammetry projects are another source of controlled SAR GCPs. The accuracy of photo identifiable control is relative to the flying height of the photography, which can vary widely depending on the mapping requirements (i.e. map scale and

contour interval). Typical photogrammetry mapping projects will range from 1:600 to 1:2400 in map scale and will yield horizontal accuracies ranging from 30 – 150 cm. Vertical accuracies of the underlying elevation model, assuming contour intervals from 30 – 150 cm, will range from ± 15 – 75 cm.

10.5.6 Summary of GCP Collection

In the case of the examples provided above, GCPs are only available within the extent of the established air-photo and associated control. In cases where the high-resolution air photo coverage is much smaller than that of the SAR image, additional GCPs must be collected from other sources.

It is important to note that the presence of comprehensive site survey and control data will not alone facilitate the geo-referencing of SAR images unless the benchmarks used in the survey can be visualized in the SAR image. This is most often not the case, since the monuments used for surveying (i.e., pegs or rebar rods) are not visible in a SAR image. The site survey and control information is only useful if it is tied in with a source of usable GCPs, which is most often an orthorectified air photo.

10.6 Site & InSAR Suitability

There are several factors to be considered when determining a site's suitability for InSAR monitoring. These include;

- Slope Alignment:
  Slopes that are ideal for InSAR monitoring are those facing in a general East or West direction. This maximizes sensitivity of the SAR instrument, because it is pointed in the direction of the assumed slope movement. Slopes that are facing in a North or South direction may be effectively monitored with InSAR; however, the minimum detectable movement is higher for these slopes. This minimum detectable movement is determined by the slope geometry.

- Slope Grade:
  Steep slopes are often difficult to monitor with InSAR due to layover, foreshortening and shadow effects. In addition, complicated topography creates a challenge in eliminating residual topographic phase, especially when an accurate DEM is not available. Slope grades that are much less than the SAR incidence angle are preferable.

- Image Coherence:
  The InSAR coherence is one of the main factors in determining suitability. Slopes with heavy brush, fast growing vegetation and deciduous forests are generally not suitable for InSAR monitoring unless natural or artificial (e.g., structures, corner reflectors) point targets are present.

- Existing Site Data:
  The availability of site survey and control data, coupled with orthophotography, is very useful for maximizing the accuracy of the horizontal positioning of the InSAR data. In addition, these data help to provide a means to interpret the InSAR-derived movement information to determine the overall impact of any significant movement. The availability of a recent DEM is also important to the application of InSAR. Usable DEMs have the following specifications: 25 – 30 m spacing with vertical accuracies of 5 – 20 m. Ideally, the DEM should cover the entire region SAR image (50 × 50 km or 100 × 100 km), and minimally should cover about 5% (~125 km^2) of the SAR image.

- Data availability:
  New data can always be captured on sites of interest; however, the availability of a large quantity of SAR data in the historical archive will also facilitate a review of the movement history if the data are closely spaced in time and have reasonable coherence. This is particularly relevant in a project where it is required to perform an historical analysis of the movement using data available in the SAR archive.

10.7 Variations To Application Of InSAR Monitoring

There are several variations that can be made to the application of InSAR. In addition, there are several new satellites that have recently been launched which will provide enhancements over current capabilities. These are listed below.

- Corner reflectors: Phase stable reflectors can serve the dual purpose of facilitating geo-referencing to site control and improving coherence in regions that are not suitable for traditional InSAR. Reflectors made from sheet and angle aluminum are robust and not generally susceptible to wind, rain or snow damage. Tests conducted in Alberta and Newfoundland, Canada, have demonstrated their ability to weather harsh environments over many years. As shown in Figure 11 10, several designs are available, including those mounted with steel pegs and on concrete base foundations. The steel peg design can be field assembled and installed in about 90 minutes. There are issues specific to those techniques that include, for example, the proper sizing, placement and positioning of reflectors, the resolution of phase ambiguities in the interferograms with spatially discontinuous phase information, and the removal of artifacts such as atmospheric effects. (Ferretti, et al., 2000, 2001, Werner, et al., 2003).

there are several new satellites that have recently been launched which will provide enhancements over current capabilities. These are listed below.

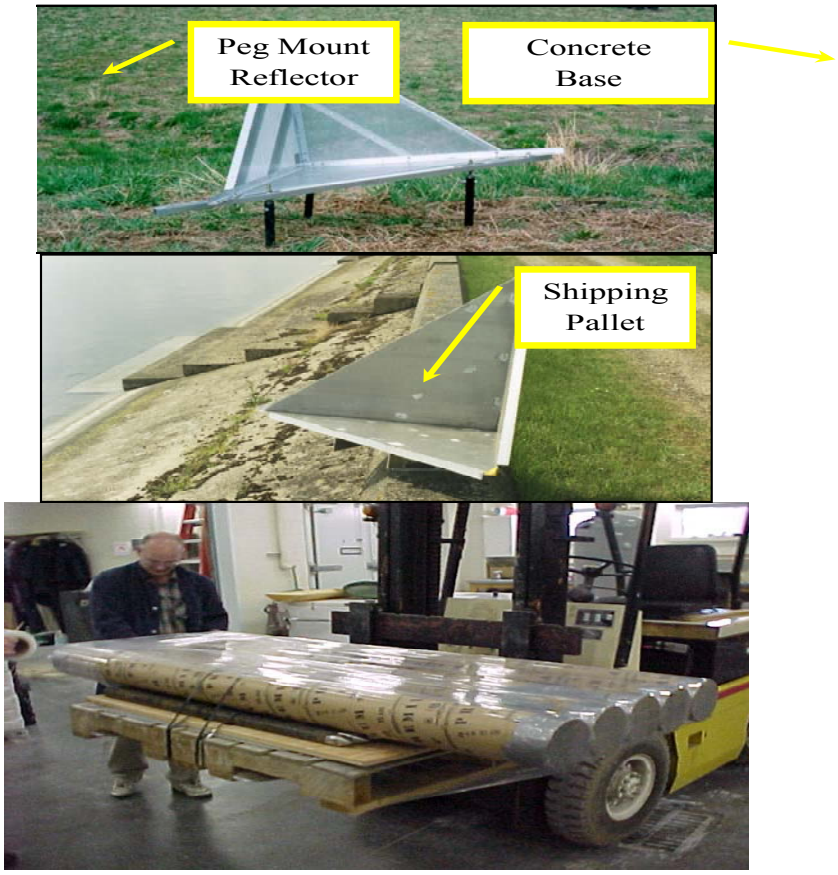

Figure 10-10 Radar reflectors using two different mounts (upper left and right), and packaged for shipping (lower centre)

- Interferometric Point Target Analysis (IPTA): IPTA and PS InSAR is finding greater use due to lower costs of European ERS and ENVISAT data and the relative success that monitoring programs have seen in producing high accuracy results (on the order of millimeters). They are typically used with historically archived data and require stacks of images of minimum 15 scenes and more typically between 25 – 35 images covering 3 – 5 year timeframes. When used in conjunction with corner reflectors, success in the application of InSAR is virtually guaranteed regardless of the site. If the ground movement behavior can be described by a mathematical model, the technique can also be used to correct for atmospheric effects and topographic errors. Figure 10-11 shows an example of subsidence within an urban area as determined using the IPTA technique. (GAMMA website)

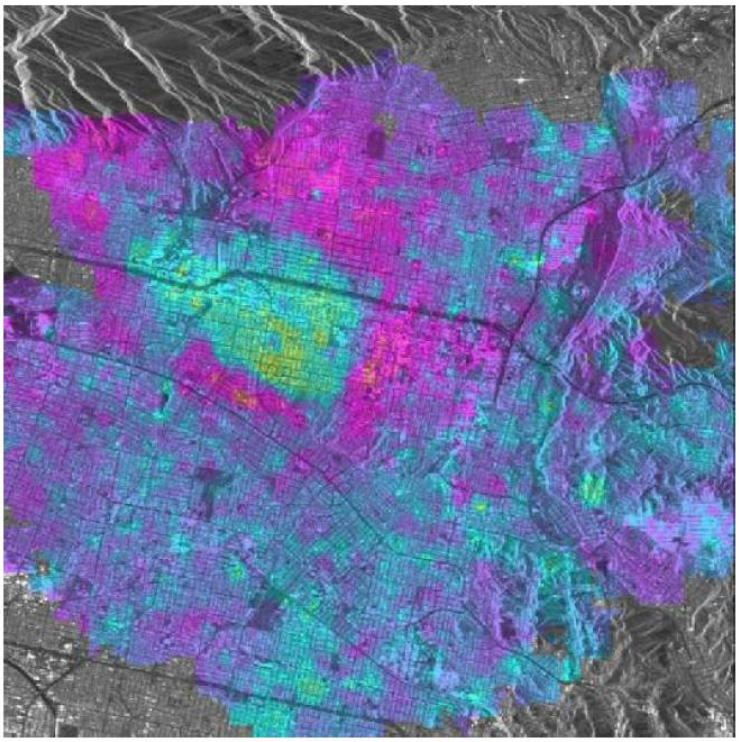

Figure 10-11 IPTA example (Colour Cycle = 4 mm /year) (GAMMA website)

- Higher resolution satellites: Two new high resolution SAR satellites have been launched in 2007, RADARSAT-2 and TerraSAR-X, as shown in the illustrations of Figure 10-12. RADARSAT-2 is a C-band satellite (similar to RADARSAT-1, ERS and ENVISAT) and has a maximum resolution of 3 m, with the possibility of being increased to 1 m after launch. This platform has much better orbit control than its predecessor RADARSAT-1, and consequently more of the scenes acquired for monitoring programs should be suitable for InSAR. The increased C-Band (5.4 GHz) resolution should, in theory, improve coherence due to reduced clutter levels in higher resolution cells and consequently regions that are presently not suitable for InSAR may be suitable with RADARSAT-2. TerraSAR-X has have a maximum resolution of 1 m, although it operates at X-Band (9.65 GHz) and may be less suitable for InSAR in vegetated regions compared with RADARSAT-2. The relatively high resolutions from these two satellites imply that ground motion monitoring will increase significantly due to the ability to image smaller features on the ground and thus measure greater movement details. This will be particularly relavant for monitoring smaller slopes or slopes with smaller or more complex moving features.

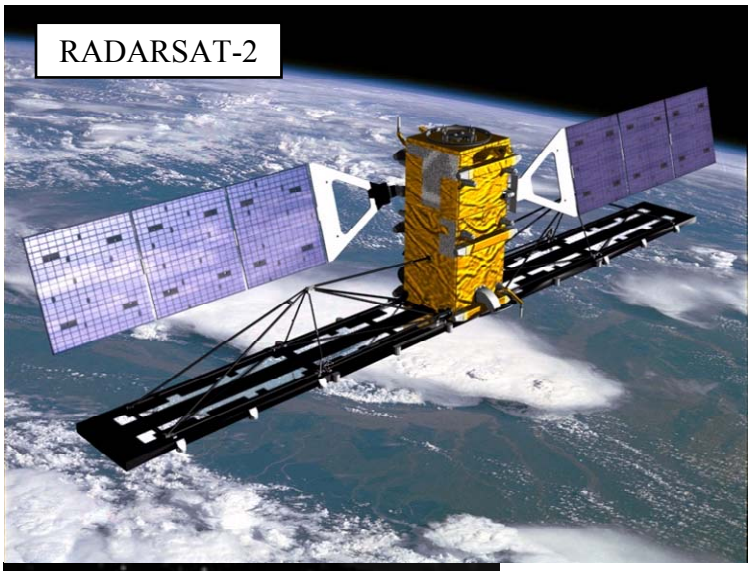

TerraSAR-X

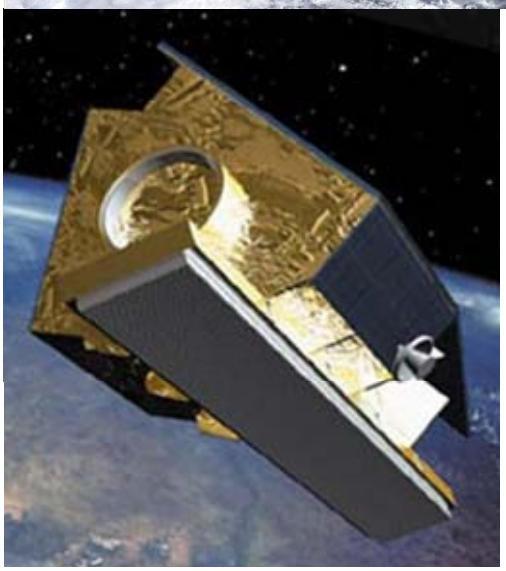

Figure 10-12 The new SAR satellites RADARSAT-2 and TerraSAR-X

L-Band SAR: Advanced Land Observing Satellite (ALOS) carries an L-Band (1.27 GHz) sensor called PALSAR. It is the successor of the Japanese satellite JERS and with imaging resolutions between 7 – 44 m in Fine Mode, it is similar in resolution to RADARSAT-1 and ERS/ENVISAT. L-Band is known to be less susceptible to problems of temporal decorralation due to vegetation. Compared with C-Band (approximately 56 mm), the longer L-Band wavelength (approximately 246 mm) does not interact as much with tree canopies because the wavelength is much larger than a typical tree leaf, needle or branch structure. Consequently, certain vegetation types are transparent to the L-Band

sensor, thus the SAR receives more echoes from the ground compared to the vegetation. Although there is improved overall coherence, L-Band is more susceptible to ionsphere effects than C-Band.

10.8 References

Curlander, J.C., and McDonough, R.N. (1991) *Synthetic Aperture Radar: Systems and Signal Processing*, New York: J. Wiley & Sons.

Ferretti, A., Prati, C. and Rocca, F. (2000) "Nonlinear subsidence rate estimation using permanent scatters in differential SAR interferometry" *IEEE Transactions on Geoscience and Remote Sensing*, vol. 38, no.5, pp. 2202-2212, Sept. 2000.

Ferretti, A., Prati, C. and Rocca, F. (2001) "Permanent scatters in SAR interferometry" *IEEE Transactions on Geoscience and Remote Sensing*, vol. 39, no.1, pp. 8-20, January 2001.

Fruneau, B. and Sarti, F. (2000) "Detection of ground subsidence in the city of Paris using radar interferometry: isolation of deformation from atmospheric artifacts using correlation" *Geophysical Research Letters*, vol. 27, no. 24, pp.3981-3984.

Gamma Remote Sensing, http://www.gamma-rs.ch/

Gatelli, F., Monti Guarnieri, A., Parizzi, F., Pasquali, P., Prati, C. and Rocca, F. (1994) "The wavelength shift in SAR interferometry" *IEEE Transactions on Geoscience and Remote Sensing*, vol. 32, no.4, pp. 855-865, July 1994.

Leva, D., Nico, G., Tarchi, D., Fortuny-Guasch, J. and Sieber, A.J. (2003) "SAR-Temporal analysis of landslide by means of a ground-based SAR interferometer" *IEEE Transactions on Geoscience and Remote Sensing*, vol. 41, no. 1, pt.1, pp.745-752.

Massonnet, D. and Feigl, K.L. (1998) "Radar interferometry and its application to changes in the earth's surface" *Reviews of Geophysics*, vol. 36, no. 4, pp. 441-500, Nov. 1998.

Pieraccini, D., Casagli, N., Luzi, G., Tarchi, D., Mecatti, D., Noferini, L. and Atzeni, C., (2003) "Landslide monitoring by ground-based radar interferometry: a field test in Valdarino (Italy)" *Int. J. Remote Sensing,* vol.24, no,6, 1385-1391.

RADARSAT International (1995) "RADARSAT Illuminated, Your guide to products and Services" RADARSAT International Client Services, Richmond, BC, Canada.

Tarayre, H., and Massonnet, D. (1996) "Atmospheric propagation heterogeneities revealed by ERS-1 interferometry" *Geophysical Research Letters*, vol. 23, no. 9, pp. 989-992, May 1996.

Werner, C., Wegmuller, U., Strozzi, T. and Wiesmann, A. (2003) "Interferometric point target analysis for deformation mapping" *IGARSS,* Toulouse, France 21-25 July 2003.

Zebker, H.A., and Goldstein, R.M. (1986) "Topographic mapping from interferometric synthetic aperture radar observations" *Journal of Geophysical Research*, vol.91, (B5), pp.4993-4999, April 1986.

Zebker, H.A. and Villasenor, J. (1992) "Decorrelation in interferometric radar echoes" *IEEE Transactions on Geoscience and Remote Sensing*, vol. 30, no. 5, pp. 950-959, Sept. 1992.

11 APPENDIX C: LATERAL-AXIAL RESPONSE INTERACTION CONSIDERATION

The interaction between the mobilised lateral and axial soil resistance was considered section 6.1 as a potential improvement to the structural soil pipeline response modelling. The interaction diagram, as developed for example in Figure 5-24, was considered to define the axial and lateral resistance limits for the soil spring response, Figure 11-1. As the soil response is symmetric in this plane, only the magnitude of the lateral and axial resistances are considered in the current formulation.

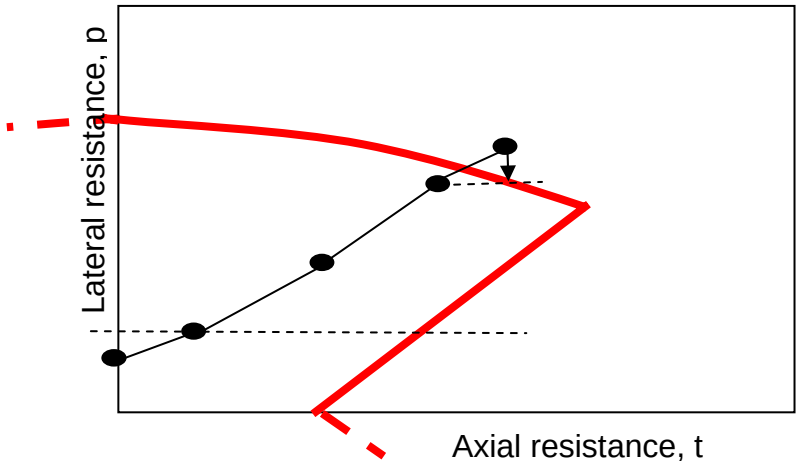

Figure 11-1 Interaction diagram

The interaction limit is defined by the red envelope. As the pipe-soil system is displaced the mobilised resistances in the axial and lateral directions in each soil element are checked. There is a unique value of limit axial resistance on the interaction envelope for any value of lateral resistance, as indicted by the lower dashed line in Figure 11-1. While the 2 mobilised resistances remain inside the interaction envelope during the analysis, as depicted by the first 4 incremental results, the mobilised resistances are not corrected. When the mobilised resistances leaves the envelope, as shown in increment 5, the resistances are corrected back to the envelope. A similar correction strategy is applied in subsequent incrementally, until the mobilised resistance lie inside the envelope, for example after unloading.

This correction strategy was implemented in Abaqus using Fortran subroutines. Other analysis software, such as PIPLIN, do not currently have this implementation option. A manual correction strategy could then be applied, by which the axial and lateral resistance limits are adjusted over a series of analyses until they are lie acceptably close to the required interaction envelope(s).

LAST PAGE OF DOCUMENT